Oxide ceramics under extreme pressure and radiation conditions

Oxidkeramiken unter extremen Druck- und Bestrahlungsbedingungen
Zur Erlangung des Grades eines Doktors der Naturwissenschaften (Dr. rer. nat.)
genehmigte Dissertation von Beatrice Schuster aus Darmstadt
September 2011 — Darmstadt — D 17

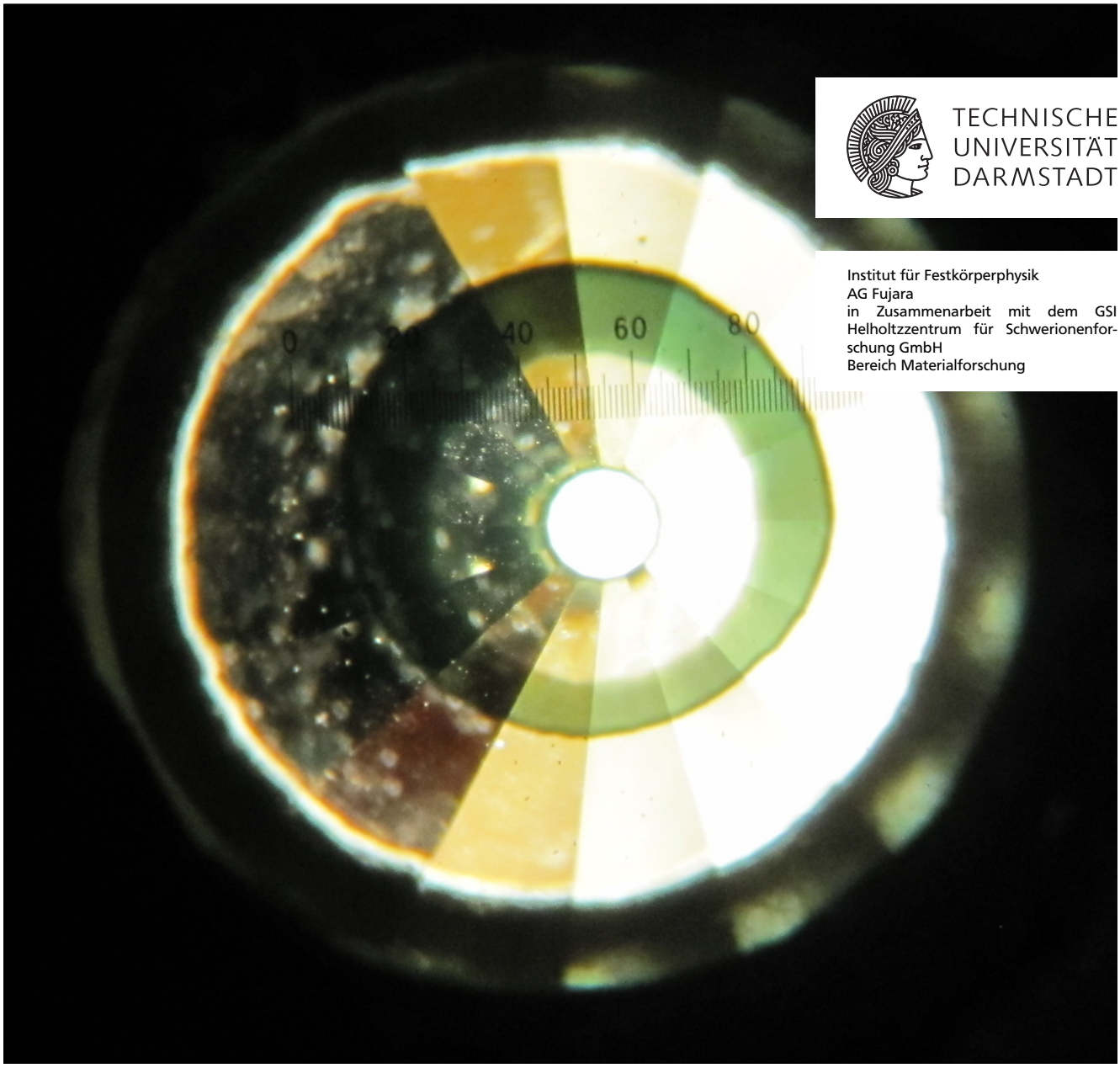

TECHNISCHE UNIVERSITÄT DARMSTADT

Institut für Festkörperphysik
AG Fujara
in Zusammenarbeit mit dem GSI Helholtzzentrum für Schwerionenforschung GmbH
Bereich Materialforschung

Oxide ceramics under extreme pressure and radiation conditions
Oxidkeramiken unter extremen Druck- und Bestrahlungsbedingungen

Genehmigte Dissertation von Beatrice Schuster aus Darmstadt

1. Gutachten: Prof. Dr. Franz Fujara
2. Gutachten: Prof. Dr. Reinhard Neumann

Tag der Einreichung: 14. Juni, 2011
Tag der Prüfung: 13. Juli, 2011

Darmstadt — D 17

Erklärung zur Dissertation

Hiermit versichere ich, die vorliegende Dissertation ohne Hilfe Dritter nur mit den angegebenen Quellen und Hilfsmitteln angefertigt zu haben. Alle Stellen, die aus Quellen entnommen wurden, sind als solche kenntlich gemacht. Diese Arbeit hat in gleicher oder ähnlicher Form noch keiner Prüfungsbehörde vorgelegen.

Darmstadt, den 7. September 2011

(Beatrice Schuster)

Abstract

This experimental study tackles the question how oxide ceramics (ZrO_2 and HfO_2) respond to the simultaneous exposure to two extreme conditions, pressures up to several ten GPa and irradiation with highly energetic (MeV-GeV) heavy ion projectiles. The combination of these two extreme conditions influences the materials in ways none of those two conditions alone could.
In both materials, the exposure to high-fluence irradiations at ambient pressure result in a crystalline-to-crystalline phase transformation from the monoclinic into the first high temperature tetragonal phase. For heavy ions such as Xe, Au, Pb, and U this structural change requires a double impact process. For light ions such as Ni and Cr, the transferred energy does not suffice to induce any transformation indicating an energy loss threshold in ZrO_2 as well as in HfO_2. If the irradiation is performed under high pressure, the monoclinic-to-tetragonal transformation occurs already at a fluence that is more than one order of magnitude lower, suggesting a single-hit process. Although the ZrO_2 and HfO_2 behave much alike as no two other compound materials, their response to the combination of pressure and ion irradiation differs. X-ray diffraction analysis of the irradiated, pressurized samples and Raman and TEM measurements at ambient conditions revealed that the monoclinic-to-tetragonal transformation in ZrO_2 around 10 GPa is not direct but includes a detour into the cubic high-temperature phase, before the tetragonal structure becomes stable under decompression. For HfO_2, high fluence irradiation at 10 GPa results in the intensification of the first high pressure phase which is afterwards stabilized to ambient conditions. At higher pressures, additional ion irradiation forces both ceramics to perform a transition into their second high pressure phase (orthorhombic-II) far away from its stability field. This study demonstrates that the combination of ion irradiation and high pressure can serve as a trigger for transitions into different phases and as stabilization mechanism of usually unstable structures.

Zusammenfassung

Diese experimentelle Arbeit beschäftigt sich mit der Frage, wie sich Oxidkeramiken (ZrO_2 und HfO_2) unter der gleichzeitigen Einwirkung von zwei extremen Umgebungsbedingungen, nämlich hohen Drücken von mehreren 10 GPa und Schwerionenbestrahlung im MeV-GeV Bereich verhalten.
Unter der Bestrahlung mit sehr hohen Fluenzen vollführen beide Materialien einen strukturellen Übergang von der monoklinen zur tetragonalen Hochtemperaturphase. Für schwere Ionen so wie Xe, Au, Pb und U ist für diesen Übergang ein doppelter Ioneneinschlag und daher eine sehr hohe Fluenz von Nöten. Für leichtere Ionensorten so wie Ni und Cr, reicht die von den Ionen an das Material übertragene Energie nicht aus um einen Phasenübergang zu induzieren, was auf eine Energieverlusstschwelle sowohl in ZrO_2 als auch in HfO_2 hinweist. Falls die Bestrahlung mit schweren Ionen unter Druck stattfindet, verringert sich die für die Transformation benötigte Fluenz um mehr als eine Größenordnung, was auf einen einfachen Ioneneinschlagprozess hindeutet. Auch wenn die beiden Keramiken ZrO_2 und HfO_2 sich so ähnlich sind wie keine zwei anderen Verbindungen, zeigen sie unter der gleichzeitigen Einwirkung von Druck und Bestrahlung ein unterschiedliches Verhalten. Röntgenbeugung an den unter Druck stehenden Proben, und Raman Spektroskopie so wie TEM Messungen bei Umgebungsbedingungen zeigten, dass im Falle von ZrO_2 der Übergang von der monoklinen in die tetragonale Phase nicht direkt, sondern über einen Umweg in die kubische Phase von statten geht, bevor nach Druckentlastung die tetragonale Phase stabil wird. In HfO_2 führt die gleiche Bestrahlung bei 10 GPa zu einer stärkeren Ausprägung der instabilen ersten Hochdruckphase (orthorhombisch-I), welche dann auf Umgebungsbedingungen überführbar ist. Bei wesentlich höheren Drücken führt eine zusätzliche Ionenbestrahlung zu einem Übergang in die zweite orthorhombische Hochdruckphase weit entfernt von deren Stabilitätsfeld. Diese Arbeit zeigt, dass die Kombination von Schwerionenbestrahlung und hohen Drücken als Auslöser für Transformationen in neue Phasen und zur Stabilisierung von normalerweise instabilen Strukturen dienen kann.

Contents

1 Introduction

The development of new materials with novel and/or improved characteristics is important to meet the demands of tomorrows technological applications. This concerns in particular the performance in extreme environments such as thermo-mechanical extremes, severe radiation environments or chemical reactive conditions. In the search for materials with enhanced properties, structural diversity plays an important role. Possible parameters to control and tune structural configurations are high pressure and high dose irradiations. Of particular interests are swift heavy ions of MeV-GeV energy because they deposit energy of the order of several keV per nm along each individual ion trajectory.

In the past, the response of many different kinds of solids to such ion beams has been studied in detail. The formation of ion tracks and other damage phenomena are known for many insulators (e.g., polymers, oxides, garnets, ionic crystals,...), several semiconductors, and a few metals [1]. There are several different ways how a given material handles this huge energy input. In many crystals, the ions create an amorphized cylindrical region which in some cases can be exploited to fabricate nanostructures within a solid matrix [2]. More radiation resistant materials sometimes respond by a transition into another crystalline phase [3] which is important since the tuning of atomic structures of different phases allows the optimization of a variety of material properties.

Compared to radiation damage, the behavior of solids under high pressure is generally much better understood. Depending on the phase diagram, the high-pressure phase of some materials is characterized by enhanced physical and chemical properties such as excellent conductivity or extreme hardness. Unfortunately most high pressure phases can usually not be stabilized to endure at ambient conditions. Over many years, the search for novel (e.g. superhard) materials has stimulated activities in the high pressure community [4, 5]. It is generally assumed that a material becomes harder under pressure by decrease of its volume, either within a single phase, or via a volume-reducing phase transition. As a result, if high pressure phases could be recovered at ambient conditions, this may provide a promising route for the synthesis of materials with enhanced mechanically properties [6].

Recent developments in the pressure cell technique (e.g. by new designs of diamond anvil cells) allow access to extreme pressures up to 500 GPa, which is even much higher than the pressure in the inner core of the Earth (330-365 GPa) [7]. But even though it is nowadays possible to cover a very large pressure regime and create previously unknown material structures with enhanced properties, one still needs to find a way to stabilize these materials in their newly found forms to ambient pressure in order to access their properties for technological applications [4].

The novel approach of this project is the simultaneous exposure of materials to two different extreme conditions, pressure and high radiation dose. The experiments consist of heavy ion irradiations of pressurized samples introducing extreme energy densities and opening new routes to high temperature and high pressure phases within the $p - T$ phase diagram. The high energy in combination with severe disruption of the electronic structure provides new possibilities for the pressurized solid. As will be demonstrated, the irradiation of a pressurized crystal may allow us to recover high-pressure phase to

ambient conditions. Pressure applied during irradiation opens physical access to a large variety of structural conformations of the starting material. However, additional pressure can hinder or enhance certain radiation induced transformations [8]. Conversely, ion irradiation can change the stability field of some materials.

The idea to combine ion irradiation and pressure originated from a problem in the geoscience community. Ion irradiation occurs naturally in minerals due to spontaneous fission of radioactive nuclides such as ^{238}U that are incorporated in the material during the crystallization process. In the course of a geological time period, these unstable incorporations decay via α-particle emission or by spontaneous fission. In many minerals, the energy of the daughter nuclides is high enough to form damage tracks which can be revealed by chemical etching. Because of the long half life of ^{238}U (10^{15} a) and low concentrations, the amount of formed tracks is usually limited to a number that can be counted under an optical microscope. The amount of fission tracks is proportional to the amount of incorporated ^{238}U and thus to the age of the sample. Fission track dating requires to quantify the number of tracks and is an important tool for geochronology. Since most of these fission tracks are produced in the Earth's crust under elevated temperatures and pressures, the question arose whether track formation is influenced by the given temperature and pressure conditions. Lang et al. first simulated fission track production with an ion beam at elevated pressures and temperatures and found that the formation of tracks is not suppressed under crust conditions. The track size however, is influenced slightly [9].

This study focuses on the radiation and pressure response of dioxide ceramics ZrO_2 and HfO_2 which have a wide range of applications due to their high fracture toughness, extraordinary heat resistance and especially their chemical inertness. Besides industrial and medical applications as cladding material, oxygen sensor, tooth or hip implants, it is used as containment material for radioactive waste or inert matrix fuel in order to utilize reprocessed plutonium in nuclear reactors [10]. The two ceramics are chosen because of their radiation resistance, their high melting point ($>$ 3000 K) and low chemical reactivity with the reactor water [11]. Since fission fragments from the nuclear fuel produce an radiation field, a better understanding and reliable long-term predictions of the material behavior under such extreme conditions are needed for reliable lifetime estimates. Motivated by more fundamental aspects, it is of great interest to investigate the structural diversity of ZrO_2 and HfO_2 that both have 5 different structural polymorphs. The natural monoclinic form of ZrO_2 is of potential interest as reference for spent ZrO_2 based inert matrix fuels [12]. Both ceramics have two high pressure phases which are considered as very promising candidates for ultra hard materials [13].

Because compression can result in entirely new reactivity, bonding and structure of the material [14], the transition mechanisms between the different polymorphs are therefore investigated with regard to their stability to either ion irradiation (up to fluences of 1×10^{13} ions/cm^2) or high pressures (up to 70 GPa) and the combination of these two extreme conditions. Pressure onto the samples is applied by use of diamond anvil cells (DAC). All ion irradiations were performed at the GSI Helmholtz Center for Heavy Ion Research providing beams of all ion species in the energy regime between 10 and 90 % of the speed of light. Given by the need of large ion ranges to penetrate the cell and sample, energies of several tens of GeV provided by the heavy ion synchrotron (SIS) are necessary. Irradiations of unpressurized samples were conducted at the linear accelerator (UNILAC). The samples were investigated by means of Raman spectroscopy, high resolution X-ray diffraction (performed at DESY, Hamburg), and transmission electron

microscopy. Both irradiation and high pressure induce structural phase changes in the materials. The exposure of pressurized ZrO_2 and HfO_2 samples to the ion beams also provides insights into the beam induced phase transitions. Both conditions can partially substitute each other: the ion beam can induce phase transitions far away from the usual transition pressure. Similarly, high pressure can mimic the damage induced by dense ion irradiation. In HfO_2, a usually non-quenchable high-pressure phase can be recovered to ambient conditions when irradiated. This ion-beam stabilized sample remains stable in its high-pressure phase to this day.

This methodological approach provides a powerful tool to gain access to unique, unstable high pressure-phases and recover them to ambient conditions. This might lead to a future use of new materials which have so far been inaccessible.

2 Theory

2.1 Radiation effects in solids

When solids are exposed to heavy ion irradiation, several kinds of effects occur within the material. Most of the energy introduced into the solid is transformed to lattice vibrations (heat) or luminescence but some part is used to create defects such as e.g. lattice distortions, vacancies, interstitials, amorphization, ... [15]. The defect creation mechanism is discussed in the following sections.

2.1.1 Energy loss

When fast heavy ions traverse a solid, several different processes emerge. On the way through matter, the ion projectiles slow down because they transfer their kinetic energy onto the target. In most materials a long damage region with a diameter of a few nm is produced along the trajectory of the ion, a so-called ion track [16]. The energy deposition in the material is crucial for the defect production and is expressed by the stopping power or energy loss which is the average loss of kinetic energy per unit path length

$$S(E) = -\left(\frac{dE}{dx}\right) \tag{2.1}$$

The common unit of the energy loss is keV/nm. The energy loss processes for ions can roughly be classified into six groups [17]:

- excitation and ionization of target electrons
- excitation and ionization of the projectile
- electron capture
- recoil loss
- electromagnetic radiation
- elastic collisions

For high initial specific ion energies ($\geq$ 1 MeV per nucleon), excitation and ionization of target electrons is the dominating process, except for at the low-speed end, at which the interaction with target atoms occurs. To what extent the different mechanisms play a role depends strongly on the kinetic energy and charge state of the projectile ions. There exist two velocity-dependend kinds of energy loss adding up to the total energy loss $S_{total} = S_n + S_e$.

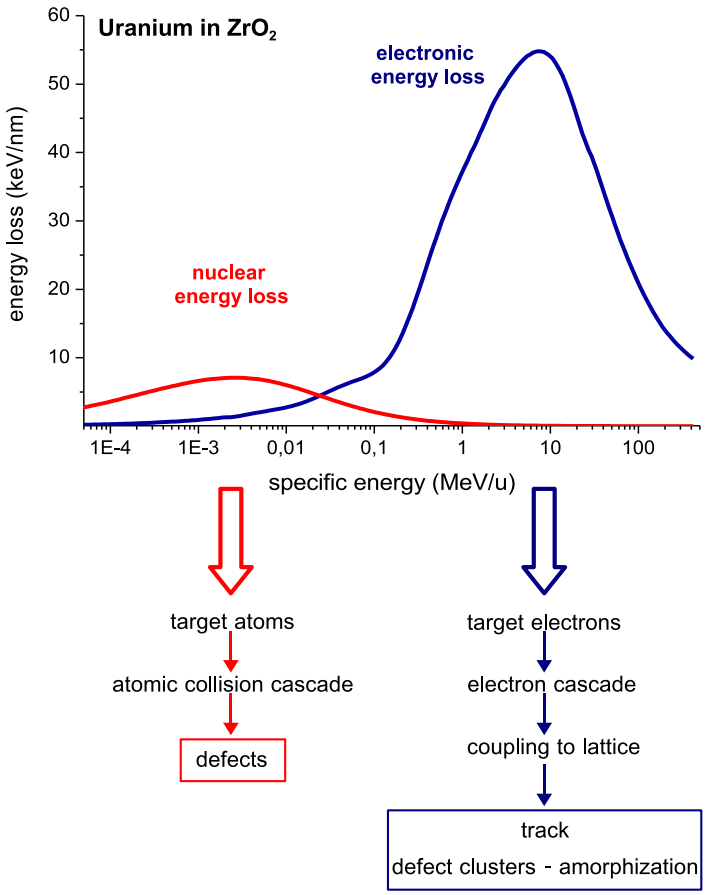

Figure 2.1: Electronic and nuclear energy loss of uranium ions in ZrO_2 versus the specific ion energy. The maximum of the electronic energy loss region is called Bragg maximum or Bragg peak.

- nuclear energy loss, S_n (for specific energies lower than $\sim$ 100 keV/u)
- electronic energy loss, S_e (for specific energies larger than $\sim$ 1 keV/u)

2.1.1.1 Nuclear energy loss

For kinetic energies of the projectile, less than 100 keV/u, the nuclear energy loss is dominating with its maximum at $\sim$ 1 keV/u (see Fig. 2.1). The velocity of the ion is then slow compared to its shell electrons. The nuclear energy loss is important in the last hundred 100 nm of the ion trajectory. Typical processes are elastic collisions of projectile and target atoms (knock-on processes). This causes displacements of the atoms from their initial lattice sites and lattice vibrations. Displacement of target atoms occurs for as long a the ion energy is larger than the needed displacement energy. Also recoils are produced during these hit processes. As mentioned before, the influence of the nuclear energy loss becomes negligible above 100 keV/u. Because our experiments were always performed with energies well above 1 MeV/u, the electronic energy loss is dominating and the nuclear energy loss is not taken into consideration. Especially for the high-pressure experiments, the ions are stopped several μm behind the sample so that no kind of nuclear stopping occurs.

2.1.1.2 Electronic energy loss

Above energies of 100 keV/u, the electronic energy loss is the dominating process. The projectile ionizes and excites the target electrons. Because of the high speed, no strong interaction takes place with the target nuclei. Also, the momentum transferred to the target electrons is very small compared to the available kinetic energy of the projectile because of the small electron mass. Thefore, the projectile is only slowly decelerated without changing its direction. The overall course of the energy loss of an ion in a medium depends on the ion velocity v_p and its charge state and can be described by the Bethe-Bloch formula, which considers the momentum transfer to a target electron in a Coulomb potential plus correction terms [18, 19, 20].

$$\left(-\frac{dE}{dx}\right)_e = \frac{4\pi\,(Z_p^{eff})^2\,Z_t\,N_t}{m_e\,v_p^2} * \left(ln\,\frac{2m_e v_p^2}{I} - ln\,(1-\beta) - \beta^2\right) \tag{2.2}$$

- Z_p^{eff} = effective charge of the projectile
- Z_t = atomic charge of the target material
- N_t = amount of target atoms per volume unit
- m_e = electron mass
- e = electron charge
- I = effective ionization potential of the target material
- β = ratio between ion velocity and speed of light

2.1.2 Effective charge state

An important correction factor takes into account the shielding of the nuclear charge of the projectile because of its bound electrons. By passing through a solid, the projectile ion loses these electrons whose orbital velocity (v_0) is smaller than the projectile velocity (v). This is called Bohr's stripping criterion. Therefore, one has to consider the charge exchange between the projectile ion and the solid. The more loosely bound outer electrons are easily stripped off during the scattering process with the target material. This leads to an effective charge state Z_p^{eff} of the projectile which is smaller than the nuclear charge number Z_p and can be expressed by the following formula [19].

$$Z_p^{eff} = Z_p\left[1 - exp\left(\frac{-v/v_0}{Z^{2/3}}\right)\right] \tag{2.3}$$

Starting at very high initial kinetic energies, the electronic energy loss increases by a factor of $\frac{1}{E}$ when the ion is decelerating (see Fig. 2.1). This is due to the fact that with decreasing ion energy the time

for interactions between projectile and target increases and higher momentum transfer becomes possible. When the velocity of the ion approaches the average orbital velocity of the target electrons, the momentum transfer is most efficient and the stopping curve has its maximum at about 5 MeV/u (see Fig. 2.1) [21]. This maximum is called Bragg maximum or Bragg peak. The energy loss decreases quickly with $\sqrt{E}$ below the Bragg peak, because the loss of the effective charge (electron capture) becomes a dominating factor until the nuclear stopping takes over. Besides the effective charge, there are a few more correction factors have to be taken into considereation. Because Bethe derived his formula using quantum mechanical perturbation theory, his result is proportional to the square of the charge Z_p. The description can be improved by considering corrections which correspond to higher powers of Z.

The penetration depth of an ion with an initial kinetic energy E_0 in a specific material until it is stopped completely is called the ion range. The total range R is obtained by integration of the inverse stopping power of the medium over the energy.

$$R = \int_0^{E_0} \left(\frac{dE}{dx}\right)^{-1} dE \tag{2.4}$$

The path of the ion can be considered as straight. R describes the mean range, because not every ion of an ensemble transfers the same amount of energy to the target. Therefore, some ions still have some small amount of kinetic energy when they reach the calculated mean range whereas others have before already transferred all their energy to the target material. This range distribution at the end of the trajectories is called ion straggling. In this work, the values of energy loss and ion range were calculated with the SRIM2008 (Stopping and Range in Matter) code which has an accuracy of about 15% [22].

2.1.3 Track formation and defect creation mechanism

Swift, highly charged ions transfer their kinetic energy by ionization of target atoms, and therefore produce free electrons that further ionize more atoms causing ionization cascades. Also Auger electrons can be produced if electrons from a lower shell are ejected. In our kind of experiments, the energy of the primary electrons is usually in the order of several keV, allowing several steps of free electron production. All secondary and higher-order follow-up electrons are called δ-electrons. These ionization processes happen on a very short time scale (primary electrons $\sim 10^{-17}$ - 10^{-16} seconds), so that after around 10^{-14} seconds the δ-electron cascades have ended [16]. The energy deposition of the projectile follows a radial distribution of $\sim 1/r^2$ (with r denoting the radial distance from the ion trajectory) leading to a formation of cylindrical damage regions [23]. In these cylindrical ion tracks, the defect distribution is inhomogeneous with a high defect concentration close to the ion trajectory, surrounded by a halo of lower defect concentration. The overall damaged region can be up to several 10 nm depending on the target material. All of these mentioned processes occur without interaction with the target lattice. Only after relaxation times $\tau \geq 10^{-13}$, which correspond to a period of a lattice vibration, coupling to the lattice is possible. The question by which mechanism or mechanisms the ion energy is transferred to the

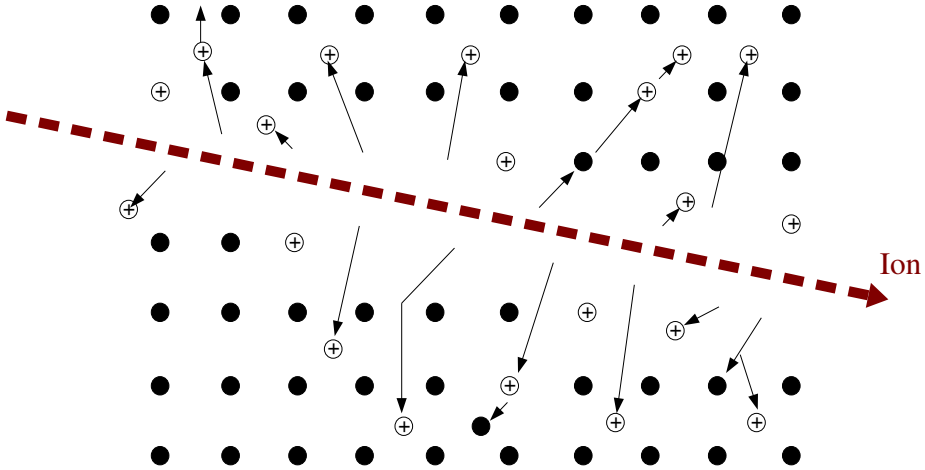

Figure 2.2: Schematic view of ion displacements as a result of ionization along the path of an ion

lattice is still not solved, and very difficult to answer experimentally. In the following paragraph, the two most promising models, namely Coulomb explosion and thermal spike, will be discussed.

2.1.3.1 Coulomb explosion

The Coulomb explosion or ionic spike model was introduced by Fleischer et al. in the 1960s, trying to describe the track formation in insulating materials [24]. In this model, the track formation is subdivided into several steps. When the ion passes through matter, an ion cloud is formed along its path. The corresponding δ-electrons fly away perpendicular to the ions path and leave back a narrow cylinder which is densely filled with excess positive ions. These positive lattice ions now repel each other and are ejected into interstitial positions [16, 24]. The ejected target ions will eventually neutralize and the high local lattice strains are compensated by relaxation and other readjustments to a larger volume of the target. Hereby, a cylindrical core with huge vacancy concentration surrounded with atoms on interstitial planes is created. The radii of these ion tracks is typically in the region of several nm but depend strongly on energy, charge state, and mass of the projectile ion as well as on the thermal stability and free electron density of the target material. Several criteria have to be fulfilled for the Coulomb explosion to happen. First of all, the Coulomb repulsive forces within the ionized region must be high enough to overcome the lattice bonding forces. If two ions in a material of dielectric constant ϵ and average atomic spacing a_0 have received an average ionization of n unit charges e, the force between them is $n^2e^2/\epsilon a_0^2$. If n is high enough, the electrostatic stress will be larger than the mechanical strength. This shows that the tracks are formed more easily in materials of low mechanical strength, low dielectric constant, and close interatomic spacing. Another very important criterion relates to the supply of electrons near the ionized track. The repulsion of the ionized target ions and therefore displacement from their original sites has to be faster than the time for recombination between target ions and electrons of $\sim 10^{-13}$ seconds. The density of free electrons has to be low enough for a track to be formed. This is usually the case for insulators and semiconductors. In metals, on the other hand, the density of free conduction electrons is

so high that the ionized target atoms become neutralized almost immediately. Model calculations show that in the case of metals only $\sim$ 0.001 % of the deposited energy would be available for dislocations [25].

2.1.3.2 Thermal spike

The thermal spike model, first proposed by Dessauser [26] and further developed by other groups [27] and especially by Toulemonde et al. [28, 29, 30], concentrates on the defect creation caused by a huge temperature increase along the ion trajectory. The energy of the incoming ion is first transferred to the electrons. This leads to a rapid local heating of the electron subsystem to a temperature T_e, comparable to the Fermi energy E_F along the ion trajectory, which expands as far as the δ-electrons travel [31]. A highly non-equilibrium region, with hot electrons and cold lattice, arises [29]. The energy of the electrons is then transferred to the atomic subsystem via electron-phonon coupling leading to a large temperature increase of the target crystal atoms T_a. The temporal and spatial development of the electron and lattice temperature can be described by the following two coupled differential equations [32]:

$$C_e(T_e)\frac{\partial T_e}{\partial t} = \frac{1}{r}\frac{\partial}{\partial r}\left[rK_e(T_e)\frac{\partial T_e}{\partial r}\right] - g(T_e - T_a) + A(r,t) \tag{2.5}$$

and

$$C_a(T_a)\frac{\partial T_a}{\partial t} = \frac{1}{r}\frac{\partial}{\partial r}\left[rK_a(T_a)\frac{\partial T_a}{\partial r}\right] + g(T_e - T_a) \tag{2.6}$$

with $C_{(e,a)}$ representing the specific heat and $K(e,a)$ the thermal conductivity of the electronic ($_e$) and lattice ($_a$) subsystems, and r the radius of a cylindrical track with the heavy-ion trajectory as symmetry axis. $A(r,t)$ is the energy deposited on the electronic subsystem at a time t and a distance r. The only free parameter is the electron-phonon coupling constant g which is directly linked to the electron mean free path $\lambda = K_e/g$ [30]. These differential equations can not easily be solved since the electron and lattice systems are not in equilibrium. Under certain conditions (low melting point, strong electron-phonon coupling) a local melting along the ion trajectory can occur. Due to rapid quenching, "frozen" defects are created and form the ion track. As for the Coulomb explosion model, the lack of ion tracks in metals is explained by the high density of free electrons. The energy transferred from the ion to the electrons diffuses quickly into a larger volume, hindering a strong heating that could lead to melting of the lattice.

Both models have good arguments to explain the radiation defect creation mechanism. It might be that the Coulomb explosion processes (atomic motion) occur but are later annealed by the slower thermal spike process in the lattice (10^{-13} - 10^{-12} s) [32]. Until now, no experimental proof for one model or the other has been presented, leaving both mechanisms as possible explanations.

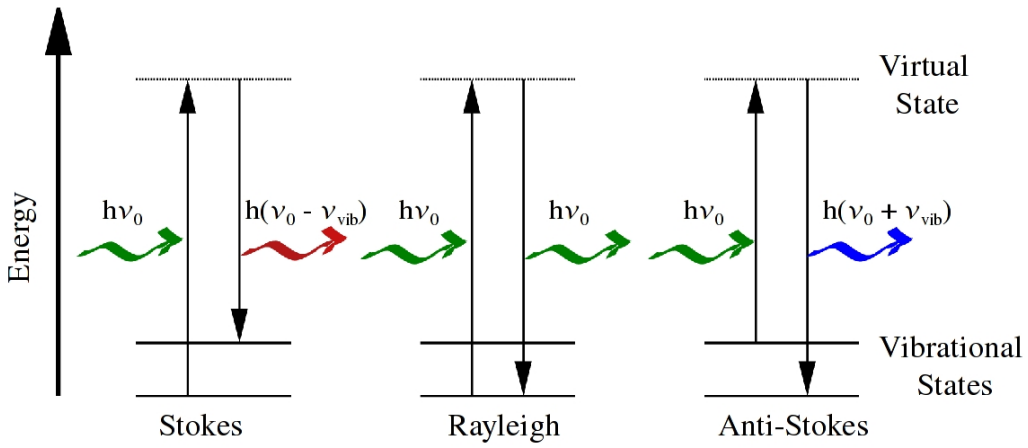

Figure 2.3: Energy level diagram for Rayleigh and Raman scattering processes.

2.2 Raman spectroscopy

The Raman effect was experimentally discovered by the Indian physicist Chandrasekhar Venkata Raman in 1928. He observed that a sample illuminated with monochromatic light not only re-emits light with the same energy (Rayleigh scattering) but also a small component of higher or lower frequency compared to the incident light. Since then, Raman spectroscopy has become (next to IR spectroscopy) an important method for the analysis of vibrational states of gasses, liquids, and solids. It offers the combination of spatial resolution ($\sim 1\ \mu$m) and physical/chemical characterization without destroying the sample.

2.2.1 Raman effect

When light hits matter it interacts with the electrons of the material. If the energy of the incident light matches exactly the energy of an electronic transition, an electron is transferred to the excited state and the energy of the incident light will be absorbed. This happens in the case of IR spectroscopy. If no absorption occurs, the incoming light causes a distortion of the electron cloud of the material and due to relaxation the light with the same wavelength is re-emitted. This elastic scattering process (called Rayleigh scattering) happens in most of the cases. In some cases, the induced distortion of the electron cloud interacts with the motion of the molecules (vibration, bending, rotation). Energy of the incoming light is transferred to the molecule, therefore changing the frequency of the scattered light. This inelastic process is called Raman scattering.

The Raman effect can be best described with an energy level diagram as in Fig. 2.3. In contrast to IR spectroscopy, light with one certain wavelength is used to illuminate the sample, therefore lasers with a fixed wavelength are used. The incoming light excites the molecules into a virtual state which is not an eigenstate of the molecule. This virtual state is a distortion of the electron cloud of a covalent bond introduced by the interaction of the laser light with the electrons. The virtual state is unstable and the photon will be scattered instantaneously. The energy of the virtual state is determined by the frequency

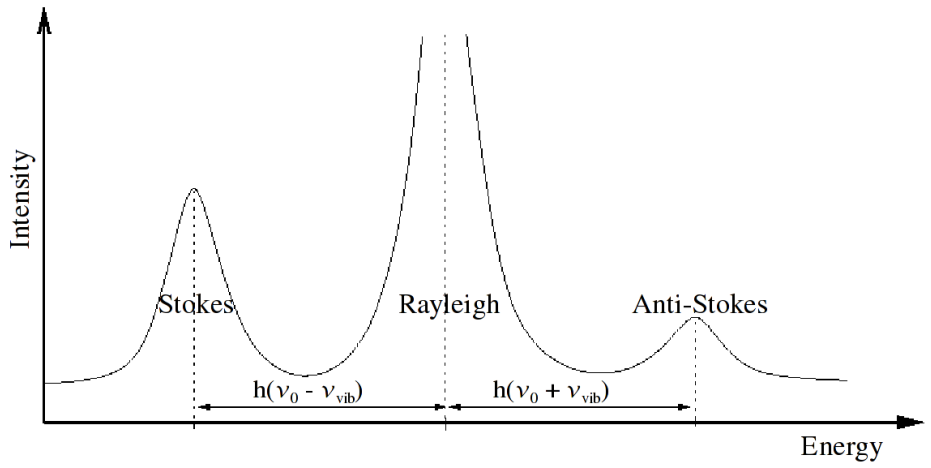

Figure 2.4: Schematic of the intensity distribution of Rayleigh-, Stokes-, and anti-Stokes scattering peaks.

of the exciting light. For the scattered light therefore exist three possibilities:

Rayleigh scattering:

Most of the incoming light experiences elastic backscattering (see Fig. 2.3 center). The incoming photons cause a distortion of the electron cloud causing an excitation of the molecule to the virtual state but the nuclei themselves possess too much inertial mass, making it impossible to follow the electron cloud movement. No energy will be transferred during this process and the electron cloud relaxes to its initial state emitting a photon of the same frequency as the incident light.

Stokes scattering:

In a few cases (one out of 10^6-10^8 photons), the incoming light interacts with the electrons and the nucleus begins to move at the same time. Part of the incoming energy is then transferred to the movement of the molecule, creating a vibrational phonon. When the electrons then relax back from the virtual state, the emitted light has less energy than before ($E_{scatt} = h(\nu_0 - \nu_{vib})$). This is called *Stokes scattering* (see Fig. 2.3 left).

Anti-Stokes scattering:

Due to thermal activation, about 1% of the molecules are already in the excited vibrational state. Some of these molecules transfer part of their energy to the incoming photon during the scattering process, destroying a vibrational phonon. Therefore, the emitted photon has a higher energy than before ($E_{scatt} = h(\nu_0 + \nu_{vib})$). This is called *Anti-Stokes scattering* (see Fig. 2.3 right).

At ambient conditions and thermal equilibrium, more molecules are in the vibrational ground state (m) than in the excited state (n). The intensity of anti-Stokes scattering is therefore much less than for Stokes scattering (see Fig 2.4). If not specifically mentioned otherwise, speaking about Raman scattering always means Stokes scattering.

As mentioned before, only one out of 10^6-10^8 photons is Raman-scattered. The elastically scattered light (Rayleigh peak) displayed in Fig. 2.4 is much stronger and has to be removed by filtering when looking at Raman spectra. The intensity of the scattered light is proportional to the amount of excited molecules. The intensity of Stokes scattered photons is therefore proportional to the amount of molecules

in the vibrational ground state, while the intensity of anti-Stokes scattered photons is proportional to the amount of molecules existing already in the excited vibrational state. The ratio of excited state to ground state and thus the ratio of anti-Stokes to Stokes scattering can be calculated via the Boltzmann equation:

$$\frac{N_n}{N_m} = \frac{g_n}{g_m} e^{-\frac{(E_n - E_m)}{kT}} \tag{2.7}$$

N_n: number of molecules in the excited state (n)
N_m: number of molecules in the ground state (m)
g: degeneracy of states n and m
$E_n - E_m$: energy difference between these two states
k: Boltzmann constant ($1.3807 \cdot 10^{-23}$ JK^{-1})
T: temperature in Kelvin

For well-calibrated systems, it is even possible to determine the temperature of the sample under study using the intensity ratios of Stokes and anti-Stokes peaks.

2.2.2 Raman theory

Raman spectroscopy provides information about vibrational energy levels of a molecule or structural group. Whether a vibration is Raman active depends on the change of the polarizability of the electron shells. When polarized light interacts with a molecule, the electron cloud of this molecule will be deformed relative to the atoms introducing a dipole moment μ which is proportional to the electric field.

$$\vec{\mu} = \alpha \cdot \vec{E} \tag{2.8}$$

with

$$\vec{E} = \vec{E}_0 \cdot cos(2\pi\nu_0 t) \tag{2.9}$$

α represents the degree of the possible deformation of the electron cloud and is called polarizability.

Although the incoming light is polarized in one plane, the effect on the electron cloud is not necessarily limited to that plane. Therefore, the full dipole has to be represented with the polarizability tensor:

$$\begin{pmatrix} \mu_x \\ \mu_y \\ \mu_z \end{pmatrix} = \begin{pmatrix} \alpha_{xx} & \alpha_{xy} & \alpha_{xz} \\ \alpha_{yx} & \alpha_{yy} & \alpha_{yz} \\ \alpha_{zx} & \alpha_{zy} & \alpha_{zz} \end{pmatrix} \cdot \begin{pmatrix} E_x \\ E_y \\ E_z \end{pmatrix} \tag{2.10}$$

where the first subscript refers to the direction of polarizability of the molecule and the second subscript to the polarization of the incident light. If α is constant in time, Eq. 2.8 describes a constant oscillating dipole moment with only the initial vibration frequency ν_0 which can be observed in the

Rayleigh peak. If the excited molecule performs a vibration with a frequency ν_{vib}, it causes a time variation of the polarizability and α changes to:

$$\alpha = \alpha_0 + \left(\frac{\partial \alpha}{\partial Q_{vib}}\right)_0 Q_{vib} \tag{2.11}$$

where Q_{vib} is the normal coordinate of the vibration. Developing the polarizability as Taylor expansion around the equilibrium, one will obtain the following expression for the dipole moment:

$$(t) = \underbrace{\alpha_0 E_0 cos(2\pi\nu_0 t)}_{Rayleigh} + \underbrace{\frac{1}{2}\left(\frac{\partial \alpha}{\partial Q_{vib}}\right)_0 Q^0_{vib} E_0 cos(2\pi(\nu_0 - \nu_{vib})t)}_{Stokes} + \underbrace{\frac{1}{2}\left(\frac{\partial \alpha}{\partial Q_{vib}}\right)_0 Q^0_{vib,} E_0 cos(2\pi(\nu_0 + \nu_{vib})t)}_{Anti-Stokes} \tag{2.12}$$

Equation 2.12 expresses that a molecule vibration changes the frequency of the induced dipole moment. Besides the incident frequency, then two additional frequencies with $(\nu_0 \pm \nu_{vib})$ occur. Only if

$$\left(\frac{\partial \alpha}{\partial Q_{vib}}\right)_0 \neq 0 \tag{2.13}$$

these two additional frequencies appear, which means that the change of polarizability is the condition for the Raman effect [33, 34, 35, 36, 37].

2.3 X-ray diffraction

X-rays can be produced either by slowing down highly energetic electrons in matter (producing the so-called bremsstrahlung) or by recombination processes of electrons [38]. In the first case, the emitted X-ray can have a continuum of different frequencies, while in the second case, sharp lines are emitted corresponding to the transition between electronic shells.

Because the wavelengths of X-rays are comparable to the atomic distances in a solid ($\sim$ 1 pm up to 10 nm), X-ray diffraction is a powerful non-destructive method to analyze the crystal structure of materials. X-ray diffraction results from the interaction of the X-ray with the electrons of the material under study. Depending on the atomic arrangement of the material, the scattered rays interfere constructively when the paths of the diffracted rays differ by an integral number of wavelengths [39]. This selection condition is given by Bragg's law:

$$2 \cdot d_{hkl} \cdot sin\Theta_{hkl} = n \cdot \lambda \tag{2.14}$$

where λ is the wavelength, d_{hkl} the spacing between the planes in the atomic lattice, θ_{hkl} the angle between incident and scattered rays, and n the order of constructive interference. The principle of Bragg's scattering geometry is displayed in Fig. 2.5.

Each X-ray diffracted by an atom, sends out a spherical wave with this atom (or more precisely the electron cloud of the atom) as diffraction center. Bragg's law determines in which direction (2 θ) the interference of the diffracted waves is constructive. When the wavelength λ is known, one can obtain the

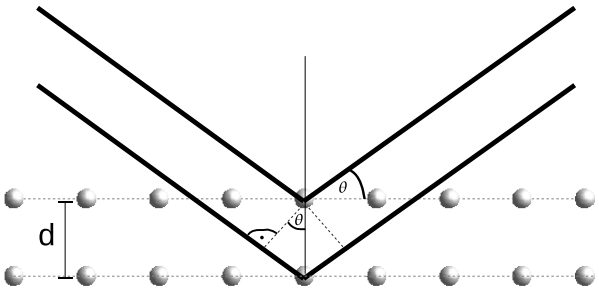

Figure 2.5: Principle of Bragg scattering geometry.

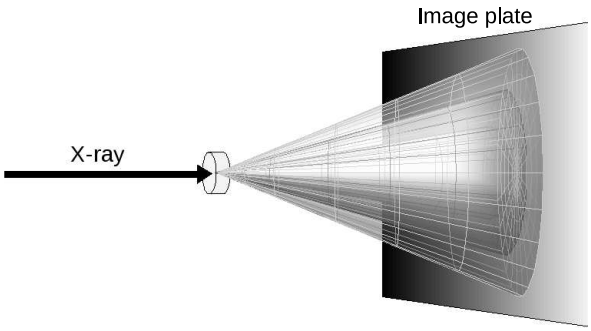

Figure 2.6: Debye-Scherrer geometry for powder diffraction measurements.

lattice plane d-spacings d_{hkl}. If the crystal system is known, the lattice constants of the crystallographic unit cell can be derived from d_{hkl}:

$$d_{hkl} = \frac{1}{\sqrt{(\frac{h}{a})^2 + (\frac{k}{b})^2 + (\frac{l}{c})^2}} \tag{2.15}$$

with a, b, and c denoting the lattice constants of the unit cell [40]. For crystals with higher symmetry (eg. cubic $a=b=c$) it becomes easier to solve the equation.

Any diffraction process can be described by a Fourier transformation from crystal space into reciprocal space yielding data in reciprocal space [39]. The measured intensities I_{hkl} are directly proportional to the square of the crystallographic structure factors F_{hkl}. The structure factor depends on the kind of atoms and their positions in the unit cell and is the Fourier transformation of the electron density distribution $\rho(x,y,z)$ [40]. In practical applications, the Fourier method is seldomly used. One rather uses the Fourier sum of all atomic scattering factors f_i of all N atoms i in one unit cell [41].

$$F_{hkl} = \sum_{i=1}^{N} f_i e^{2\pi i(hx_i + ky_i + lz_i)} \tag{2.16}$$

2.3.1 Powder diffraction

For diffraction analysis of single crystals the Laue method is typically used. For the Laue method, non-monochromatic X rays (bremsstrahlung) are used so that several lattice planes fulfill the Bragg condition simultaneously. Constructive interference only occurs if the change of the wave vector is equal to the reciprocal lattice vector during the scattering process [40]. The scattered image shows point reflections.

In the case of powdered samples (as used in this study) the Debye-Scherrer method is preferably used. For diffraction experiments, an ideal powder consists of numerous small, randomly oriented crystallites. Usually, there are enough crystallites in all possible diffracting orientations. For the powder diffraction technique, it is essential to use a narrow beam of monochromatic X-rays. If monochromatic x rays hit a fine powder of randomly oriented particles, a pattern as in Fig. 3.9 occurs. The diffracted rays from

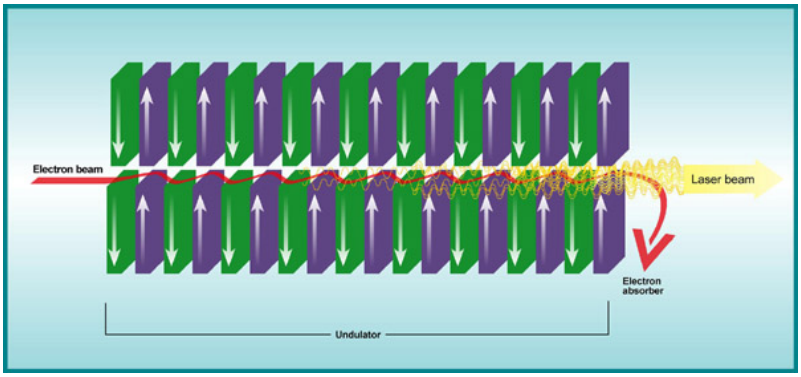

Figure 2.7: Schematic of a dipole structure which forces an electron beam to perform direction changes thus emitting syncrotron radiation primarily in forward direction. Behind the undulator, the electron beam is absorb via an electron catcher [43].

a set of planes of spacing d_1 generating a cone with an opening angle of $4\theta_1$, planes of spacing d_2 generate a cone of angle $4\theta_2$ and so on [42]. A pattern of concentric rings is produced. If the number of orientations of the crystallites is too small, the rings will look spotty and discontinuous. One can derive a typical diffractogram in one dimension by displaying the intensity profile along a radius of the diffraction rings.

2.3.2 Synchrotron radiation

Common X-ray tubes used in laboratories do not provide enough X-ray energy and intensity to pass through thicker or strongly absorbing materials. Especially for investigations of materials under high pressure, the energy has to be high enough to penetrate several mm of diamond. Synchrotron sources have been developed to produce much higher average brilliance B which is defined as

$$B = \frac{Number\ of\ Photons}{Time \cdot horizontal\ \&\ vertical\ size \cdot horizontal\ \&\ vertical\ divergence \cdot band\ width} \tag{2.17}$$

with usual units $N_{Phot}/(\mathrm{s} \cdot \mathrm{mm}^2 \cdot \mathrm{mrad}^2)$ [44].
In an electron synchrotron, an incandescent cathode produces free electrons which are usually transferred via a DC accelerator part into an accelerator ring, a so-called synchrotron. In such a device, the electrons are accelerated almost to the speed of light by strong high-frequency emitters in the MHz regime in resonator structures. Strong magnetic fields keep the electrons on their circular path. Even though the velocity remains constant (storage rings), the electrons constantly have to change their direction causing the emission of electromagnetic waves which are directed tangential to their trajectory, the so-called synchrotron radiation [40]. Synchrotron radiation is not monochromatic, but by using a monochromator one can more or less choose the energy of the X-rays. (The larger the radius of the ring accelerator the lower are the beam losses.) Electrons travel in bunches which are hindered to diverge by specialized magnetic lenses.
To produce large amounts of synchrotron radiation undulators are used. An undulator consists of a periodic structure of dipoles over a length of several meters, forcing the electrons on a sine-shaped path with

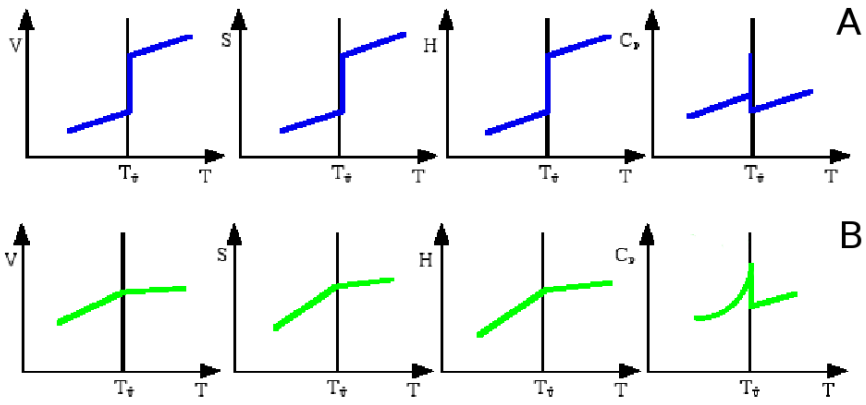

Figure 2.8: Change of different thermodynamical properties at the phase transition of first (A) or second (B) order. (V = volume, S = entropy, H = enthalpy, and C_p = heat capacity).

a wavelength λ_U. Because of the numerous trajectory changes, the electron beam is forced to undergo oscillations and thus to irradiate X-rays. If the constant magnetic field of the undulator dipoles is strong enough and the wavelength of the oscillating beam λ_U small enough, the emitted radiation displays constructive interference increasing the intensity, at certain energies, by a factor of about one thousand compared to a simple bending magnet [40, 45].

2.4 Structural phase transitions

Besides the phase transitions, considered in most cases such as e.g. solid-liquid or liquid-gaseous, there exist structural phase transitions where a solid changes from one crystalline phase into another. Under such transitions, the material does not change its chemical composition. Structural phase transitions are mainly induced by pressure, but also a change of temperature can induce a structural phase transition below the melting point. There exist materials that exhibit more than ten different crystalline phases (e.g. crystalline ice phases) [46]. Most structural transitions occur under high pressure. High-pressure phases usually arise because the new phase is more compact (higher density) and therefore shows greater thermodynamic stability. The susceptibility of solids towards phase changes depends strongly on the closeness of packing of the atoms in the low-pressure form. Crystals with relative open structures, which means low density, have a higher tendency to rearrange themself than others which are already in a high-density form [47].
A phase transition occurs when a phase becomes unstable in the given thermodynamic conditions. In thermodynamics, it is possible to show that the stable phase corresponds to the minimum of the Gibbs free energy G (also called free enthalpy) [46]:

$$G = U + pV - TS \tag{2.18}$$

where U is the internal energy, S the entropy, T the temperature, p the pressure, and V the volume. The necessary criterion for phase change is then given by $\Delta G < 0$. The pV term in Eq. 2.18 becomes

increasingly important for materials under pressure. A phase with a lower specific volume may then become thermodynamically more stable than one with lower internal energy. The pressure at which the Gibbs free energies of two phases become equal is the thermodynamic transition pressure. Usually, the application of pressure changes the specimen to the phase with higher density.
Landau theory gives a phenomenological framework to charaterise a phase transition by introducing a so-called order parameter η, which contains all necessary information (such as e.g. the degree of order or extent of deformation) of the material. The Gibbs free energy can then be expressed by a low order Taylor expansion in terms of the order parameter [48].

$$G(\eta) = G_0 + \frac{1}{2}A\eta^2 + \frac{1}{4}A\eta^4 + ... \tag{2.19}$$

where A and B are constants and G_0 is the free energy of the system for $\eta = 0$. Usually $G(\eta)$ is independent of the sign of η and therefore contains only terms with even powers. A depends on the transition temperature so that $A = a(T - T_c)$. The equilibrium condition is given for $\partial G/\partial \eta = 0$.

Phase changes are divided in transformations of first and second order. First-order tansitions are accompanied by a discontinuity of thermodynamic quantaties such as volume and entropy which are the first derivatives of the Gibbs free energy.

$$S = -\left(\frac{\partial G}{\partial T}\right)_p \qquad V = \left(\frac{\partial G}{\partial p}\right)_T \tag{2.20}$$

This kind of transition can easily be identified, because the measured property shows an abrupt jump (see blue curves in Fig. 2.8).
Second-order transitions occur when the two different structures merge continuously. This means the first derivatives are continuous while the second order derivatives become discontinuous such as specific heat C_p and compressibility κ [46].

$$\frac{C_p}{T} = -\left(\frac{\partial^2 G}{\partial T^2}\right)_p \qquad \kappa V = -\left(\frac{\partial^2 G}{\partial p^2}\right)_T \tag{2.21}$$

The production of high-pressure phases is often limited without additional catalysts. An additional activation energy has to be introduced into the system to start the transformation. The same effect hinders some high pressure phases to reconvert into their ambient form after pressure release. The best known example for this behavior is the graphite → diamond transition. The stability field of diamond under pressure already starts at around 2 GPa, but no transformation occurs at this point [49, 50]. Even pressurization up to 40 GPa cannot evoke a phase change. A lot of activation energy in the form of additional pressure and high temperature is needed to produce diamond. However, once produced,

diamond is stable enough to remain at ambient pressure conditions until another energy input (e.g. $T > 1000\,°C$) overcomes the activation barrier. The diamond structure is therefore called metastable.

Crystalline-crystalline phase transformations are often described by the similarity of the two structures. Therefore, the degree of rearrangement of the atoms can be explained. There are two main groups for structural transformations in solids.

Displacive phase transitions

This kind of transformation does not involve any long-range movements but only comparatively small motions of atoms which change the symmetry of the crystal structure. In this case, the two phases differ only slightly e.g. in lattice parameter, angle, or coordination number. Displacive transitions only need a small energy input and occur quite fast. These kinds of phase transitions can be of first or second order and are usually fully reversible [51].

Reconstructive phase transitions

This kind of transition involves a breakdown of one lattice and a reorganization into the other. The phases do not need to be similar in their structure or symmetry. The reconstructive transition is always of first order. Because of the breaking, rearrangement, and new formation of bonds, a lot of activation energy is needed for the transformation. Therefore, in some cases, fast decompression (so-called quenching) can lead to the preservation of the metastable high pressure phase even at ambient pressure. E.g. the graphite → diamond transition is of reconstructive type.

3 Experimental Setup

3.1 High-pressure technique

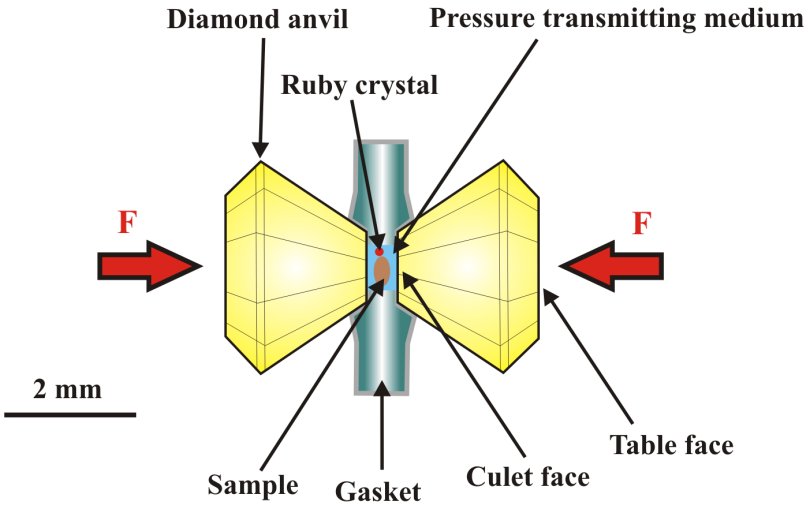

Figure 3.1: Schematic of a diamond anvil cell (DAC) [52].

3.1.1 Diamond anvil cell

There exist numerous ways to apply pressure on materials, depending on the needed pressure and sample size. There are several kinds of large volume presses which can be used for large samples and pressures up to $\sim$ 25 GPa. Further, medium-size apparatuses are available, like the Paris-Edinburgh press which was originally developed for neutron scattering measurements under pressures up to $\sim$ 12 GPa and sample volumes around $\sim$ 100 mm^3 [53, 54]. But the most common pressure apparatus is the diamond anvil cell developed in the 1960s by W. Bassett et al. which uses the simple principle $P = \frac{F}{A}$ to create high pressures by decreasing the sample area while applying moderate forces [55]. The area of the applied force is usually only a few hundred μm in diameter, and new developments in diamond cutting techniques made it possible to reach pressures up to 550 GPa [56]. The great advantage of the diamond anvil cells besides the large pressure regime is their small size and weight which allows an easy transport to different experimental sites making them quite handy [57]. A sketch of the basic principle of a DAC is shown in Fig. 3.1.

The most important parts of the DAC are the two brilliant-like cut diamonds. Diamond is the hardest material known and therefore well suited to apply very high pressures. The table face of the diamond sits on some very strong background material, the so-called diamond seat usually made of tungsten carbide (or beryllium for low-background diffraction measurements). The diamonds are either mechanically

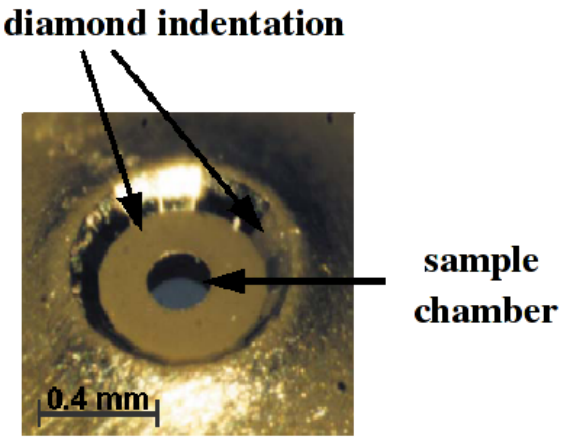

Figure 3.2: Pre-indented gasket and drilled sample chamber with a diameter of 200 μm.

fixed or glued to the seat. The size of the culet face (small front of the diamond) defines the pressures that can be reached at a given force, defined by the mechanical setup. Inside a DAC, the culet faces of both diamonds have to oppose each other perfectly. Not only the positions of the faces have to match, but also tilting between both faces cannot be tolerated. Every misalignment diminishes the reachable pressure regime. The lateral and angular positions of the diamond can be controlled via small set screws.

A thin metal gasket (e.g. hardened steel or rhenium) with an initial thickness of 250 μm is placed between the two culet faces. Then the diamonds squeeze the metal, creating a pre-indented area in form of the diamond tips to later provide stabilization of the gasket. The pre-indented area usually has a thickness of 40-80 μm. Inside this pre-indented part a small hole is drilled, either via mechanically drilling or spark corrosion, which later accomondates the sample. In this work, the drilled sample chambers ranged between 100 and 200 μm in diameter depending on the culet size and intended pressure (see Fig. 3.2). For filling of the cell, the gasket is now placed on the lower diamond. With a fine needle, the sample is placed inside the sample chamber together with a small pressure gauge (eg. ruby or quartz) and a pressure transmitting medium (e.g. a mixture of methanol, ethanol, and water or noble gases like argon). The choice of pressure medium depends on the planned pressure range and the necessity of hydrostatic or non-hydrostatic conditions, because each pressure medium has its advantages and disadvantages [58]. After the sample chamber has been filled with the sample, pressure calibrant, and pressure medium, it is quickly closed by the second diamond to avoid evaporation of the pressure medium. By tightening the screws, the diamond tips are brought closer together squeezing the sample chamber. The liquid pressure medium then transfers the increased pressure hydrostatically to the sample.

The use of natural colorless diamonds as anvils not only opens the possibility to optically observe the sample with a light microscope but enables also the in-situ application of various analytical techniques [59], especially optical vibrational spectroscopy like Raman spectroscopy.

Although they are quite handy and can create high pressures, DAC have one major drawback. The limited sample chamber volume demands accurate loading skills. Even the unloading procedure has to

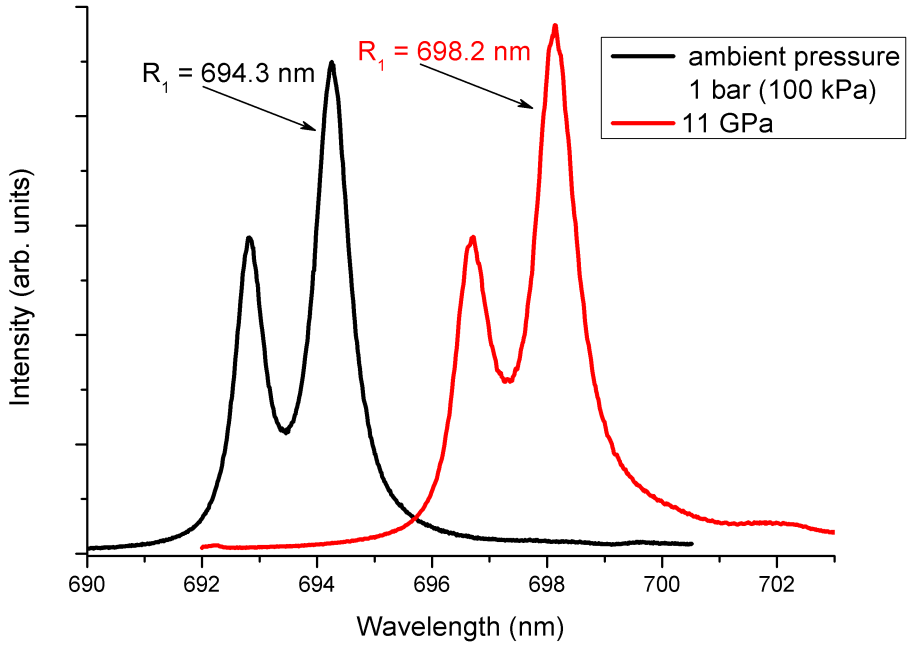

Figure 3.3: Chromium 3^+ luminescence in ruby at ambient pressure (black) and at 11 GPa (red).

be performed with great care so that the sample does not get lost. The small sample size limits the possibilities to use many kinds of (especially destructive) analyzing methods.

3.1.2 Pressure calibration

After filling and closing the cell, the pressure has to be adjusted to the desired value. Pressure can be applied simply by tightening the screws that regulate the distance of the two anvils. There are several possibilities to measure the pressure inside a DAC, having different advantages and disadvantages. The method of choice for a long time has been to use Si or elemental metals such as Pt, Au, Ag as internal pressure standard, relating the equation of state of the bulk moduli that are well-known for these materials to the measured lattice constant. The disadvantage of this method is that a strong x-ray (typically synchrotron) source is necessary yielding the pressure calibration very time-consuming. Also, the occurrence of additional calibrant lines in the diffraction pattern is disadvantageous for x-ray analysis of the sample [60]. As an alternative, the addition of a small ruby chip, as first suggested by Forman et al. [61], makes it possible to measure the pressure by fluorescence spectroscopy. The transparent diamond allows to focus of a laser onto the ruby chip and to collect the fluorescence signal. Ruby's main fluorescence lines (R-doublets) are very intense and are therefore easily detectable even through several mm of diamond. For the pressure calibration, the high intensity R_1-line is used which is at 694.3 nm at ambient pressure. With increasing pressure, the lines shift towards the red side of the visible spectrum (see Fig. 3.3). Only very small pieces of ruby need to be added because of the very strong fluorescence signal. Furthermore, because ruby is chemically inert, it can be present in the sample chamber without interfering with the experimental specimen [62]. The fluorescence line shift has been calibrated against

the compression of NaCl (measured by x-ray diffraction) to be able to relate the measured shift in wavelength to a certain pressure [63]. The shift of the fluorescence lines is almost linear up to 30 GPa [64] and has been investigated and further developed by several groups [65, 66, 67, 68, 69].
As mentioned before, the pressure inside a DAC can be calculated by measuring the wavelength shift of the fluorescence lines. Mao and Bell [65] calibrated this shift first up to 80 and later to 100 GPa [66] under quasi-hydrostatic conditions and developed the following simple formula with empirical A =1904 and B = 7.665:

$$P(GPa) = \frac{A}{B}\left[\left(\frac{\lambda}{\lambda_0}\right)^B - 1\right] \tag{3.1}$$

This calibration method is very common, because it is fast and easy. On the other hand, this method is often inapplicable at pressures higher than 100 - 150 GPa, due to weakening of the fluorescence signal and/or due to non-hydrostatic pressure effects. Therefore, some groups developed a technique which uses the Raman signal of the diamond tip, directly touching the sample chamber, as pressure indicator [60, 70]. The Raman peak of diamond also shifts to higher wavelength under high pressure and can be described by the following formula

$$P(GPa) = C\,\frac{\Delta\nu}{\nu_0}\left[1 + \frac{1}{2}(D-1)\frac{\Delta\nu}{\nu_0}\right] \tag{3.2}$$

with C = 547 and D = 3.75 and ν_0= 1333 cm^{-1}.

Unfortunately, at low pressures the error in the calibration is very large and therefore, despite its disadvantages, the ruby fluorescence method is the most common pressure calibration tool in combination with diamond anvil cells.

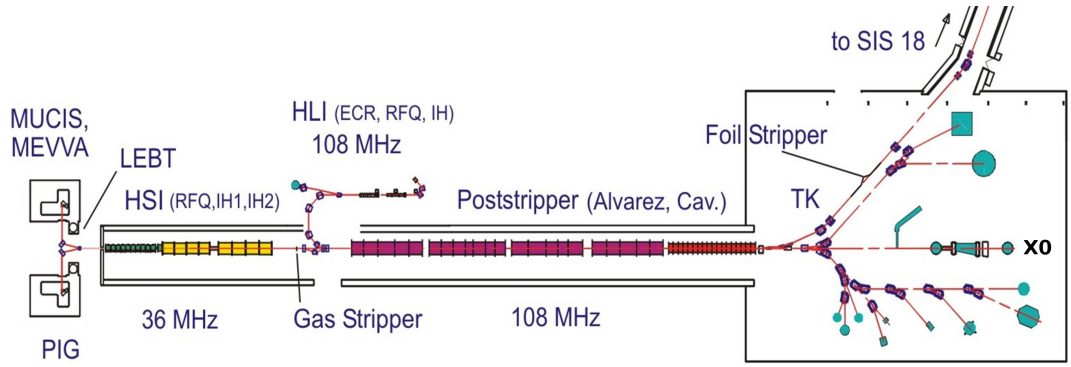

Figure 3.4: Schematic of the UNILAC at GSI. The ions come from the ion sources, are transferred into the high current injector where they are pre-accelerated and further accelerated in a four-tank Alvarez structure after increase of the charge state in the gas stripper. At the end of the 120 m long linear accelerator, the ion beam can be transferred into one of the four beam branches (M, X, Y, and Z) or the heavy ion synchrotron SIS - 18.

3.2 Irradiation conditions

All irradiations were performed at the radiation facility of the GSI Helmholtz Center for Heavy Ion Research. Two different sample irradiation processes have been used for this thesis. For low-pressure conditions, irradiations were performed at the Universal Linear Accelerator (UNILAC) while pressurized samples were irradiated at the heavy ion synchrotron (SIS) of GSI. Various methods were used for sample preparation and will be discussed in the following sections.

3.2.1 UNILAC irradiations

The 120 m long linear accelerator of GSI can accelerate all elements up to the heaviest naturally occurring element uranium with energies up to 11.4 MeV/u [71]. All samples referred to in this work as irradiated under ambient conditions were irradiated at station X0 (see Fig. 3.4) of the Materials Research Department. The samples were mounted onto a 5×5 cm^2 aluminum holder which was transported by a sample inlet system into the vacuum chamber for irradiation. All samples were irradiated at room temperature and perpendicular to the sample surface. By using quadrupole magnets, the ion beam was widened so that the 5×5 cm^2 sample area was homogeneously irradiated. Fluences (ions/cm^2) ranged from 10^{10} to several 10^{13} ions/cm^2. The ion flux (ions cm^{-2} s^{-1}) was kept between 1×10^8 and 5×10^8 ions cm^{-2} s^{-1} to exclude excessive macroscopic heating of the samples. The electric current of the ion beam is measured with a so-called Faraday cup. This signal can be converted into a beam current value for a given area and charge state of the ion beam. Because the Faraday cup is a beam stopping device, it can not be used during irradiation. To monitor the accumulated fluence on the sample a secondary-electron transmission monitor (SEETRAM) is used, consisting of three aluminum foils, each of 1 μm thickness. The two outer foils are biased with +100 V to sweep out the free electrons and the middle foil is connected to a current amplifier [72]. The SEETRAM emission current is calibrated against the Faraday cup and is left in front of the sample during the irradiation, leading to a small reduction in energy from 11.4 to 11.1 MeV/u.

3.2.2 SIS irradiations

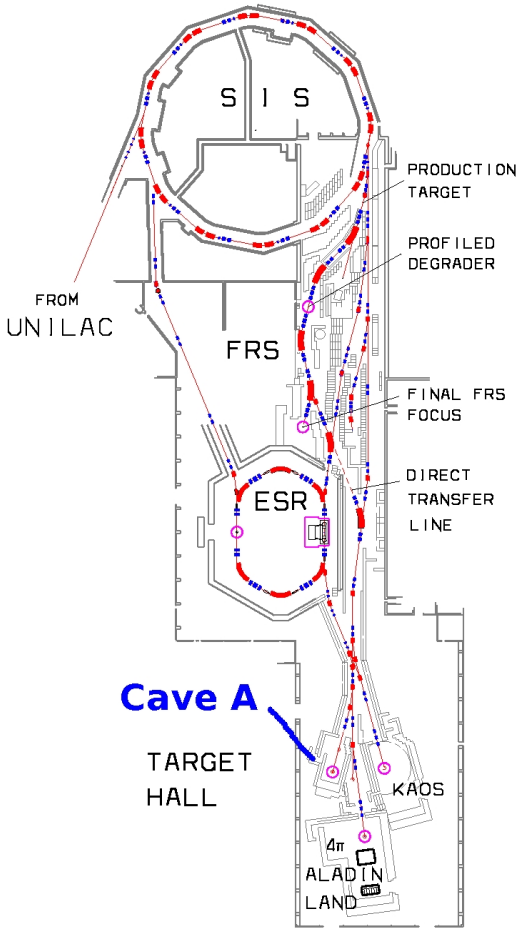

Figure 3.5: Schematic of the SIS 18 and connected experimental facilities. In this ring accelerator structure, there exist two RF acceleration cavities which allow the acceleration of ions up to 2 GeV/u (1 GeV/u for uranium ions). The ions can then be extracted and guided into several experimental sites in the high-energy experimental hall.

After acceleration in the UNILAC, the ion beam, with an energy of 11.4 MeV/u, can be injected into the heavy ion synchrotron SIS-18 (Fig. 3.5) where the ions can be further accelerated up to 90 % of the speed of light. The SIS with a circumference of 216 m can accelerate heavy ions from 50 MeV/u up to 2 GeV/u (1 GeV/u for uranium). By the use of multiturn injections, it is possible to accumulate several 10^9 of $^{238}U^{73+}$ ions in the SIS which can be accelerated and then delivered to different experimental sites [71].

All high-pressure irradiations were performed at the experimental site Cave A in the SIS target hall. To irradiate pressurized materials, ion energies of several hundred MeV/u are necessary to penetrate the first diamond and reach the sample inside the DAC.

3.2.3 High pressure irradiation procedure

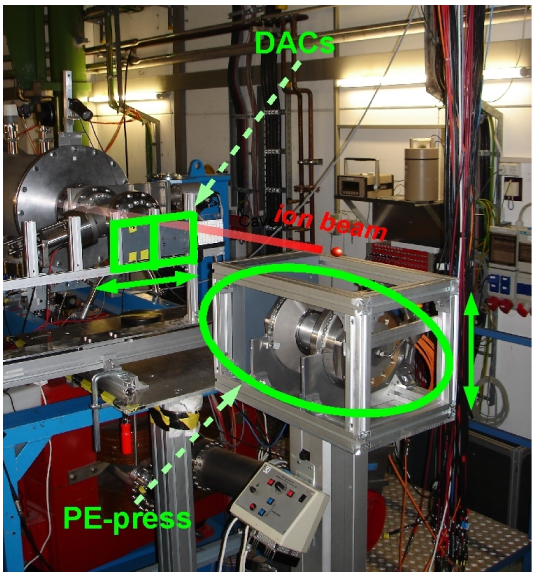

Figure 3.6: Photograph of the experimental setup at Cave A. The ions exit the beamline through a thin aluminum window (left) and are shot into the diamond anvil cells (holders marked by green squares). On the right, side on can see a Paris-Edinburgh press for larger samples.

Before irradiation, all high-pressure cells are placed inside a specialized plastic holder for mounting and centering. The holders are mounted on a motorized stage which can be moved from the measuring hut (see Fig. 3.6). Because the spot size of the ion beam is kept very small ($\sim$ 0.25 mm), centering of the sample is quite important. We therefore use a carefully adjusted cross laser system. By means of the last steering magnets in the beamline, the ion beam is positioned onto the laser cross on a fluorescence screen. The pressurized samples were irradiated with either Xe, Au, or U ions using a slow extraction mode of $\sim$ 1 second and extraction cycle of about 4 seconds. The dose was about 1-4$\times 10^8$ ions per extracted beam, leading to an irradiation durations of a few minutes up to several hours depending on the intended fluence of the sample.

Figure 3.7 shows a schematic of the irradiation setup at Cave A. The ion flux (and accumulated fluence) were monitored similarly to X0 with a SEETRAM detector consisting of three titanium foils, each 10 μm thick. The initial energies were calculated with the SRIM-2008 code [22] and fixed such that the ions had a remaining energy of 30 MeV/u when reaching the sample after passing the SEETRAM detector, the exit window, 45 cm of air, and the 1.5 - 2.5 mm thick diamond. The accuracy of the energy calculations have been experimentally confirmed by M. Lang et al. [73]. Initial energies thus ranged from 150 to 230 MeV/u depending on the ion species. Due to the advantageous property of heavy ions to deposit most of their energy at the end of their trajectory, the energy loss inside the sample is quite high.

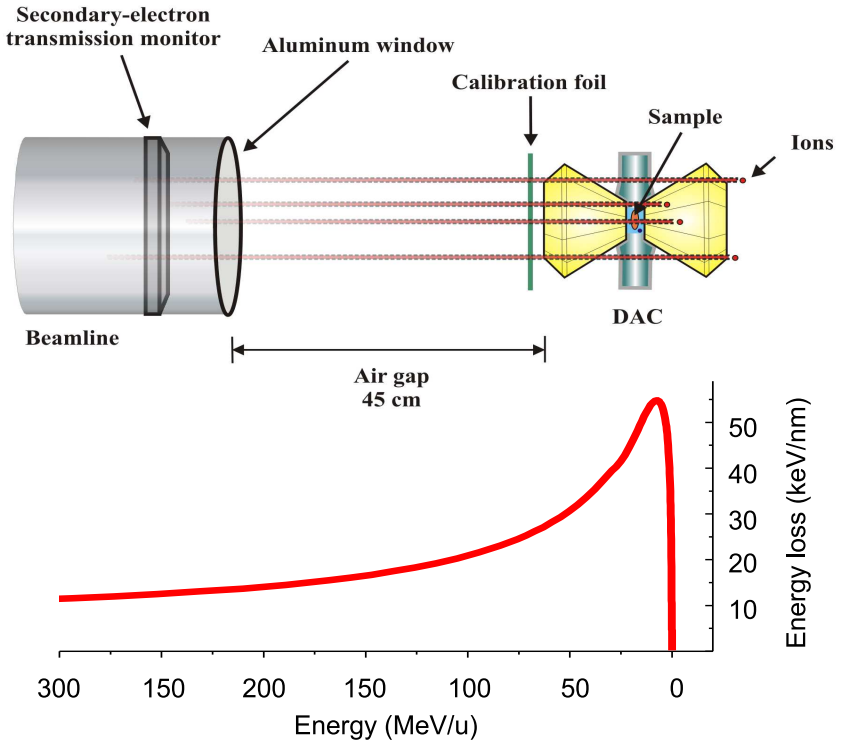

Figure 3.7: Schematic of irradiation procedure of pressurized samples. The initial ion energy is high enough to penetrate detector, exit window, air, and first diamond, cross the sample, and come to a stop in the second diamond. The underlying energy loss distribution shows that the energy loss occurring inside the sample, is near to the maximum of this distribution.

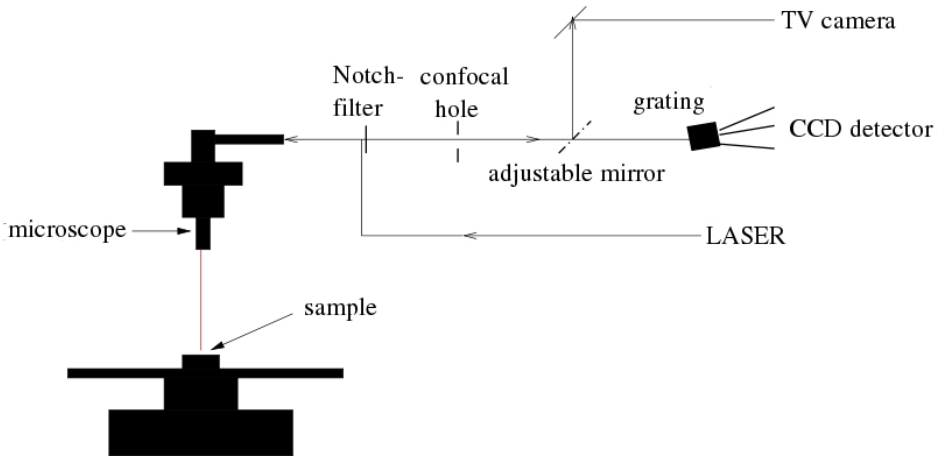

Figure 3.8: Schematic of a Raman spectrometer

3.3 Raman measurements

All Raman measurements (except the Raman data for ruby) were performed with a commercial Raman spectrometer from HORIBA Jobin Yvon™(HR800) with a 20 mW HeNe-laser having an excitation wavelength of 632.82 nm. The employed Raman system is a so-called 180° system where the backscattered light enters the spectrometer through the same optical path as the incoming beam (see Fig. 3.8). The great advantage of Raman spectroscopy is that it is possible to study very small amounts of sample material and to measure destruction-free. Because only one out of 10^6-10^8 photons from the backscattered light is "Raman-scattered", the strong Rayleigh scattered light has to be blocked. Otherwise the photo-sensitive detector will saturate and no Raman signal can be detected. To discriminate the Rayleigh scattered light, "Notch"-filters are used that filter out the light of a certain wavelength domain around the Rayleigh wavelength. In our Raman setup, an edge instead of a Notch filter is used. An edge filter not only filters a small spectral domain of 20-30 nm but discriminates all wavelengths shorter than a certain well-defined value. In this way, one loses the possibility to measure any Anti-Stokes signal, but the edge filter has a very small transition width below 1% of the laser wavelength, allowing measurements very close to the incident wavelength, gaining information at very low Raman shifts ($\leq$ 100 cm^{-1}). After passing the filter, the backscattered light is focused into the confocal hole whose width can be adjusted to discriminate signals from a certain depth of the sample. After that, the light passes through another slit and is focused on the monochromator with a grating of 1800 lines/mm, separating the Raman light into its spectral contributions before hitting the CCD detector. The CCD detector is a cooled (-70 °C), sectoral piece of silicon forwarding the signal of each sector to the computer [74].
The great advantage of this setup is that measurements can be performed without any complex preparations of the sample. Further, because of the integrated microscope even very small samples can be analyzed. The dimensions of the focal regions depend on the numerical aperture (NA) of the applied objective. The lateral diameter (D) of the laser spot is given by:

$$D \sim \frac{1.22\,\lambda}{NA} \tag{3.3}$$

The depth resolution (T) of the laser spot is given by [75]:

$$T \sim \frac{4\,\lambda}{(NA)^2} \tag{3.4}$$

The calculated values for our highest-NA objective ($\times$100, $NA = 0.9$) with which most analysis outside the pressure cells were performed, are 0.86 μm for lateral resolution D and 2.1 μm for the depth resolution T.

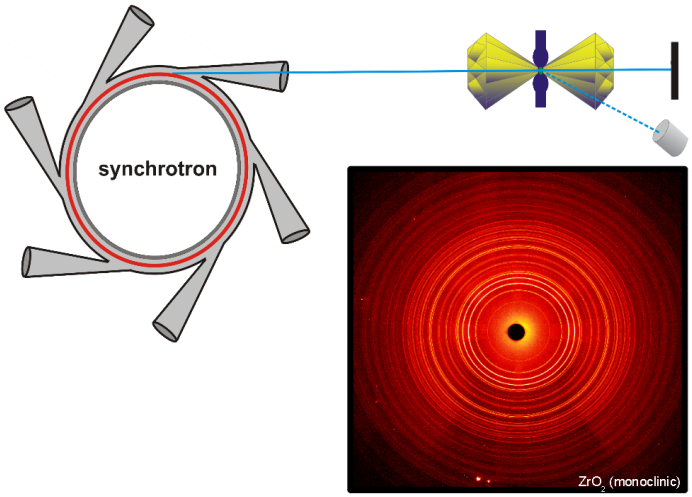

Figure 3.9: Schematic of synchrotron X-ray measurements on pressurized samples inside a pressure cell plus a typical diffraction image.

3.4 X-ray diffraction measurements

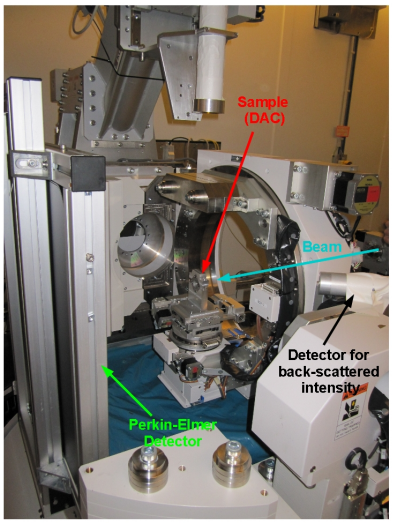

Figure 3.10: Experimental setup for X-ray diffraction measurements at the P08 beamline at DESY.

X-ray diffraction measurements of pristine and pressurized samples were performed at the P08 beamline of PETRA III at the German Electron Synchrotron (DESY) in Hamburg with a beam energy of (25.054 ± 0.005) keV (λ = 0.49467 Å) and a total flux at the sample of 10^{12} ph/sec, and an X-ray spot size of ∼ 50 μm in diameter. The energy selection was accomplished by using a double-crystal monochromator with Si single crystals. A compound of refractive beryllium lenses was used to collimate the beam [44]. Samples (usually inside a DAC) were mounted on a movable sled on a high-precision 6-circle diffractometer NZD-3 (Kohzu) (see Fig. 3.10). Additionally to the 6 rotations, 3 motors controlled the xyz position of the high-precision sample stage. The sample stage has a resolution of 0.2 μm in the movements of x, y, and z. The Debye-Scherrer rings were recorded with a Perkin-Elmer detector with a 16 bit digital resolution of 200 μm pixels and an image size of 2048×2048 pixels. A typical diffraction image is shown in Fig. 3.9. Depending on the opening angle of the DAC, diffraction patterns could be measured up to 30° of 2θ. The sample to detector distance was 390 mm. The diffraction image was integrated into two-dimensional patterns with the program Fit2D [76], and the configuration parameters of the experimental setup were calibrated with a cerium dioxide (CeO_2) standard. XRD patterns were refined by the Rietveld method using the MAUD [77] and GSAS [78] software.

4 Pre-experiments

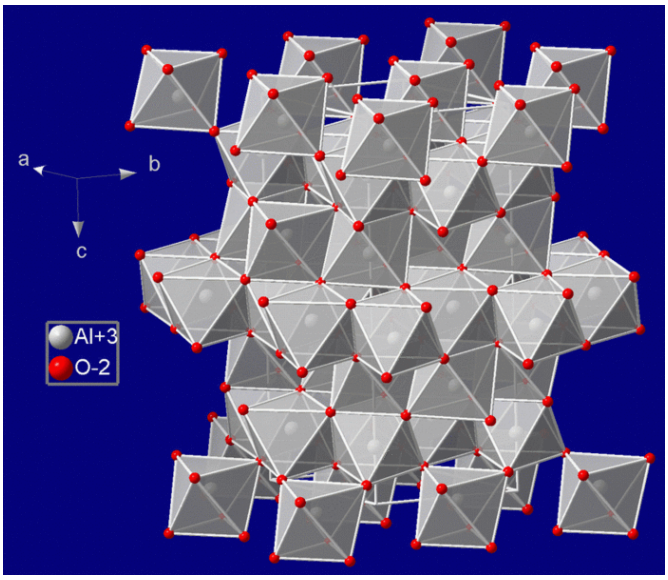

Figure 4.1: Crystal structure of corundum.

4.1 Ruby as pressure gauge

Ruby is the chromium containing variety of aluminum oxide (Al_2O_3), also called corundum. The crystal structure of Al_2O_3 can be described as trigonal or hexagonal. The structure is like a closed packed stacking of oxygen layers with Al ions occupying two thirds of the octahedral interstitial between the layers [79]. This means that one aluminum ion sits in the center of a slightly distorted octahedron formed by six oxygen ions. Only $\frac{2}{3}$ of the octahedrons are occupied by Al ions. For corundum to become ruby, the vacant Al positions are occupied by the Cr^{3+} ions causing the red coloring and fluorescence of ruby. The positions of the Cr ions are only slightly shifted to the positions of the Al ions due to the larger ionic radius [80]. The typical fluorescence of ruby (Al_2O_3:Cr^{3+}) has become the most prominent optical pressure sensor for high-pressure experiments in combination with diamond-anvil cell (DAC) techniques [61, 81, 66]. The ruby pressure calibration scale originally developed by Mao et al [66, 65] has been extended and refined by others [67, 82, 83] and is nowadays a well-established pressure gauge.
To apply ruby as pressure gauge in this study, it is mandatory to verify if irradiated crystals still provide reliable pressure calibration. Therefore, the fluorescence properties of ruby irradiated with swift heavy ions, both at ambient and high pressure conditions, were investigated.

In our case, we investigate the photoluminescence of ruby where energy is transferred to the outer electrons of the ruby by the photons of the incoming light. The outer d^3-electrons (which are bound to the Cr) can be excited to either the $^4T_1$ or $^4T_2$ level from which they decay quickly (in a few nano-

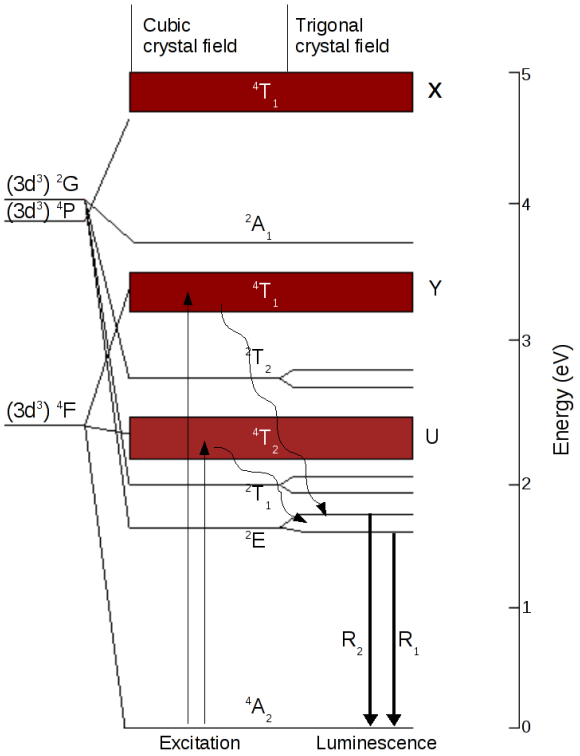

Figure 4.2: Schematic of the full energy level scheme of Cr^{3+} in ruby. The lowest energy free-ion multi-electron state of Cr^{3+} is a high-spin state (^4F). Absorption via U and Y bands in combination with phonon-assisted relaxation leads to the population of the excited ^2E state [79].

seconds) to a long-lived metastable ^2E state via phonon emission. From there, they decay (radiative lifetime 4 ms at 330 K [84]) back to the ground state $^4A_2$ causing the so-called R-line emission of 692.3 nm. The trigonal site distortion in combination with spin-orbit interaction results in an additional splitting of the ^2E level leading to the well-known R_1-R_2 splitting [85] (ΔR_{12} = 29 cm^{-1}) [79].

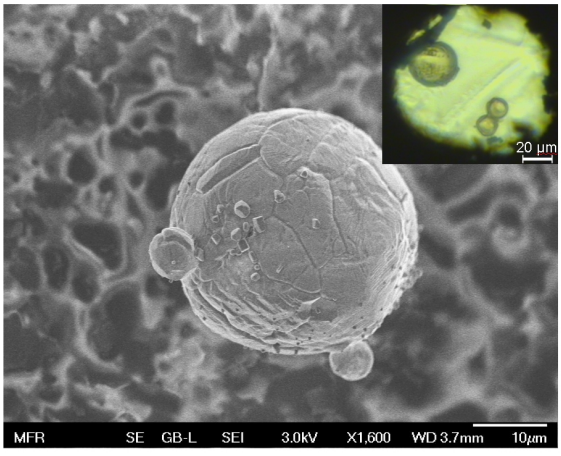

Figure 4.3: SEM image of a ruby sphere. The inset shows three ruby crystals mounted inside a DAC at 8 GPa.

The resulting fluorescence spectra therefore consist of two individual lines ($\lambda(R_1)$ = 694.28 nm and $\lambda(R_2)$ = 692.85 nm), with halfwidths of ~0.67 nm for R_1 and ~0.55 nm for R_2 at room temperature [79, 86].

Under pressure, the R-line fluorescence experiences a pronounced redshift. While the R_1-R_2 splitting remains almost constant under uniform hydrostatic pressures at room temperature, it is contrariwise highly sensitive to non-hydrostatic stress conditions [87, 88, 89]. In the past, the pressure-induced shift of the R_1 fluorescence band was carefully calibrated against various equations of state [66]. To date, the fluorescence signal of ruby is the most commonly used optical pressure gauge for DAC experiments up to the megabar pressure regime [90, 91].

In a DAC, the rubies used for pressure calibration, are placed next to the sample and are exposed to the same ion dose during sample irradiation. A pressure change inside the cell after irradiation can be a first indicator for possible changes in the material. Therefore, it was important to look at the radiation response of ruby with emphasis on its application as pressure gauge. Irradiation experiments were performed at ambient conditions at the UNILAC with standard ruby spheres, commonly used for pressure calibration, and additionly with oriented samples. Other experiments concentrated on the radiation response of ruby irradiated at high pressure, and on the pressure behavior of pre-irradiated samples.

4.1.1 Irradiations at ambient conditions

For exposure at ambient pressure, several small ruby spheres (∼10-30 μm in diameter, with ∼3600 ppm Cr^{3+}) [86] were packed in between 10-μm thick aluminum foils and irradiated at the Universal Linear Accelerator (UNILAC) of GSI with a pulsed beam (50 Hz) using different ions (^{132}Xe, ^{197}Au, and ^{238}U) of kinetic energy 11.1 MeV per nucleon (MeV/u). Fluences ranged from 1×10^{11} up to 1.8×10^{13} cm^{-2} for Au ions and 1×10^{13} cm^{-2} for Xe and U ions. According to the SRIM code [22], the ions have a range of about 60 μm in ruby, thus completely penetrating the samples. The stopping process of the ions is dominated by electronic excitation, i.e., so-called nuclear energy loss via elastic collisions of projectiles with atomic cores of the sample can be neglected. The average electronic energy loss $(dE/dx)_e$ in the sample is (25 ± 1.5) keV/nm for Xe, (37 ± 1.9) keV/nm for Au, and (48 ± 2.3) keV/nm for U ions.

All irradiated rubies were analyzed by measuring the position and FWHM of the laser-excited fluorescence R_1-R_2 doublet, using a cooled CCD detector of a commercial Raman spectrometer (Horiba Jobin Yvon HR800) with a spectral resolution of about 0.01 nm. The excitation was performed with light of a red He-Ne laser line at λ = 632.8 nm. To reveal structural changes, rubies exposed to Au ions were additionally investigated by Raman spectroscopy using a blue excitation wavelength of 488 nm also with Raman spectrometer by Horiba at the department of Edelsteinforschung of the University of Mainz. All measurements were performed at room temperature.

Because of the very strong fluorescence of ruby in the visible red region, the Raman spectra were measured with a blue excitation wavelength of 488 nm. Still, a strong background due to the fluorescence was overlaying the Raman signal. All Raman spectra shown are therefore background subtracted. The Raman spectra shown in Fig. 4.4 give clear evidence of ion-beam induced structural changes above a fluence of 10^{12} ions/cm^2 where track overlapping sets in. Ruby has two A_{1g} and five E_g vibration modes that are Raman active [92]. The intensities of the bands vary strongly for different polarizations [93]. Fig 4.4 shows the Raman spectra for unoriented rubies with randomly polarized excitation light, therefore showing all 7 bands. A_{1g} bands are at 418 and 645 cm^{-1}, E_g bands are at 378, 432, 451, 578, and 751 cm^{-1} [93]. With increasing fluence, the most prominent Raman bands at 417 and 379 cm^{-1}

Table 4.1: Electronic energy loss of various ions in ruby calculated by SRIM 2008 [22].

Ion	**electr. energy loss**
Ni	11 keV/nm
Xe	25 keV/nm
Au	37 keV/nm
U	48 keV/nm

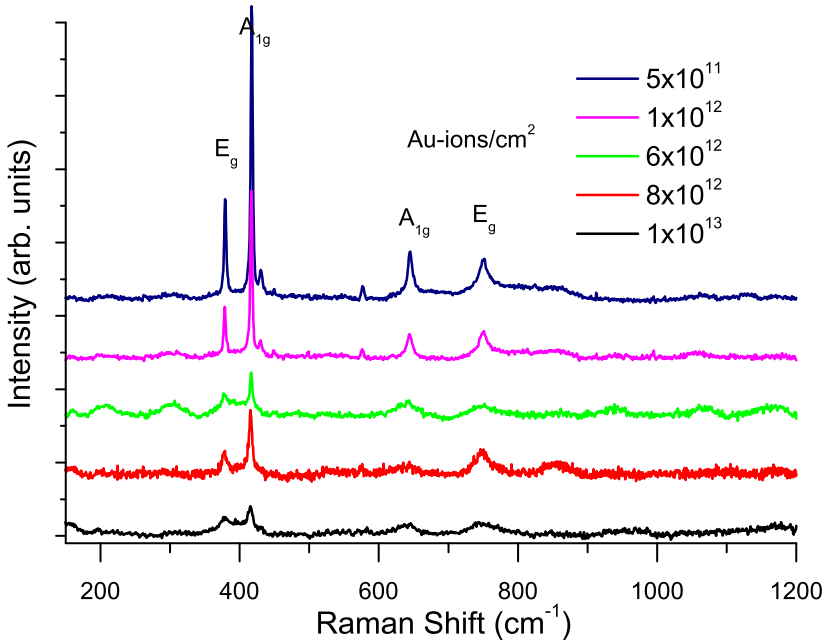

Figure 4.4: Raman spectra of unoriented rubies irradiated with 11.1 MeV/u gold ions. The bands broaden and strongly decrease in intensity indicating loss of crystalline structure.

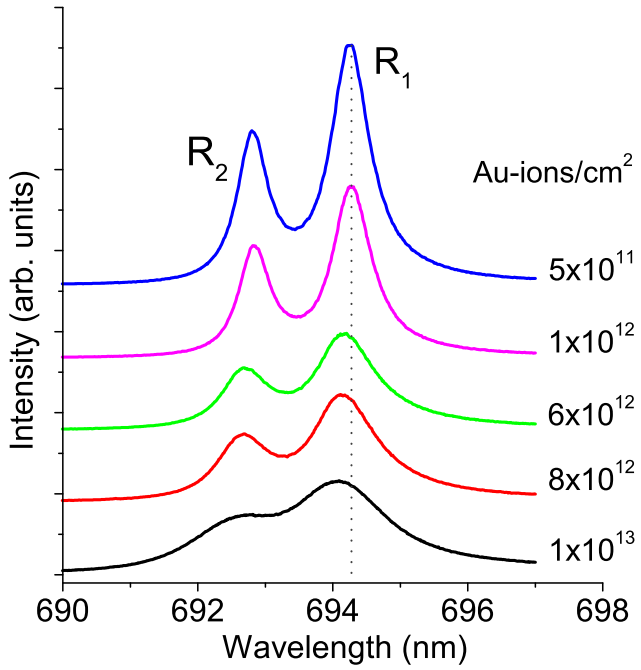

Figure 4.5: Ruby luminescence double-line spectra (R_1 and R_2) after irradiation with various fluences of 11.1 MeV/u gold ions. The spectra are stacked for better visibility.

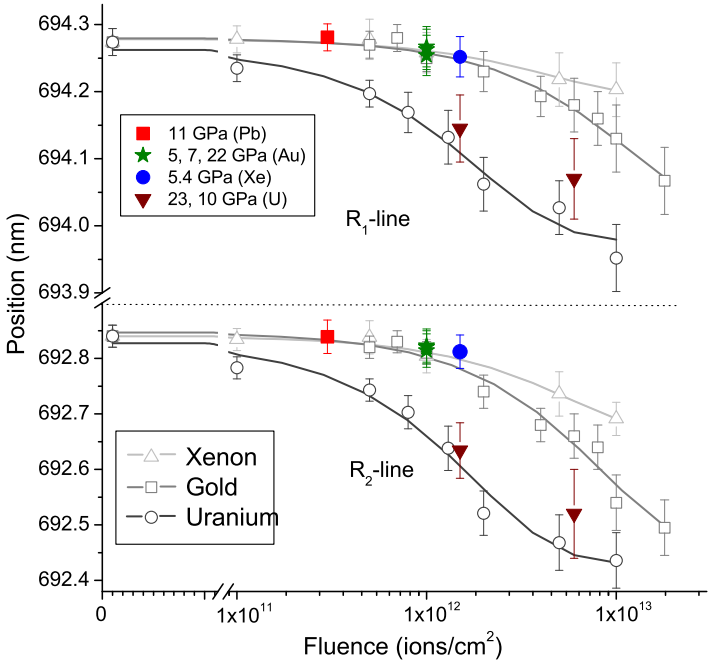

Figure 4.6: Position of the R_1 and R_2 lines versus fluence for Xe, Au, and U ions. Open symbols represent ambient irradiations of unoriented rubies. Colored (full) symbols show unoriented rubies irradiated at selected high pressures. The lines are exponential fits to the data.

broaden (swallowing the adjacent bands) and decrease in intensity. This trend is a typical indication for the softening of the lattice structure and beginning amorphization [94].

The evolution of the luminescence spectra of unoriented ruby crystals exposed to 11.1 MeV/u Au ions (Fig. 4.5) is similar. With increasing fluence, the line doublet decreases in intensity, broadens, and shifts to lower wavelengths. The induced change of the peak position (Fig. 4.6) and FWHM (Fig. 4.7) was evaluated for the different ion irradiations. Each data point represents the mean value of several measurements. For a given fluence, 5-10 rubies were evaluated, testing several areas of each crystal. The shift as well as broadening of the R_1-R_2 line evolve in the same manner, being most pronounced for U ions and scaling with the energy loss of the different ions (U > Au > Xe). The splitting of the two lines increases slightly with fluence, which is probably due to a non-hydrostatic stress situation inside the sample induced by the ion beam [95]. A shift of the luminescence lines of ruby crystals irradiated with ions of similar mass and energy has been reported earlier by Skuratov et al. [96, 97, 98]. However, the shift was towards lower energies, in contrast to our finding. The origin of this discrepancy is not quite clear but we assume that the specific sample and irradiation geometry, e.g. the use of oriented, thick samples and different irradiation conditions, has a strong influence on the resulting stress configurations. In the experiments described here, the ions are completely penetrating the small ruby spheres. This is the same situation when ruby crystals are inserted as pressure gauges in DACs. Complete irradiation allows beam-induced structural changes to relax by volume expansion, leading to a decrease in internal pressure. In contrast, thick crystals (range $\ll$ sample thickness) from Skuratov et al. are exposed only partially, so that compressive stress is built up, in particular at the interface of irradiated

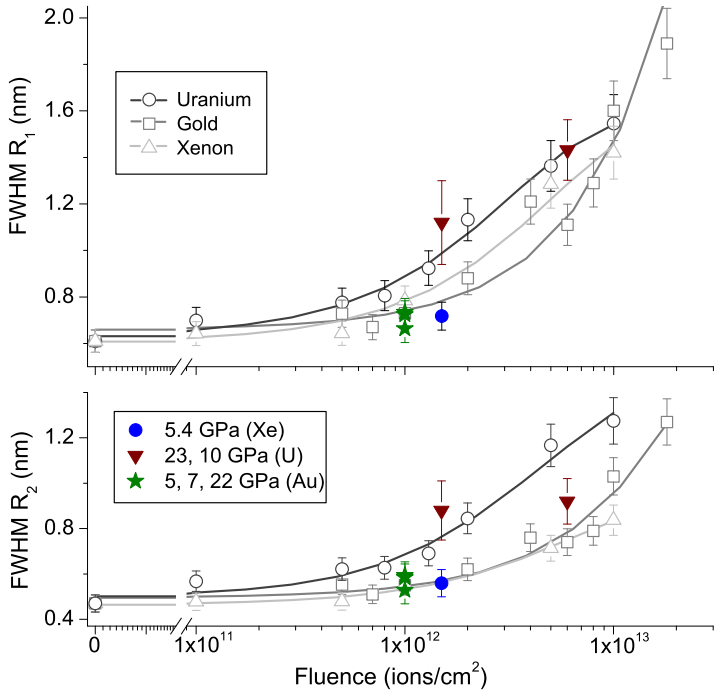

Figure 4.7: FWHM of the R_1 and R_2 lines versus fluence for Xe, Au and U ions. Open symbols represent irradiations of unoriented rubies at ambient conditions. Full (colored) symbols correspond to samples irradiated at high pressure. The lines are exponential fits to the data.

and unirradiated material, and the crystal thus experiences different stress components. While internal stress resulting from radiation damage is known from different investigations [99, 100, 101], geometrical effects on the resulting stress field have to be clarified by dedicated future experiments.

Pressure gauge applications of ruby crystals commonly use the position of the R_1 line for calibration. From our irradiation with 1×10^{13} U/cm^2, the maximum radiation induced effect shifts the R_1 line from (694.29 ± 0.02) to (693.95 ± 0.05) nm. This shift by 0.34 nm corresponds to a deviation of almost 1 GPa (10 kbar) from its actual pressure value using the parameterized relationship given by Mao et al. [66]. In the hydrostatic regime (for which these results are most interesting), this uncertainty can range from 10 % at 10 GPa up to almost 50 % at 2 GPa. To compensate for this radiation effect, and the resulting underestimation of the pressure, we propose to adjust the calibration formula by adding the term ε [102]:

$$P(GPa) = \frac{A}{B} \cdot \left[\left(\frac{\lambda_0 + \Delta\lambda + \overbrace{D_\infty \left(1 - e^{-\sigma\Phi}\right)}^{\varepsilon}}{\lambda_0} \right)^B - 1 \right] \tag{4.1}$$

with $A = 1904$ and $B = 7.665$ [66]. The correction term $\varepsilon = D_\infty \left(1 - e^{-\sigma\Phi}\right)$ [nm] accounts for the radiation damage, assuming a single-impact process [103, 104], i.e. each ion impact produces a cylindrical track with a damage cross section σ. The ion fluence is given by Φ. The contribution due to damaged material increases linearly in the low-fluence regime and saturates due to track overlapping at higher fluences. D_∞ is the saturation value of the R_1 line shift. For uranium ions the values are $D_\infty(R_1) = 0.34$

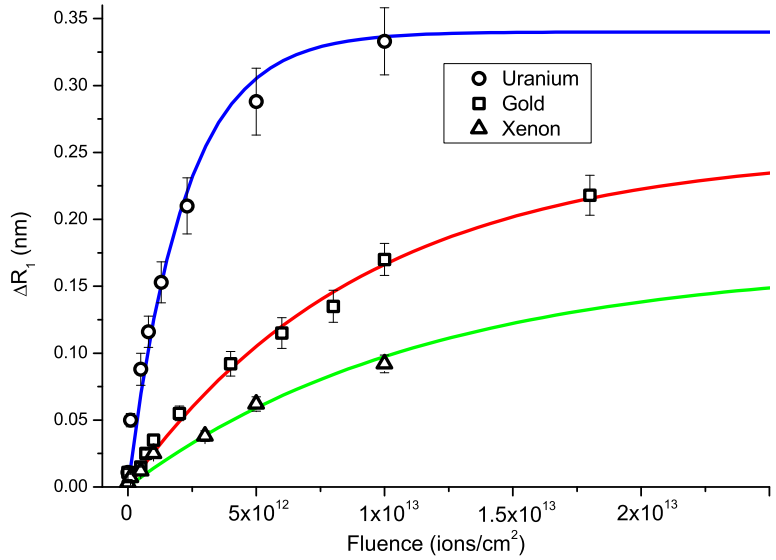

Figure 4.8: Relative shift of the R_1 line vs. fluence and ϵ fits according to Eq. 4.1 for Xe, Au, and U ions.

± 0.02 nm. For both lines, the saturation values for the different ions show the following correlation with the electronic energy loss:

$$D_\infty = D_\infty(max) \times \frac{\frac{dE}{dx}}{\frac{dE}{dx}_{max}} \tag{4.2}$$

where the index *max* applies to the maximum saturation and energy loss value from the uranium irradiation with $\frac{dE}{dx}(U) = 48\ \frac{keV}{nm}$. Fitting the equation for ϵ to the line shift data yields $D_\infty(R_1)$ of 0.25 ± 0.02 nm and 0.168 ± 0.02 nm for Au and Xe ions, respectively. The direct relation between the energy loss and D_∞ makes it possible to predict the pressure correction term for any other ion beam. Fitting ϵ to the line-shift data also allows us to deduce the damage cross section (see Fig. 4.8), yielding a σ of (5.30 ± 0.89) $\times 10^{-13}$ cm^2, (1.28 ± 0.23) $\times 10^{-13}$ cm^2, and (1.0 ± 0.2) $\times 10^{-13}$ cm^2 for U, Au, and Xe ions, respectively. These values correspond to a track radius of about 4.0 ± 0.5 nm (U), 1.9 nm ± 0.4 nm (Au), and 1.6 nm ± 0.4 nm (Xe).

4.1.2 Ruby irradiation under pressure

Because the behavior of materials simultaneously exposed to high pressure and heavy-ion irradiation can deviate strongly from that occurring under irradiation at ambient pressure [105, 106, 8], Figs. 4.6 and 4.7 include also experimental data from rubies irradiated at high-pressure conditions in a diamond anvil cell (see Fig. 3.7). Pressures ranged from 5 to 23 GPa for four different ions (full symbols). The additional pressure exerted on the ruby during irradiation seems to influence the R-line positions only marginally compared with the shifts caused by radiation damage. Data from the irradiation series with gold ions at a fixed fluence of 1×10^{12} ions/cm^2 and different pressures (5, 7, and 22 GPa) are shown as green stars in Figs. 4.6 and 4.7. The R_1 shifts for all three pressures coincide. Also the other high-

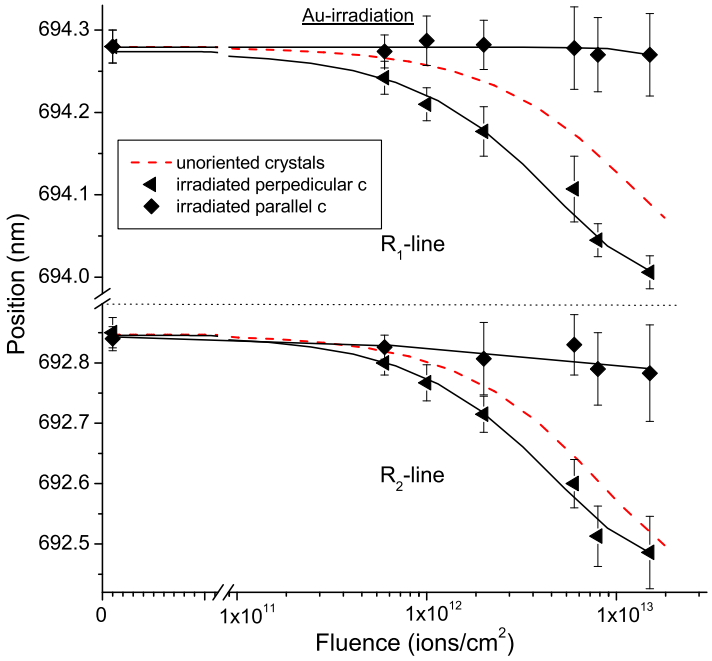

Figure 4.9: Postions of the R_1 and R_2 fluorescence lines as a function of applied fluence (11.1 MeV/u Au ions). ⧫ represents samples with surface irradiated parallel and ◄ samples with surface irradiated perpendicular to the c-axis. The red dashed lines show the fits for unoriented samples irradiated under the same conditions.

pressure irradiation data (Xe at 1.5 (5.4 GPa) $\times$ 10^{12} ions/cm^2 and U at at 1.5 (23 GPa) and 6 (10 GPa) $\times 10^{12}$ ions/cm^2) conform to the results of ambient irradiations. We thus conclude that the simultaneous exposure to pressure during irradiation has no significant additional effect, neither on the shift nor on the broadening of the fluorescence lines.

4.1.3 Irradiation of oriented ruby crystals

Irradiation experiments were also performed on two polished ruby plates of crystallographic (0001) and (11$\bar{2}$0) orientation. The irradiation was performed perpendicular (◄) and parallel (⧫) to the c-axis, applying the same beam conditions (11.1 MeV/u Au ions) as for unoriented rubies. The data of both oriented samples are shown in Figures 4.9 and 4.10. In contrast to the randomly oriented ruby spheres (visualized by the dashed red line), the rubies irradiated parallel to the c-axis (⧫) show almost no response to irradiation, whereas the effect for the ruby irradiated perpendicular to the c-axis (◄) is even stronger than for unoriented crystals for both luminescence lines. This behavior is visible for both lines but more pronounced for the R_1 line.
Obviously, the line shift as well as FWHM depend strongly on the crystal orientation. The increase of the R_1-R_2 splitting observed for unoriented rubies (Fig. 4.5) is probably an indication of the same effect given by the anisotropic response of the ruby crystal orientation with respect to the incidence of the ion beam. The minor response of the sample irradiated parallel to the c-axis is not unexpected taking into

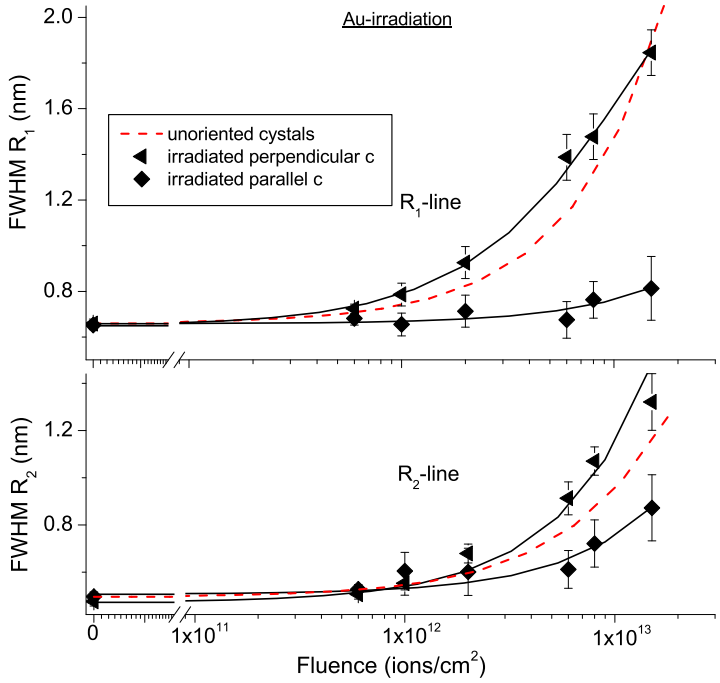

Figure 4.10: FWHM of the R_1 and R_2 fluorescence lines as a function of fluence (11.1 MeV/u Au ions). ♦ represent samples irradiated parallel and ◄ irradiated perpendicular to the *c*-axis. The dashed red lines show the fits for unoriented samples irradiated under the same conditions. The solid black lines are exponential fits to the data.

account the lattice structure of ruby. Since the lattice constant $c = 12.99$ Å is almost three times as large as the other constant $a = 4.76$ Å) [79], the structural damage along the c axis is less pronounced.

4.1.4 High pressure behavior of irradiated rubies

For a quantitative validation of irradiated rubies as pressure gauge, the position of the R_1 line was monitored as a function of pressure. For comparison, pre-irradiated (Au ions, 11.1 MeV/u) and pristine rubies were placed inside the sample chamber of a symmetric DAC. A mixture of 16:3:1 methanol-ethanol-H_2O, used as pressure medium, ensured hydrostatic conditions inside the cell up to ∼10.5 GPa [58]. The pressure was increased in multiple steps up to 10 GPa and was monitored by the pristine ruby crystals. Because of the optical transparency of diamond, the fluorescence spectra can easily be measured through the anvil of the DAC. Figure 4.11 displays the differences of the R_1-line positions of pre-irradiated and pristine (R_1^0) ruby as a function of pressure for various fluences and crystal orientations. Up to a fluence of 7×10^{11} Au/cm^2, the R_1-R_1^0 difference is negligible and therefore not plotted. For higher fluences, R_1-R_1^0 becomes significant but remains independent of the applied pressures up to fluences of 6×10^{12} Au/cm^2 (stars), and independent of the crystal orientation and the previously reported anisotropy (♦, ◄). Remarkably, for 1.0 and 1.8×10^{13} ions/cm^2, the influence of pressure becomes significant. At ambient pressure, the (R_1-R_1^0) wavelength difference is -0.21 nm. With increasing pressure, (R_1-R_1^0) approaches zero, changes its sign at ∼ 5 GPa and reaches 0.2 nm at ∼ 9 GPa. We ascribe this

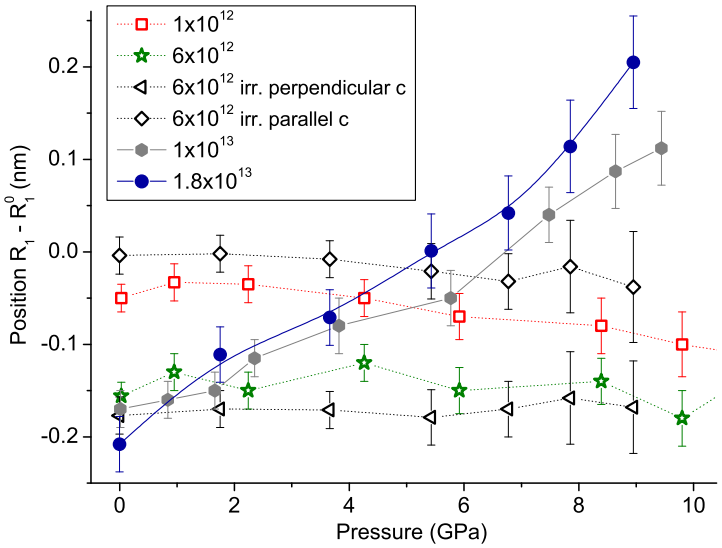

Figure 4.11: Shift of the R_1-line position of irradiated rubies with Au ions compared with that of pristine crystals (R_1^0) as a function of pressures. Black, open symbols represent oriented ruby crystals. The lines are guides to the eye.

effect to severe structural damage. At such high fluences, completely disordered layers appear and the crystals are partially amorphized [100].

4.1.5 Summary

In summary, the results show that heavy-ion irradiation of ruby causes a shift to lower wavelengths as well as a broadening and slight splitting of the two luminescence lines. Samples irradiated perpendicular to the c-axis display a stronger radiation response than those exposed to the beam at random crystal orientation. The effect is negligible for irradiations parallel to the c-axis. Quantitatively, the line shift depends strongly on the electronic energy loss of the ion, being more pronounced for U than for Au and Xe ions. Pressure additionally applied during irradiation does neither enhance nor lessen the effect but follows the same trend. For fluences up to 1×10^{12} ions/cm^2 (for Xe, Au) and 1×10^{11} (for U), the shift is negligible.
Radiation effects induced in ruby should be considered above 1×10^{12} ions/cm^2. For a fluence of 1×10^{13} U-ions/cm^2 the pressure underestimate is ≥ 1 GPa. The deviation can be taken into account by inserting a correction term $(D_\infty\left(1-e^{-\sigma\Phi}\right))$ in the standard calibration formula. Our results on ion-irradiated ruby crystals demonstrate that the luminescence lines of Cr dopants are suitable probes for providing in-situ damage and stress accumulation. This approach may open new perspectives to monitor damage and stress development and thus provide important information on material changes exposed to high energy ion bombardment.

5 Results and Discussion

5.1 Zirconia (ZrO_2)

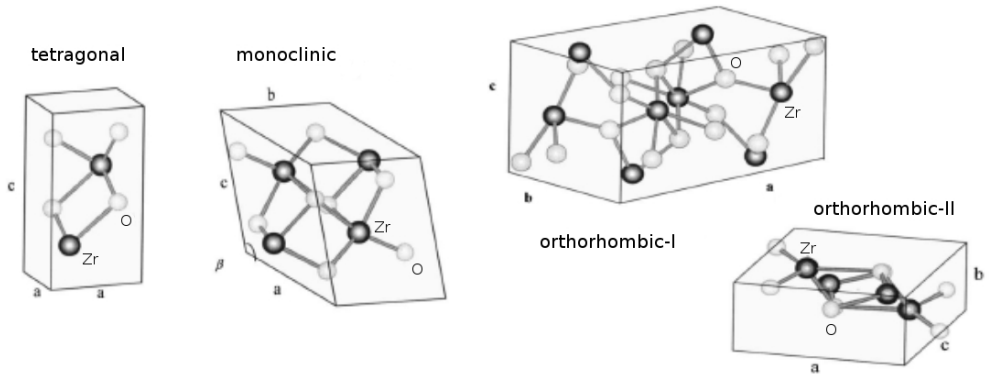

Figure 5.1: Unit cells for four different structures of ZrO_2, monoclinic, tetragonal, orthorhombic I, and orthorhombic II (cotunnite). The picture is taken from [107].

Zirconia or zirconium dioxide (ZrO_2), first investigated by the German chemist Martin H. Klaproth in 1789, has become one of the most commonly used ceramics [108]. Zirconia has five known structural formations depending on pressure and temperature of the material. The structural configurations of four different crystalline phases of ZrO_2 can be seen in Fig. 5.1.

5.1.1 Phase transitions in ZrO_2

At ambient pressure and temperature conditions, zirconia exits as a white powder in its monoclinic (also called baddelyte) phase. At temperatures around 1170 °C, zirconia transforms into its tetragonal high-temperature form accompanied by a density increase of ∼ 4 % [109]. At 2370 °C, a transformation into the cubic structure occurs before it melts at around 2750 °C [110, 10].

Zirconia also exhibits two high-pressure phases, but although numerous groups (e.g. [111, 112, 113, 114, 115, 116]) performed high-pressure experiments on this material, the exact boundaries are not certain, which probably arises from the fact that high pressure transitions often occur quite sluggishly and are not easily detected.

5.1.1.1 monoclinic → orthorhombic I transition

At pressures between 4 and 7 GPa, a transition from monoclinic to the first high-pressure phase orthorhombic I (space group Pbca) with a polyhedral coordination of seven takes place [117, 112]. This

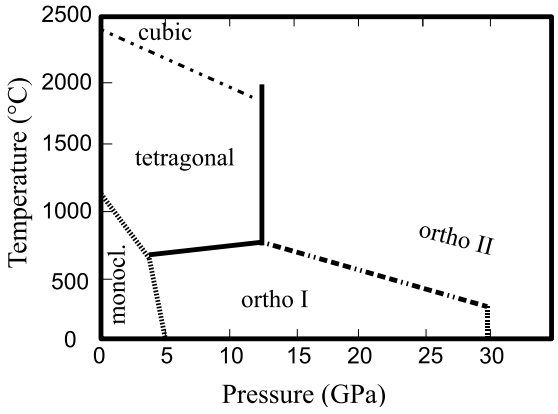

Figure 5.2: Phase diagram of ZrO_2 taken from Ohtaka et al [117].

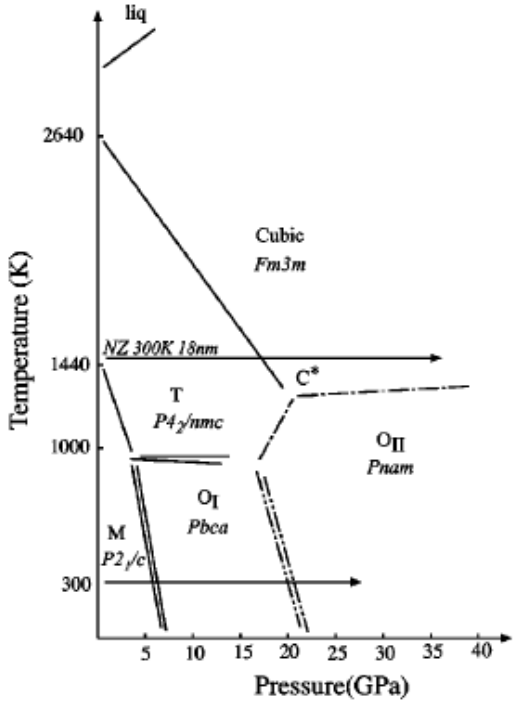

Figure 5.3: Phase diagram of ZrO_2 taken from Bouvier et al [118].

displacive transition is very sluggish at room temperature and depends on the crystallite size. Even at pressures around 10 GPa and room temperature, remains of the monoclinic phase are still detectable. The orthorhombic I phase is not quenchable to ambient conditions.

5.1.1.2 orthorhombic I → orthorhombic II transition

At elevated temperatures > 600 °C, the transition into the second high-pressure phase orthorhombic II (space group Pnma) polyhedral coordination of nine [114] takes place at 12.5 GPa [117, 119, 111] and is quite temperature independent. One has to point out that at temperatures > 600 °C the transition starts from the high-temperature tetragonal phase and is therefore not really an o I → o II transition. At room temperature, depending on the literature source, the transition occurs between 22 GPa [120, 118], 25 GPa [121], 28 GPa [113], 30 GPa [119, 114], and 35 GPa [112]. Because the ortho-I → ortho-II transition is of a reconstructive type [122], it is not surprising that it becomes increasingly sluggish at ambient temperature and usually an excess pressure of 10 GPa is needed for a full transformation [117]. This additional energy investment results in the fact that the orthorhombic II phase, once produced, is quenchable to ambient pressures [117, 119, 122]. The ortho-I → ortho-II transformation requires a significant reorganization of the cation and anion sublattices, increasing the coordination number of Zr^{4+} from seven to nine and therefore being kineticly slow to the point of being frozen at room temperature [114]. But also thermodynamic effects may play a role as *ab initio* calculations indicate that the orthorhombic II structure lies at a lower energy level than the monoclinic phase [123, 124]. Experimental and theoretical studies revealed that the ortho-II structure has a very large bulk modulus

crystal structure	lattice group	lattice parameter [Å]	density [g/cm^3]
monoclinic $a \neq b \neq c$ $\alpha = \gamma = 90°$ $\beta > 90°$	$P2_1/c$	$a = 5.296$ $b = 5.094$ $c = 5.326$ $\beta = 99.3°$	5.7
tetragonal $a = b \neq c$ $\alpha = \beta = \gamma = 90°$	$P4_1/nmc$	$a = 3.608$ $c = 5.187$	6.1
cubic $a = b = c$ $\alpha = \beta = \gamma = 90°$	$F_{m\bar{3}m}$	$c = 5.128$	6.3
orthorhombic I $a \neq b \neq c$ $\alpha = \beta = \gamma = 90°$	Pbca	$a = 10.1745$ $b = 5.3148$ $c = 5.1357$	6.8
orthorhombic II $a \neq b \neq c$ $\alpha = \beta = \gamma = 90°$	Pnma	$a = 5.6140$ $b = 3.3474$ $c = 6.5658$	-

Table 5.1: Structural data of all five solid-state phases of ZrO_2 [127, 120, 107, 124, 117, 128, 110].

between 300 and 400 GPa [121, 120, 13] making it a good candidate for a new superhard material [13, 117, 125, 126]. The structural phase behavior of ZrO_2 is displayed in two pressure-temperature phase digrams in Figures 5.2 and 5.3. The characteristics of all known solid-state phases are listed in Table 5.1.

5.1.2 Stabilized zirconia and its applications

Besides the structural variety which makes zirconia interesting for structural investigation, ceramics made out of ZrO_2 are one of the most important functional materials of this time [129]. Some of the main properties which make ZrO_2 so interesting are e.g. the high fracture toughness, the low thermal expansion, high refractoriness, high resistance to wear and corrosion, and many more [130]. The applications of zirconia ceramics are therefore numerous. Due to its high bending and tensile strength, it is used e.g. as cladding material for plane turbines and as cutting material in knife-blades [129, 131]. Even the medical sector discovered the great advantages of zirconia ceramics and uses them as bio-ceramic implants, e.g. for hip and hip-joint prostheses [132, 133]. Beside the high strength and low brittleness, the fact that zirconia is chemically inert plays an import role. Also most tooth implants consist of zirconia ceramics due to the white color imitating the color of natural teeth. Next to all these industrial applications, there is one especially important possible application. Because of the low response towards radiation, zirconia ceramics are used, e.g., as inert fuel matrix in nuclear reactors [12, 134, 135, 136], and as containment material for radioactive waste [10, 134], as cladding material e.g. in combustion chambers, and nuclear fuel assemblies in pressurized water reactors [137].

The fact that the high-temperature phases (tetragonal and cubic) have a higher density than the ambient temperature phase (monoclinic) restricts the use of monoclinic zirconia for high-temperature applications. Upon cooling from the tetragonal to the monoclinic phase, which occurs at $\sim$ 950 °C, the

volume expansion of $\sim 4\,\%$ [109] accompanied by a shear strain of ~ 0.16 [138] causes ZrO_2 to crack. Therefore, ZrO_2 is often stabilized in its high-temperature forms by adding soluble oxides such as Y_2O_3 (mostly used), MgO, CaO, and Ce_2O_3, which suppress the transformation into its monoclinic structure. Yttrium oxide not only serves as a stabilizer but creates oxygen vacancies for every unit of the Y_2O_3 dopant causing a high oxygen ion conductivity [139]. The oxygen vacancies displace any oxygen ion from the equilibrium position in the tetragonal phase, so that the tetragonal $\rightarrow$ monoclinic transformation is suppressed [140]. Depending on the amount of dopant, either the tetragonal or the cubic phase is stabilized. At ~ 3 mol %, the tetragonal phase is stabilized, being called partially stabilized zirconia (PSZ). For dopant concentration higher than 8 mol % the cubic structure is predominant, which is called fully stabilized zirconia (FSZ). The oxygen ion conductivity reaches its maximum at concentrations around 9 mol % and decreases rapidly with increasing Y_2O_3 concentration [141]. This is because at concentrations below 10 mol % the oxygen vacancies are preferentially located at zirconium ions, whereas at higher concentrations they start to form around the yttrium ions [142]. In the 1970s and 1980s, it was discovered that the transformation from the tetragonal to monoclinic phase may be enhanced by controlling the structural properties such as strength and fracture toughness of the material [138]. The t $\rightarrow$ m transition is associated with volume expansion, but due to the strength of the stabilized tetragonal or cubic zirconia it is prevented to do so. If stress is applied to stabilized zirconia it might create a crack tip that causes the transformation into the monoclinic phase accompanied by volume increase. This volume increase then compresses the crack, retarding its growth, and enhances the fracture toughness of ZrO_2 [143]. This mechanism is called transformation toughening. Such transformation-toughened ceramics are often referred to as ceramic steel for the strain and stress response is similar to that of steel [144]. To date, ZrO_2-based ceramic alloys have been demonstrated to be the strongest and toughest (single-phase) oxide ceramics yet produced [138].

5.1.3 Irradiations at ambient pressure

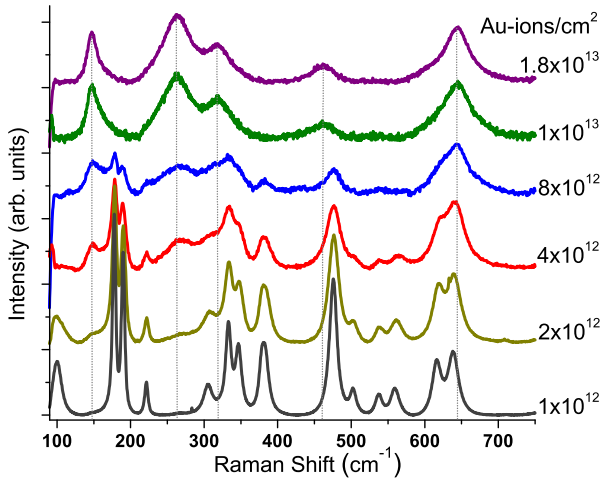

Figure 5.4: Raman spectra of ZrO_2 irradiated at ambient pressure with 11.1 MeV/u Au-ions for various fluences.

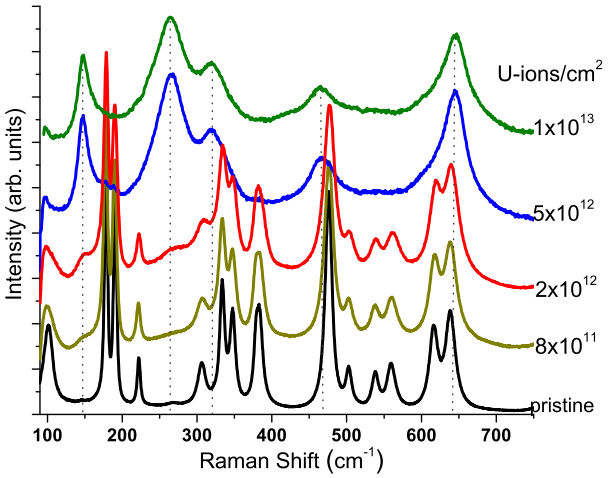

Figure 5.5: Raman spectra of ZrO_2 irradiated at ambient pressure with 11.1 MeV/u U-ions for various fluences.

At ambient pressure, the radiation response of zirconia has been extensively studied for low-energy ions at room [145, 146, 147, 137] and cryogenic [136] temperatures as well as for swift heavy ions [3, 148, 149, 150, 151, 152, 153]. All cited experiments showed that for very high ion fluences a structural phase transition from the monoclinic to the high-temperature tetragonal phase occurs. For experiments performed with low-energy ions in the nuclear stopping regime (e.g. Ge, Kr, or Xe-ions of energy around 300 keV), the transformation occurs only in a surface layer of few hundred nm [137] and requires fluences around 10^{18}-10^{19} ions/cm^2 [145]. For swift heavy ions with electronic stopping (Ni, Ge, Kr, I, and Xe of energies up to about 10 MeV/u), the monoclinic → tetragonal transition requires a critical energy loss of 13 keV/nm [154] and saturates at much lower fluences $\geq 1\times10^{13}$ [148] than for beams in the elastic collision regime. Compared to the earlier results, all irradiations presented in this thesis were performed with heavier ion species such as Xe, Au, Pb, and U plus complementary light ions (Cr and Ni). For the irradiation at ambient pressure, powder samples (purchased from Sigma-Aldrich™) were fixed on thin indium foils. During ion-beam exposure, the flux and fluence were controlled via a secondary electron transmission monitor (calibrated against a Faraday cup) that reduces the initial beam energy to 11.1 MeV/u. The range of all tested ions in ZrO_2 is $\sim$ 60 μm [22]. The ion flux was limited to $\sim$ 2 - 5$\times10^8$ ions/cm^2 to avoid excessive macroscopic sample heating. The fluence series covered values from 1×10^{11} ions/cm^2 up to 1×10^{13} ions/cm^2. The electronic energy loss $(dE/dx)_e$ within the sample is 10 keV/nm for Cr at 4.8 MeV/u, 9 keV/nm for Ni, 28 keV/nm for Xe, 40 keV/nm for Au, 42 keV/nm for Pb, and 53 keV/nm for U ions, calculated with the SRIM 2008 code [22]. Except for Cr, all irradiations were performed with an initial ion energy of 11.1 MeV/u. All irradiation parameters are listed in Table 5.2.

Ion	E_{init} (GeV)	$(dE/dx)_e$ (keV/nm)	Fluence Φ (ions/cm^2)	Pressure (GPa)	Initial structure	Final structure	Radius (nm)
macro-crystalline ZrO_2							
^{238}U	2.64	53	0.05 - 1.0×10^{13}	ambient	mono	tetragonal for $\Phi \geq 5\times10^{12}$	5.3
^{208}Pb	2.31	42	0.05 - 7.5×10^{12}	ambient	mono	tetragonal for $\Phi \geq 7\times10^{12}$	4.4
^{197}Au	2.19	40	0.05 - 1.8×10^{13}	ambient	mono	tetragonal for $\Phi \geq 1\times10^{13}$	4.0
^{132}Xe	1.46	28	0.05 - 1.0×10^{13}	ambient	mono	tetragonal for $\Phi > 2\times10^{13}$	2.8
^{59}Ni	0.66	9	0.05 - 2.0×10^{13}	ambient	mono	no transition induced	—
^{52}Cr	0.25	10	0.05 - 1.0×10^{14}	ambient	mono	no transition induced	—
nano-crystalline ZrO_2							
^{238}U	2.64	53	0.07 - 1.0×10^{13}	ambient	mono	tetragonal for $\Phi \geq 5\times10^{12}$	5.4
^{208}Pb	2.31	42	0.05 - 1.8×10^{13}	ambient	mono	tetragonal for $\Phi \geq 7\times10^{12}$	4.4

Table 5.2: Irradiation parameters for all samples irradiated at the UNILAC at ambient pressure conditions.

Raman spectra of ZrO_2 irradiated at ambient pressure with various fluences of Au and U ions are displayed in Figs. 5.4 and 5.5. Pristine ZrO_2 has 14 dominant Raman lines at 100, 178, 190, 222, 305, 334, 348, 382, 476, 503, 537, 560, 616, and 640 cm^{-1} corresponding to the low-symmetric monoclinic structure. For fluences up to 1×10^{12} ions/cm^2 the Raman spectra remain almost unchanged. At fluences around 2×10^{12} ions/cm^2, small modifications become visible, such as the decrease of the band at 100 cm^{-1} and merging of the double-band structures at 340, 550, and 630 cm^{-1}. At 5×10^{12} ions/cm^2 for U and 5×10^{12} ions/cm^2 for Au ions, new broad bands appear (indicated by the dotted lines in Figs. 5.4 and 5.5) at 148, 265, 465, and 640 cm^{-1} which are assigned to the tetragonal phase of ZrO_2 [148, 155, 153]. For Au and U ions, the transformation mainly proceeds in a fluence regime between 1×10^{12} and 1×10^{13} ions/cm^2, with marginal further changes at higher fluences. For lighter ions, such as Xe with an electronic energy loss almost two times lower than that of U, the fluence needed for saturation is much higher. For 1×10^{13} Xe-ions/cm^2, only $\sim$ 17 % of the sample volume changed into the tetragonal structure. For even lighter ions (Cr, and Ni), no transformation could be observed even at a fluence of 1×10^{14} Cr-ions/cm^2. This agrees with previous results by Benyagoub et al. who showed that the electronic energy loss needs to be above a threshold value of 13 keV/nm [3, 156]. Because the electronic energy losses of Ni (at 11.1 MeV/u) and Cr (at 4.8 MeV/u) are only 9 keV/nm and 10 keV/nm, respectively, no transformation is expected to occur. If a transformation occurred, we always identified a small contribution of the monoclinic phase. For the sample irradiated with 1×10^{13} U-ions/cm^2, e.g., the tetragonal fraction is limited to (90.1 $\pm$ 4.4) %. In agreement with previous measurements [106, 3], the transformation from monoclinic to tetragonal is obviously never completed. It is important to point out that the tetragonal structure of ZrO_2 obtained by simple temperature increase is not stable at room temperature. Therefore, the production route via ion irradiation is in that sense unique that it can not only provoke the transformation from monoclinic to tetragonal, but that this high-temperature phase is stabilized down to ambient temperature and can be measured even years after the irradiation.

Complementary X-ray diffraction measurements were performed on samples irradiated with 11.1 MeV/u U-ions (Fig. 5.6). Because the samples are very small, all X-ray measurements of samples irradiated under ambient conditions were performed at the DESY (P08-beamline) inside the gasket of a DAC (diameter $\sim$ 200 μm) serving as sample holder. The pristine sample exhibits its strongest peaks at 8.95° corresponding to the $[-111]_m$ reflex, and at 9.97° corresponding to the $[111]_m$ reflex of the

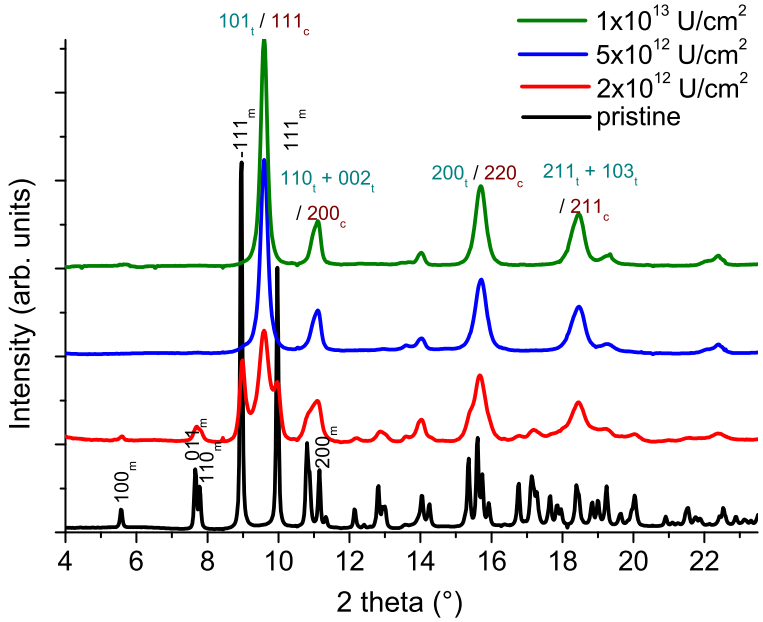

Figure 5.6: X-ray spectra of ZrO_2 irradiated at ambient pressure with 11.1 MeV/u U-ions for various fluences (same sample as in Fig. 5.5).

monoclinic structure. The calculated lattice parameter for pristine ZrO_2 are $a = (5.296 \pm 0.006)$ Å, $b = (5.094 \pm 0.007)$ Å, $c = (5.326 \pm 0.006)$ Å, and an angle $\beta = 99.40°$. Similar to the Raman data, for fluences $\geq 1\times10^{12}$ U-ions/cm^2 the monoclinic bands start to deteriorate and a new reflex at 9.60° appears which belongs probably the $[101]_t$ reflex of the tetragonal phase. Unfortunately, the cubic and the monoclinic phases of ZrO_2 display a very similar diffraction pattern making it almost impossible to distinguish between these two structural phases [157]. For both structures the strongest peak lies at 9.60° and could therefore correspond not only to the $[101]_t$ reflex of the tetragonal phase, but could also be the $[111]_c$ reflex of the cubic phase. Also the higher diffraction peaks are located at similar positions. Usually, the two phases can be distinguished by the splitting peak around 11.17° into two individual peaks belonging to the $[110]_t$ at 10.94° and $[002]_t$ at 11.13° of the tetragonal phase. Also at larger diffraction angles, a double peak e.g. $[211]_t$ and $[103]_3$ at around $\sim$ 18.5° corresponds to the tetragonal structure. Although no amorphization occurs in ZrO_2 during irradiation, the very high fluences induce strain or possibly nano-crystallization inside the sample, causes a broadening of the diffraction reflexes. Unfortunately, unambiguous identification of these two phases is also very difficult by Raman spectroscopy, because the Raman band of cubic ZrO_2 expected at 620 cm^{-1} is buried below the broad band at 640 cm^{-1} from the tetragonal structure. Probably, some fraction of the material changes into the cubic phase, but since the Raman signal definitely indicates tetragonal, we assume that this is the predominating structure after ion irradiation. The calculated lattice parameters for the tetragonal structure are $a = (3.592 \pm 0.006)$, and $c = (5.153 \pm 0.013)$ Å. ZrO_2 is one of the rare materials in which the high-temperature phase has a higher density than the room temperature phase, which leads to the fact that the monoclinic $\rightarrow$ tetragonal transition is accompanied by a density increase of $\sim$ 5 % [109].

5.1.4 Transformation mechanism: nano-crystallization vs. strain

Two possible mechanisms for the radiation induced transformation are discussed: lowering of the transition temperature due to nano-crystallization or local strain within the sample.
Several investigations have shown that the phase transition behavior of nano-crystalline materials can differ strongly compared to bulk material. The particle size can change the stability of structural phases not only at ambient conditions but also at high pressure [157]. Usually, the temperature needed for the different phase transitions decreases with decreasing grain size [158]. The same behavior can be observed for ZrO_2. With decreasing grain size, the ZrO_2 sample changes from monoclinic to tetragonal at room temperature. The lower transition temperature is due to the competition between surface energy and bulk energy. This changes the volumetric and surface enthalpy and entropy as well as the interfacial energy and strain [159]. Although monoclinic ZrO_2 has the lower free energy at room temperature, its surface energy (σ) is higher than that of the tetragonal phase (σ_m = 1.46 J/m^2 and σ_t = 1.1 J/m^2 for incoherent and σ_t = 0.55 J/m^2 for partially coherent interfaces) [160, 161]. Garvie et al. postulated that, when the two phases are at equilibrium, their free energies must be equal and can be expressed by the following formula [162, 161]:

$$\Delta G = \frac{4}{3}\pi r^3(\psi - \psi') + 4\pi r^2(\sigma - \sigma') + \frac{4}{3}\pi r^3(\epsilon - \epsilon') \stackrel{!}{=} 0 \tag{5.1}$$

- r_c = radius of a microcrystal
- ψ = free energy per unit volume of a crystal with infinite size
- σ = surface free energy
- ϵ = strain energy per unit volume for a particle

The first two terms take into account the changes in surface free energy and the last term the change in mechanical energy, evoked by strain due to the volume change caused by the transformation. One can see from Eq. 5.1 that for a critical radius r_c, ΔG can become zero at a temperature well below the transition temperature:

$$r_c = -\frac{3\Delta\psi}{\Delta\sigma + \Delta\epsilon} \tag{5.2}$$

$\Delta\sigma$ is equal to $q(1 - T/T_b)$ where q is the heat of transformation per unit volume (-2.82 $\times$ 10^8 J/m^3) and T_b is the transformation temperature of the bulk material (1470 K) [160]. $\Delta\psi$ is the difference of the interfacial energies and lies between 0.36 J/m^2 (for incoherent particles) and 0.91 J/m^2 (for partially coherent particles). The contribution of the strain energy due to volume change can be estimated by means of an equation, developed by Davidge at al. [163] for spherical particles in a matrix of different thermal expansion. This contribution amounts to 4.6 $\times$ 10^7 J/m^3 [161]. Inserting all values into Eq. 5.2, we obtain a critical radius between 6.1 and 15.3 nm. However, we still observed the monoclinic phase in crystals with a diameter of about 20 nm, and Bremholm et al. [164], also reported monoclinic ZrO_2 at a crystallite size of 10 nm. Considering that result, we can say that the crystal size has to be at

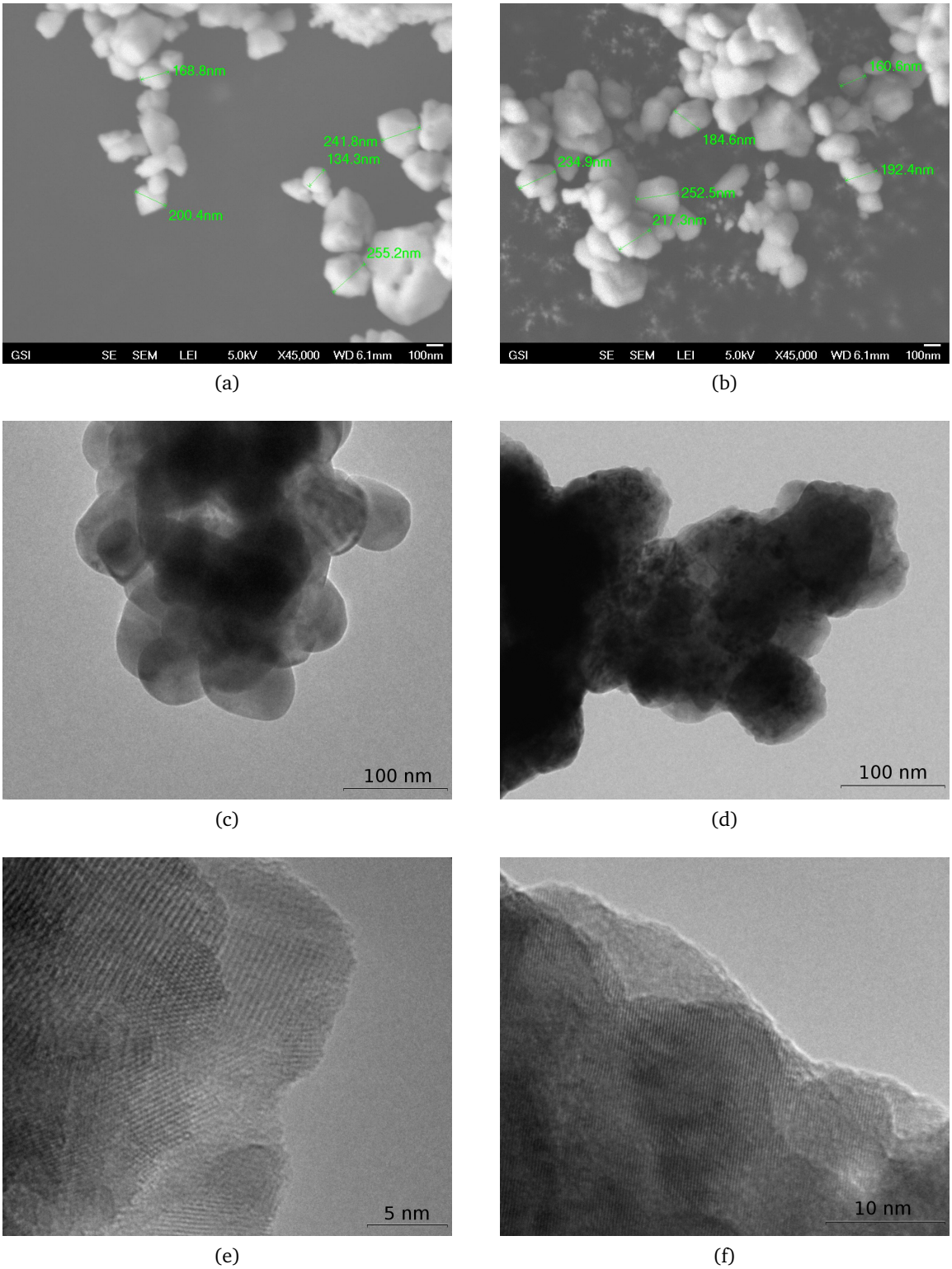

(a) (b)

(c) (d)

(e) (f)

Figure 5.7: Left column: REM (a) and TEM (c) and (e) of pristine ZrO_2. Right column: SEM (b) and TEM (d) and (f) of ZrO_2 irradiated with 1×10^{13} U-ions/cm^2.

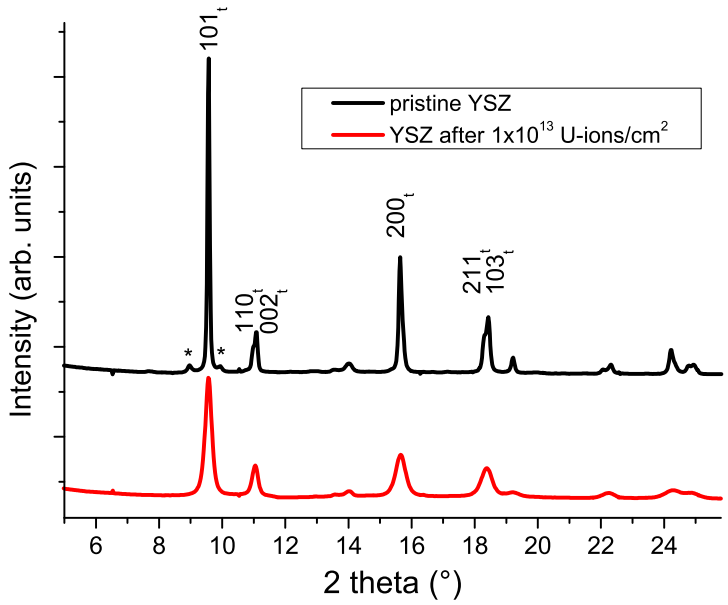

Figure 5.8: X-ray diffraction spectra of pristine and irradiated (1×10^{13} U-ions/cm^2) yttria-stabilized zirconia (YSZ). YSZ is mainly tetragonal at room condition, the asterisks indicate the bands belonging to the monoclinic fraction in the sample which has completely vanished after irradiation.

least below 20 nm in diameter to induce a monoclinic → tetragonal phase transition at room temperature. Therefore, the crystal size of pristine and irradiated ZrO_2 powder has been investigated by electron microscopy, such as scanning electron microscopy (SEM) and transmission electron microscopy (TEM), displayed in (Fig. 5.7). SEM images allow an instructive overview over both of the pristine (Fig. 5.7(a)) and irradiated (1×10^{13} U-ions/cm^2) samples (Fig. 5.7(b)). We estimate an average grain size of around 200 nm. Also TEM (Figs. 5.7(c) and (d)) investigations showed no nano-crystallization effect due to ion irradiation. Although the grain size did not change, we can see a contrast change in the irradiated sample (Fig. 5.7(d)). A ripple-like contrast observed in the TEM image is attributed to strain, leading to the assumption that radiation induced strain might be an explanation for the phase transition mechanism [165]. TEM images at highest magnification (Fig. 5.7(e)) show a lattice structure proving that after irradiation the sample is still crystalline and not amorphous. Recent results demonstrated that ZrO_2 with a crystal size of 3 nm, usually resistant to ion irradiation, can be amorphized by irradiation [166]. Summarizing, nano-crystallization could not be observed and can therefore be ruled out as transformation mechanism. But TEM images of irradiated samples point to stress within the sample as possible driving force behind the radiation induced phase transformation.

The radiation-induced phase transformation is very likely associated with radiation-produced interstitials or vacancies [167]. Several groups who investigated the radiation induced phase transition for low as well as high-energy ions [150, 137, 154], explained the mechanism by the production of oxygen vacancies. The presence of oxygen vacancies is considered as a requirement for a thermally induced phase transition [168]. Also in the case of tetragonal zirconia, artificially stabilized by addition of soluble oxides (e.g. Y_2O_3, MgO, CaO), the structure remains in the high-temperature phase because the dopants

create an oxygen vacancy for every unit of the dopant. The additional oxygen vacancies displace the remaining oxygen ions from their equilibrium positions in the tetragonal phase, so that the tetragonal → monoclinic transformation is suppressed [140]. Under ion irradiation, a large number of oxygen vacancies is produced. If they accumulate to vacancy clusters, the free volume can induce significant stress in the crystal that may relax via a phase transition [169]. Calculations showed that oxygen vacancies induce a strong local strain field in their neighborhood [170]. It is known that strain promotes the stability of the phase with the higher density [158], and due to the unique temperature-structure behavior, the high-temperature tetragonal ZrO_2 phase is 0.4 g/cm^3 denser than the monoclinic phase and is therefore the favored structure under stress. Using Landau's theory for phase transitions [171], Simeone et al. [151, 150] explained the transformation mechanism by also considering a local strain field induced by vacancies. Vacancies lower the critical transition temperature when reaching a certain threshold value. With respect to the free energy, the new crystalline phase is energetically the most favorable atomic configuration. The finding that significant amounts of ZrO_2 transform into the tetragonal phase only after ion bombarded with relative high fluences suggests that a single particle track does not induce sufficient defect density and strain to induce the phase switch. A second particle, hitting the same pre-damaged spot, then triggers the transition from the defective monoclinic structure to the dense tetragonal phase.

To investigate the strain in the sample, we use the X-ray diffraction data displayed in Fig. 5.6. Non-uniform strain (produced by point defects, plastic deformations, and poor crystallinity) leads to systematic shifts of atoms from their ideal positions, causing deviations from ideal crystallinity and therefore lead to a broadening of the diffraction lines. Information about the microstructure of the material can be obtained by the analysis of this broadening. The width of a diffraction line can be described either by the full width at half maximum (FWHM) or, more commonly used, the integral breadth β which is the total area under the peak divided by the peak intensity. There are three main sources of diffraction line broadening: the crystallite size broadening (β_{size}), the strain broadening (β_{strain}), and the instrumental broadening (β_{instr}), so that:

$$\beta_{obs} = \beta_{size} + \beta_{strain} + \beta_{instr} \tag{5.3}$$

Table 5.3: Integral breadth β for two reflections, calculated microstrain ϵ, and calculated crystallite size L for ZrO_2 and yttria stabilized ZrO_2 (YSZ). The asterisks $*$ indicate that for unirradiated ZrO_2 different diffraction peaks at similar positions were used.

Fluence (ions/cm^2)	**β for $[101]_t$**	**β for $[200]_t$**	**microstrain ϵ**	**crystal size L (nm)**
ZrO_2				
0	0.094 ± 0.002	0.155 ± 0.003*	0.0016 ± 0.0002*	120 ± 36
2×10^{12}	0.547 ± 0.042	0.759 ± 0.051	0.0092 ± 0.0008	62 ± 9
5×10^{12}	0.316 ± 0.036	0.512 ± 0.041	0.0078 ± 0.0006	72 ± 12
1×10^{13}	0.315 ± 0.038	0.508 ± 0.048	0.0075 ± 0.0005	75 ± 11
YSZ				
0	0.095 ± 0.002	0.181 ± 0.003	0.0022 ± 0.0004	104 ± 33
2×10^{12}	0.368 ± 0.039	0.560 ± 0.051	0.0037 ± 0.0006	75 ± 18
5×10^{12}	0.368 ± 0.039	0.560 ± 0.051	0.0051 ± 0.0008	68 ± 18
1×10^{13}	0.368 ± 0.039	0.560 ± 0.051	0.0053 ± 0.0008	66 ± 19

The instrumental broadening occurs due to nonideal optics, wavelength dispersion, and detector resolution, to name a few sources. The size dependence has been first described in 1918 by Paul Scherrer, who observed that the peak width is inversely proportional to the crystalline size L and derived the following formula [172]:

$$L = \frac{k\,\lambda}{\beta_{size}\,cos(\Theta)} \tag{5.4}$$

where k is the Scherrer constant, a number that lies between 0.87 and 1.0. For cubic structures, $k = 0.9$. λ is the X-ray wavelength and β the integral breadth (in radians 2Θ). In 1944, Stokes observed a line broadening of a different sort which could be attributed to strained or imperfect crystals. The average strain ϵ in the crystal shows following dependence [173]:

$$\epsilon = \frac{\beta_{strain}}{4\,tan(\Theta)} \tag{5.5}$$

so that the complete line broadening can be summed to [42]:

$$\beta_{obs} = \frac{0.9\,\lambda}{L\,cos(\Theta)} + 4\,\epsilon\,tan(\Theta) + \beta_{instr} \tag{5.6}$$

The Rietveld method combined with Fourier analysis can be used as procedure for simultaneous refinement of structural and microstructural disorder parameters [174]. A pseudo-Voigt function is used to describe the line broadening. The results are then deconvoluted into the gaussian and lorentzian fractions. It is assumed that the lorentzian component of the peak profile is entirely attributed to the crystallite size effect, while the gaussian component is connected to microstrain [174]. The evolution of the integral breadth of the two most intensive peaks of tetragonal ZrO_2 ($[101]_t$ at 9.6° and $[200]_t$ at 15.7°) is plotted against the ion fluence for U ions in Fig. 5.9. Because there exists no tetragonal phase for unirradiated ZrO_2, the integral breadth of the irradiated samples is compared to that of the monoclinic reflections at similar positions such as 10.0° and 15.6°. For additional comparison, commercial yttria-stabilized ZrO_2 (8 % Y_2O_3 doped ZrO_2) which already exists predominantly in the tetragonal phase, was also irradiated with 1×10^{13} U-ions/cm^2 (see Fig. 5.8). The integral breadth and calculated strain and sample size are listed in Table 5.3. The intergal breadth of the $[101]_t$ reflex of ZrO_2 irradiated with 1×10^{13} U-ions/cm^2 amounts to 0.315 ± 0.04, and is therefore more than three times higher than for the $[111]_m$ reflection of pristine ZrO_2 which is 0.094 ± 0.002. The same behavior can be observed for the reflections at higher angle around 15.6°. For YSZ, where the reflection of unirradiated and irradiated material can be compared directly, a similar broadening by a factor of three occurs. Interestingly, the integral breadth does not simply increase with increasing ion fluence but exhibits a maximum at 2×10^{12} U-ions/cm^2, which is five times as high compared to pristine ZrO_2 before saturating for higher fluences. This leads to the same behavior in the calculated microstrain (see Fig. 5.10).

The microstrain ϵ, calculated from Rietveld profile parameters for pristine ZrO_2, is 0.0016 ± 0.0004 which is comparable to literature values [175]. It then peaks at 0.0092 ± 0.0008 for 2×10^{12} U-ions/cm^2 before saturating at around 0.0075 ± 0.0005. The high ϵ-value for 2×10^{12} U-ions/cm^2 might be due to

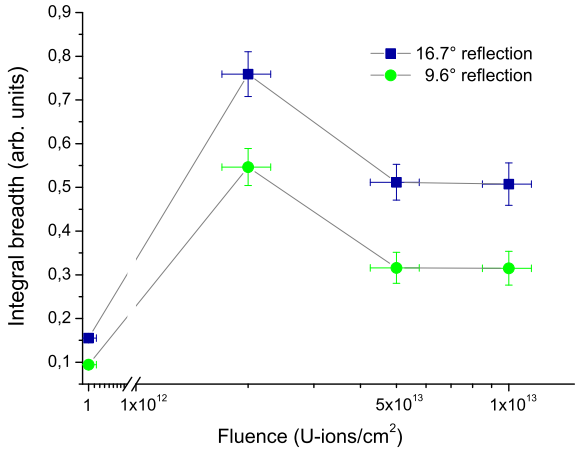

Figure 5.9: Integral breadth for the $[101]_t$ and $[200]_t$ reflections of ZrO_2 versus the ion fluence.

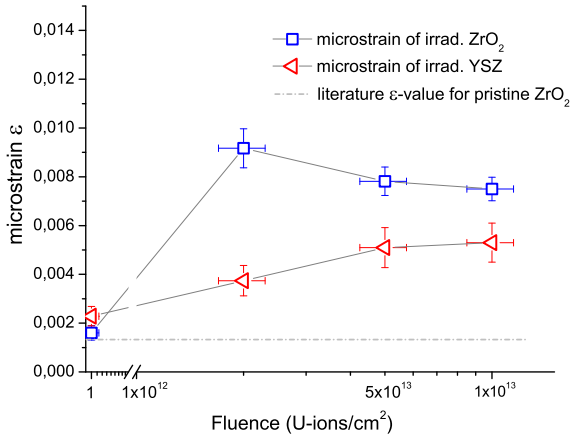

Figure 5.10: Calculated microstrain ϵ versus ion fluence for normal and stabilized (YSZ) ZrO_2.

the fact that at this fluence we have a mixture of both structural phases in the sample. The continuous transformation induced by irradiation allows the coexistence of both structures in the same sample. Domains of the tetragonal structure grow in a monoclinic matrix inducing more stress due to boundary effects. Since monoclinic and tetragonal ZrO_2 have a large density difference (~ 0.4 g/cm^3) and thermal expansion mismatch [175], an occurrence of both structures in the same sample inevitably leads to additional strain especially on the domain boundaries. After all of the sample material changed into the tetragonal form, no phase boundaries remain, reducing the strain contribution only to radiation induced defects such as vacancies and interstitials. This explains why YSZ, which exists already in the tetragonal phase before irradiation, shows no enhanced microstrain effect for 2×10^{12} U-ions/cm^2, because no phase change occurs and the strain increase is only radiation induced. In table 5.3, also the calculated crystallite size is displayed. Although these values lie lower than for the TEM observations, they are still large enough (> 20 nm) to exclude that the transformation mechanism is induced by nanocrystallization.

5.1.5 Transformation process

To shed more light on the mechanism of this transformation, Raman spectra of fluence series were analyzed for samples irradiated with 11.1 MeV/u Xe, Au, Pb, and U ions. To quantify the contribution of the monoclinic and tetragonal phases, we evaluated the intensity ratios (X_m) of the different Raman bands at 178, 190, and 148 cm^{-1}. The background was considered by subtracting the baseline between $\sim$ 125 cm^{-1} and $\sim$ 205 cm^{-1}. The monoclinic fraction was calculated by applying the formula by Kim et al [155]:

$$X_m = \frac{I_m(178\ cm^{-1}) + I_m(190\ cm^{-1})}{I_m(178\ cm^{-1}) + I_m(190\ cm^{-1}) + I_t(148\ cm^{-1})} \tag{5.7}$$

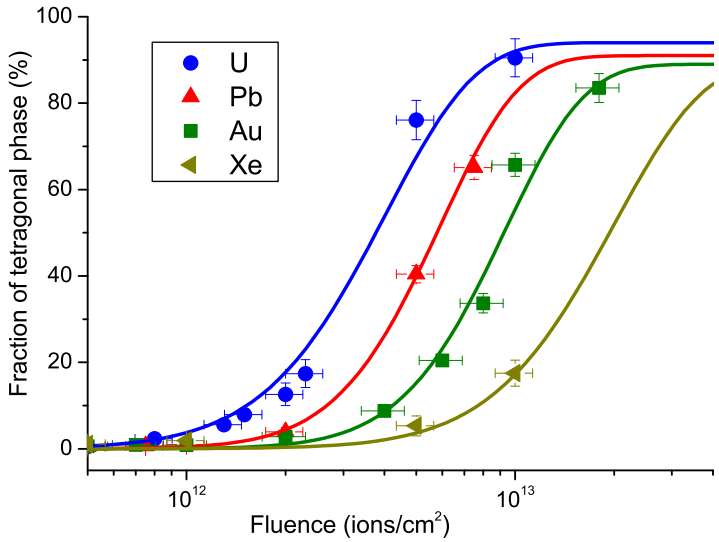

Figure 5.11: Concentration evolution of the tetragonal phase versus fluence for four different ion species (Xe, Au, Pb, U) deduced from the Raman data. The solid curves are the best fit of Eq. 5.9 to the experimental data using a cascade-overlap model.

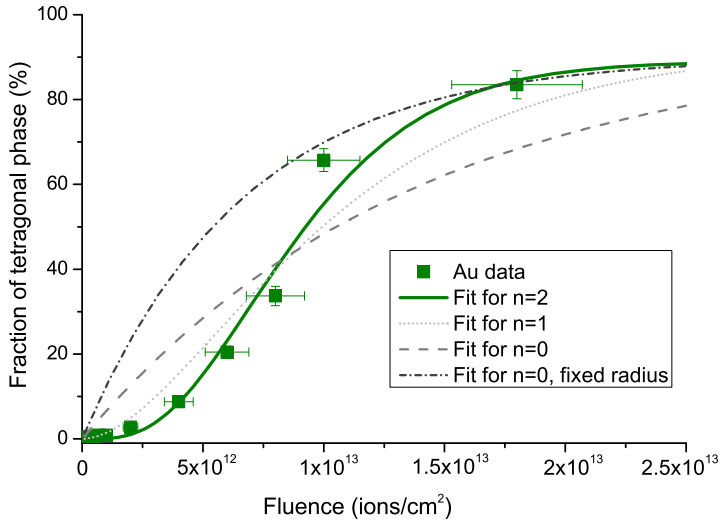

Figure 5.12: Concentration evolution of the tetragonal phase versus fluence for Au ions. The solid curves is the best fit of Eq. 5.9 with n = 2. For comparison, the dotted line represents a fit of Eq. 5.9 with n = 1. The dashed and dash/dotted line are fits for a single ion hit mechanism n = 0 (Eq. 5.8). The dashed line is a free fit, whereas the dash/dotted line is the best fit with a fixed radius calculated for n = 2.

For all tested ion species, the tetragonal fraction (100-X_m) in % plotted versus the ions fluence shows a sigmoidal evolution (Fig. 5.11). Such a sigmoidal behavior is commonly observed for non-amorphizable ceramics at ambient temperature [104, 169] and typically ascribed to a two-hit process. This is in contrast to amorphizable materials where each ion impact produces an individual amorphized track of cross section $\sigma = r^2\pi$ and radius r. For such a one-hit process, the fraction of the transformed material $A(\Phi)$ increases with fluence according to the following exponential law described by [103]:

$$A(\Phi) = A(\infty)(1 - e^{-\sigma\Phi}) \tag{5.8}$$

where σ is the total damage cross-section given as an area, Φ is the ion fluence, and $A(\infty)$ denotes the fraction of transformed material at saturation.

Fitting this formula to our Raman data does not yield satisfactory results (see dotted/dashed lines in Fig. 5.12). The monoclinic phase of ZrO_2 can obviously not be transformed into the tetragonal phase by a single ion hit but needs pre-damaging by multiple ion impacts. The effect of damage superposition is described by the Gibbons cascade-overlap model [103, 104] with the following general expression:

$$A(\Phi) = A(\infty)\left[1 - \left(\sum_{k=0}^{n} \frac{(\sigma\Phi)^k}{k!}\right) e^{-\sigma\Phi}\right] \tag{5.9}$$

For all ion species, we find best agreement with our data for a double-overlap situation (i.e. $n = 2$) presented by the solid lines in Figs. 5.11 and 5.12. The results of the fits are $A(\infty) = (93.7 \pm 4.1)$ %, $\sigma = (8.69 \pm 0.21)\times10^{-13}$ cm^2 for U-ions, $A(\infty) = (91.3 \pm 4.0)$ %, $\sigma = (6.18 \pm 0.32)\times10^{-13}$ cm^2 for Pb-ions, $A(\infty) = (89.9 \pm 4.7)$ %, $\sigma = (5.04 \pm 0.18)\times10^{-13}$ cm^2 for Au-ions, and $A(\infty) = (87.7 \pm 5.6)$ %, $\sigma = (2.29 \pm 0.45)\times10^{-13}$ cm^2 for Xe-ions. As has been reported in the literature (eg. [148, 137]), the transformation is never complete but saturates around 90 %. Assuming that the damage cross section σ can be described by a homogeneously damaged cylinder with a cross section $\sigma = \pi r^2$, the following track radii can be deduced: $r = (5.3 \pm 0.2)$ nm for U-ions, (4.4 ± 0.2) nm for Pb-ions, (4.0 ± 0.2) nm for Au-ions, and (2.7 ± 0.3) nm for Xe-ions. The results give evidence that heavy-ion irradiation at ambient pressure induces a structural change into the tetragonal phase only if the structure is pre-damaged by complete coverage of ion tracks. For U-ions ($r = 5.3$ nm), complete track coverage requires fluences of at least $> 1.5\times10^{12}$ ions/cm^2. Above this fluence, each following ion hits an already pre-damaged region, and transforms the damaged monoclinic structure into the tetragonal phase. This agrees nicely with the observed results.

5.1.6 Thermal spike calculations

The results from the previous section will be compared to theoretical results obtained by calculations using the inelastic Thermal Spike Model introduced in chapter 2.1.3.2. To calculate the temporal and spacial development of the temperature within the sample, numerous physical and thermal properties (such as thermal diffusivity, melting and boiling temperatures, specific heat capacity and conductivity, and melting and evaporation heat) have to be known about the target material. The electronic and atomic systems of the target are considered separately. First, the energy of the incoming ion is transferred

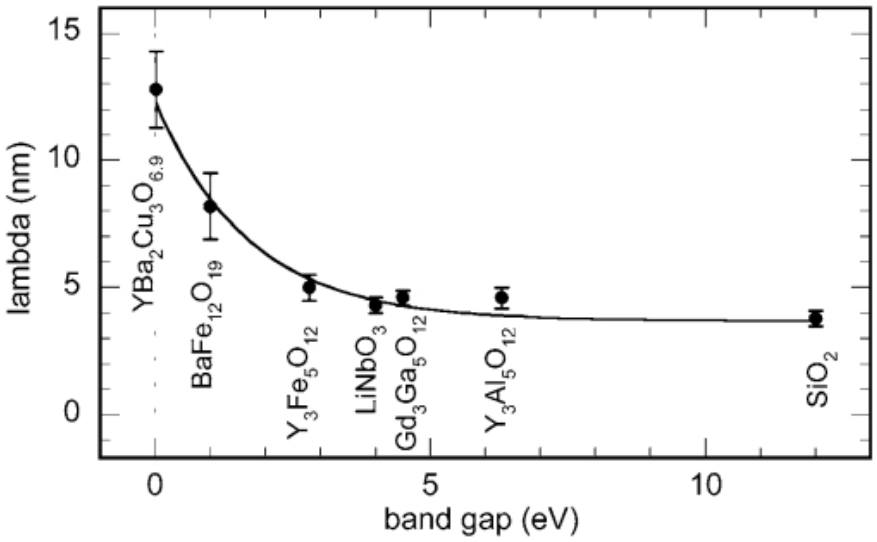

Figure 5.13: Electron-lattice interaction mean free path λ from thermal spike fitting as a function of the band gap energy E_g for several crystalline oxide materials. The diagram was taken from [176].

to the electrons of the target. Afterwards, the energy is transferred to the lattice atoms by electron-lattice interaction leading to a large increase in temperature along the ion trajectory [30]. The thermal process of the atomic and electronic systems can be modeled by using a cylindrical geometry which looks at small volumes with a cylindrical shape (from r to $r + dr$) in a small slice of thickness (dx) along the ion trajectory. For small dx and an assumed homogeneous energy input, the temperature does not change in x direction. The temperature gradient exists solely in radial direction. The classical expression of heat flow can then be described by the two non-linear differential equations (Eq. 2.5 and 2.6). The critical part of the inelastic thermal spike model is the electron-phonon coupling constant g which is unknown for insulating materials. However, g is linked to the electron-lattice interaction time τ_a by the relation $\tau_a = C_e/g$ [177] and to the electron-lattice interaction mean free path λ by the relation $\lambda^2 = D_e\tau_a = D_eC_e/g$, where C_e is the specific heat and D_e the diffusivity [30]. λ defines the volume in which the energy is deposited, and describes the energy density. Therefore, if the electronic energy diffusivity decreases, the electron-phonon coupling should also decrease [178]. For an insulating material, the coupling constant g is set to zero when the electron temperature becomes less than the lattice temperature. Katina et al. [179] proposed that the energy dissipation in the electronic system proceeds via the ionization of bound electrons at the periphery of the excited region. The energy stops spreading when the electron energy becomes smaller than the minimum ionization energy. Therefore, a link between λ and the band gap energy E_g, which is the minimum ionization energy of an electron in insulators, can be assumed [30]. Toulemonde et al. [30] used a large set of data for which the radiation induced damage track radii were known. The λ values were then deduced from fitting of the track radii and plotted versus the band gap energy of the corresponding material (see Fig. 5.13). As can be seen from Fig. 5.13, if the band gap energy is larger than 2.8 eV, λ decreases only slightly and stays in the same region between 4 and 5 nm, suggesting that crystalline insulators behave nearly in the same way concerning the electron energy transfer towards the atoms [180]. The relation between band gap and mean free path seems reasonable if one considers that the cooling of hot electrons occurs via

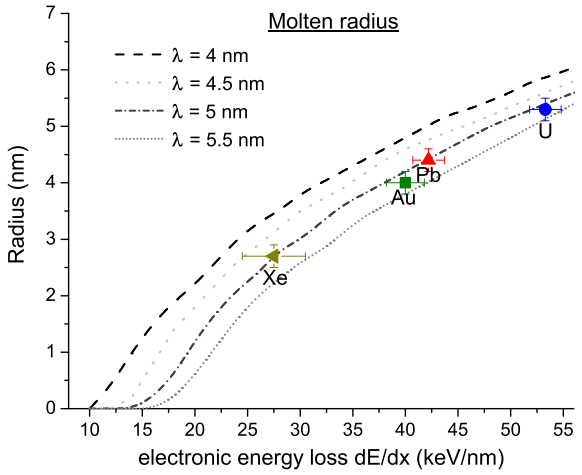

Figure 5.14: Measured track radii in ZrO_2 produced by Xe, Au, Pb, and U ion irradiation at 11.1 MeV compared to thermal spike calculations assuming track creation by melting $T > T_m$ for various mean free path λ.

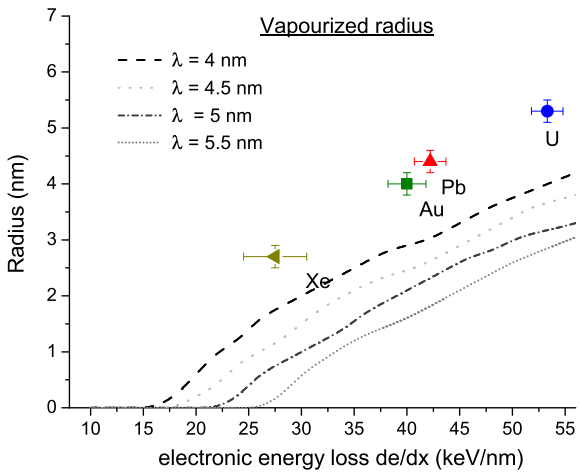

Figure 5.15: Measured track radii in ZrO_2 produced by Xe, Au, Pb, and U ion irradiation at 11.1 MeV. The curves correspond to the cylinder of matter which overcomes the temperature of vaporization $T > T_v$ calculated for various values of mean free path λ.

excitation of peripheral cold electrons from the valence band to the conduction band which is directly linked to the band gap energy [176]. The band gap energy in ZrO_2 changes with the crystal structure but lies between 3.0 and 5.3 eV [181]. For pure monoclinic ZrO_2 a band gap energy of 3.58 eV can be assumed [182]. From Fig. 5.13 one can derive that λ has to be between 4.5 and 5.5 nm. Figures 5.14 and 5.15 show the deduced track radius in ZrO_2 created by ion irradiation with Xe, Au, Pb, and U ions at an energy of 11.1 MeV/u, compared to the theoretical thermal spike calculations for different λ values from 4 - 5.5 nm. Figure 5.14 shows the results for the case of a track formation by melting of the target material. This means that the energy injected into the sample is high enough to raise the temperature from the irradiation temperature to the melting temperature (2960 K for ZrO_2). The curves in Fig. 5.15 correspond to the cylinder of material where the temperature reached the vaporization temperature (4600 K for ZrO_2). Both, melting and vaporization, have been proposed for the damage formation mechanism, but obviously the molten-track hypothesis agrees best with the experimental data. The measured track radii for all tested ion species coincide (within error bars) well with the theoretical values calculated for the molten-track mechanism. Best agreement occurs for $\lambda = 5$ nm which is quite reasonable assuming a band gap energy of 3.58 eV (see Fig. 5.13). The thermal spike calculations not only agree with the measured damage track radius but are also able to predict the energy loss thereshold of $\sim$ 13 keV/nm that has been discovered by Benyagoub et al. [3]. To test the influence of the thermal conductivity and the initial target temperature that might vary under irradiation condition, several calculation series with different parameters were performed. Change of the thermal conductivity by a factor of 10 (from 1.6 - 16 W/K m) created no difference in the calculated results. Initial target temperature increase by 100 K as starting temperature, which might be the case for high flux irradiations, also produced no changes in the calculations. Although the thermal spike model is still inconclusive in

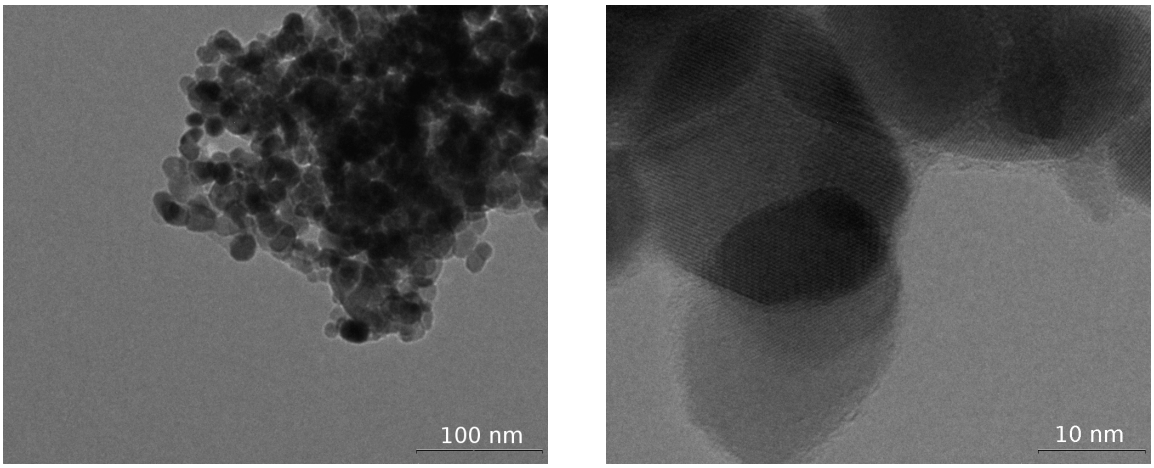

Figure 5.16: Transmission electron microscopy images of nano-crystalline ZrO_2.

some points, e.g., assumption of a non-Gaussian temperature distribution and of local equilibrium in a highly excited system [183], it seems to provide agreement of all important characteristics of the energy transfer mechanisms with the experimental data. In conclusion, the thermal spike model is a valuable tool for the prediction of damage cross sections produced by ion irradiation.

5.1.7 Comparison macro-to-nano-crystalline ZrO_2

In the previous chapter, some remakes were made regarding nano-crystallization and its influence on the phase transformation process. From literature it is known that for extremely small particle size (~ 3 nm), ZrO_2 can be amorphized [166]. If the phase transformation was due to nano-crystallization induced by ion impact, this transition should occur at much lower fluences if the starting material is close to the critical particle size. To compare the results of macro-crystalline and nano-crystalline ZrO_2, additional nanopowder from Sigma-Aldrich™was purchased. The manufacturer guarantees a sample size < 100 nm, and TEM investigations showed that the average grain size is about 20 nm (see 5.16), which is in the range of critical crystallite size for the stabilization of the tetragonal phase at ambient temperature [162]. First, it is important to mention that in spite of this small size the sample is still monoclinic, which could be confirmed by Raman and X-ray diffraction measurements. The Raman spectrum of a pristine nano-crystalline sample is displayed as inset in Fig. 5.17. Irradiation series with Au and U ions have been performed for fluences between 5×10^{11} to 1.8×10^{13} ions/cm^2. The tetragonal fraction from the Raman spectra was extracted, as described in chapter 5.1.5, and plotted versus the ion fluence. The evolution of the tetragonal amount is very similar to macro-crystalline ZrO_2. And even for fluences as high as 1.8×10^{13} Au-ions/cm^2 no amorphization occurs. The only difference worth mentioning is that in the pristine material as well as in the sample irradiated with low fluence, the tetragonal amount is slightly higher in the nano-crystalline sample. Using Eq. 5.9 one can derive the damage cross section and therefore the ion track radius. The results of the fit are $A(\infty) = (98.2 \pm 4.3)\,\%$, $\sigma = (9.32 \pm 0.70)\times10^{-13}\,\mathrm{cm}^2$ for U-ions and $A(\infty) = (97.4 \pm 4.3)\,\%$, $\sigma = (6.14 \pm 0.5)\times10^{-13}\,\mathrm{cm}^2$ for Au-ions. From this we obtain a damage track radius of (5.4 ± 0.3) nm for U and (4.4 ± 0.3) nm for Au ions. The extracted results are also listed in Table 5.2. Obviously, radiation induced nano-crystallization is not

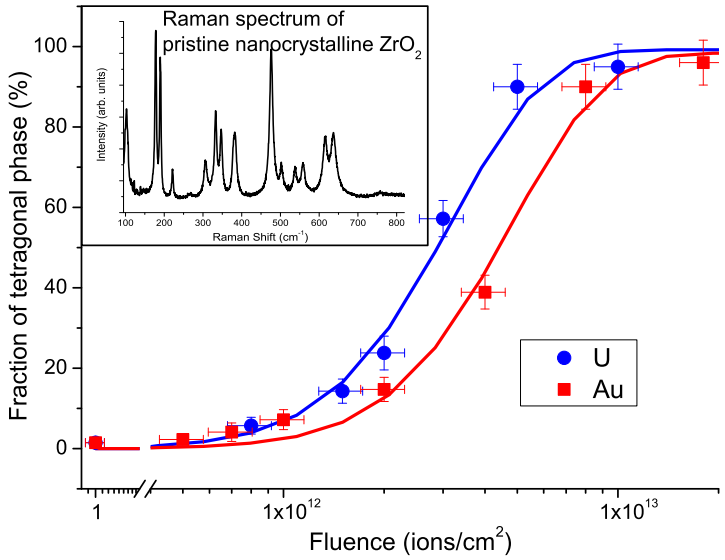

Figure 5.17: Tetragonal fraction versus fluence for Au and U ions, deduced from Raman data. The solid curves are the best fits of Eq.5.9 to the experimental data using a cascade-overlap model. The inset shows a Raman spectrum of pristine nano-crystalline ZrO_2.

the main force behind the transformation process, since both nano- and macro-crystalline ZrO_2 show the same radiation response.

5.1.8 Pressure dependence of pristine ZrO_2

Before combining irradiation and pressure in one experiment, the influence of pressure alone has to be investigated. Therefore, ZrO_2 powder was hydrostatically compressed in a diamond anvil cell, and Raman measurements were performed at different pressures. The Raman results of pressurized ZrO_2 are shown in Fig. 5.18. From one measurement to the next, the pressure was increased by about 5 GPa. At ambient pressure and temperature, 18 vibration modes (9 longitudinal and 9 transversal) of ZrO_2 are expected to be Raman active [184], but only 14 modes are visible in the spectrum. Due to the low symmetry of the atomic positions and the large mass difference of zirconium and oxygen, it can be expected that vibrations of the light and heavy ions can be separated [185]. Zr atom displacements correspond to the low frequency part (smaller Raman shifts up to ~ 400 cm^{-1}), and O atom displacements to the rest of the spectrum. Up to a pressure of 5 GPa no structural change is observed. However bands show a strong blue shift due to the pressure induced decrease of the lattice volume. At 9 GPa, there exists a mixture of the monoclinic phase and the first high-pressure phase orthorhombic I. New bands at 146, 176, 221 and 379 cm^{-1} belong to the high-pressure phase. Although the phase transformation starts at around 5 GPa, the monoclinic phase coexists up to 13 GPa along with the ortho-I phase. At 17 GPa the sample is completely transformed. Unfortunately, for pressures above 11 GPa, the pressure medium starts to freeze up so that the sample stays no longer under hydrostatic pressure. This uniaxial strain causes additional broadening of the Raman lines. For higher pressures the Raman signal becomes very weak and a change in the spectra is difficult to detect. At around 30 GPa, the bands at the lower-frequency region begin

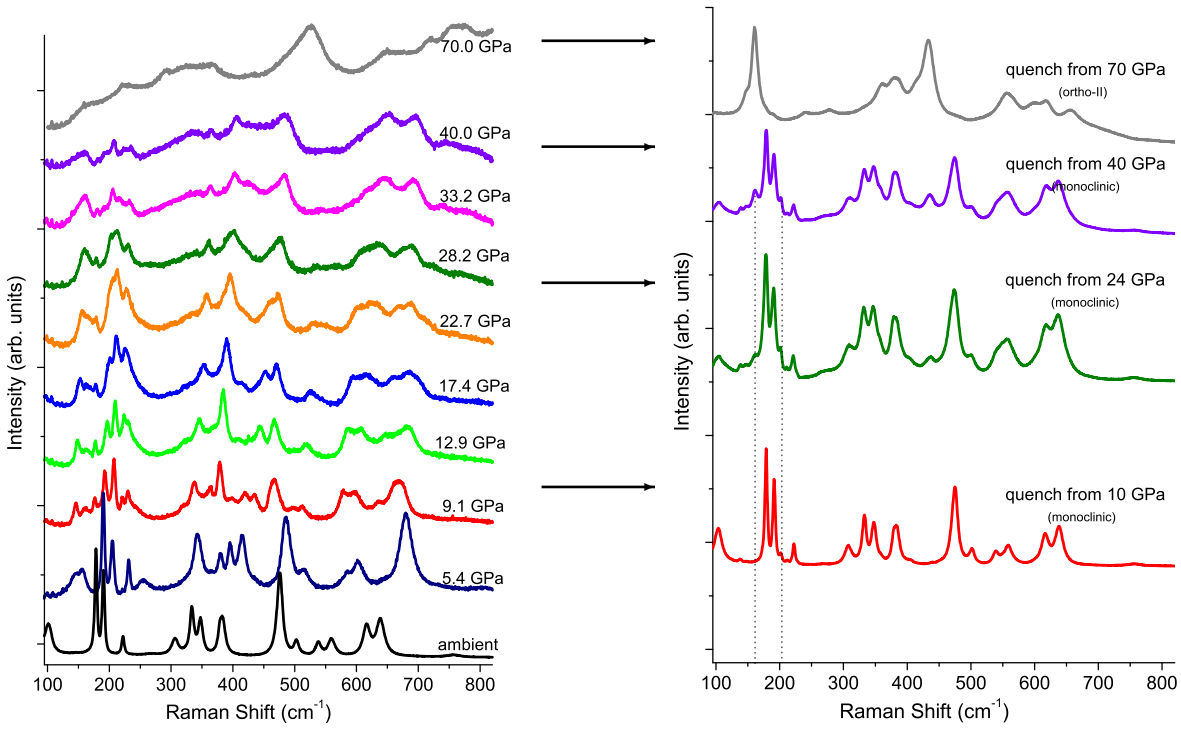

Figure 5.18: Left: Raman spectra of ZrO_2 at various pressures. Right: Raman spectra of ZrO_2 quenched from different pressures.

to disappear and the band at 480 cm^{-1} belonging to the second high-pressure phase (orthorhombic-II) becomes more pronounced. As mentioned earlier, at room temperature the transition from the ortho-I to ortho-II phase is very sluggish, so that even at 40 GPa there is still a mixture of ortho-I and ortho-II phase. At very high pressures (70 GPa), ZrO_2 exists purely in the ortho-II phase. The band previously (at 30 GPa) at 480 cm^{-1} has now shifted to 526 cm^{-1} and is the dominating one in the spectrum. Very important to know is the remaining structure after pressure release, the so-called quenching. To test in which phase the sample exists after quenching from various pressures, several pressurization and quenching cycles have been performed. The quenching results from 10, 24, 40, and 70 GPa are shown in the right graph of Fig. 5.18.

The sample quenched from 10 GPa looks almost like a pristine sample. As the ortho-I phase is not quenchable to ambient conditions, the sample changed completely back into the monoclinic structure. Only a small shoulder at 201 cm^{-1} indicates that this sample is not virgin. Also the sample quenched from 24 GPa and surprisingly also the one quenched from 40 GPa changed back into the monoclinic structure. Only tiny shoulders at 161 and 201 cm^{-1} indicate some residue of the ortho-I phase which might be due to still unrelaxed grains within the sample. For the 24 GPa sample this was expected, because at this pressure the non-quenchable ortho-I is predominant. Surprisingly, also the sample quenched from 40 GPa still changes back into the monoclinic structure. Obviously, at 40 GPa the mixture of ortho-I / ortho-II is in favor of the ortho-I structure, and therefore no high-pressure structure could be retained. In the literature, a transition pressure of these two phases between 28 and 35 GPa is mentioned, but this is just when the ortho-II structure starts to appear. Because the ortho-I → ortho-II transformation is reconstructive, the transition is very inert and stretches over a long pressure regime. Additional energy

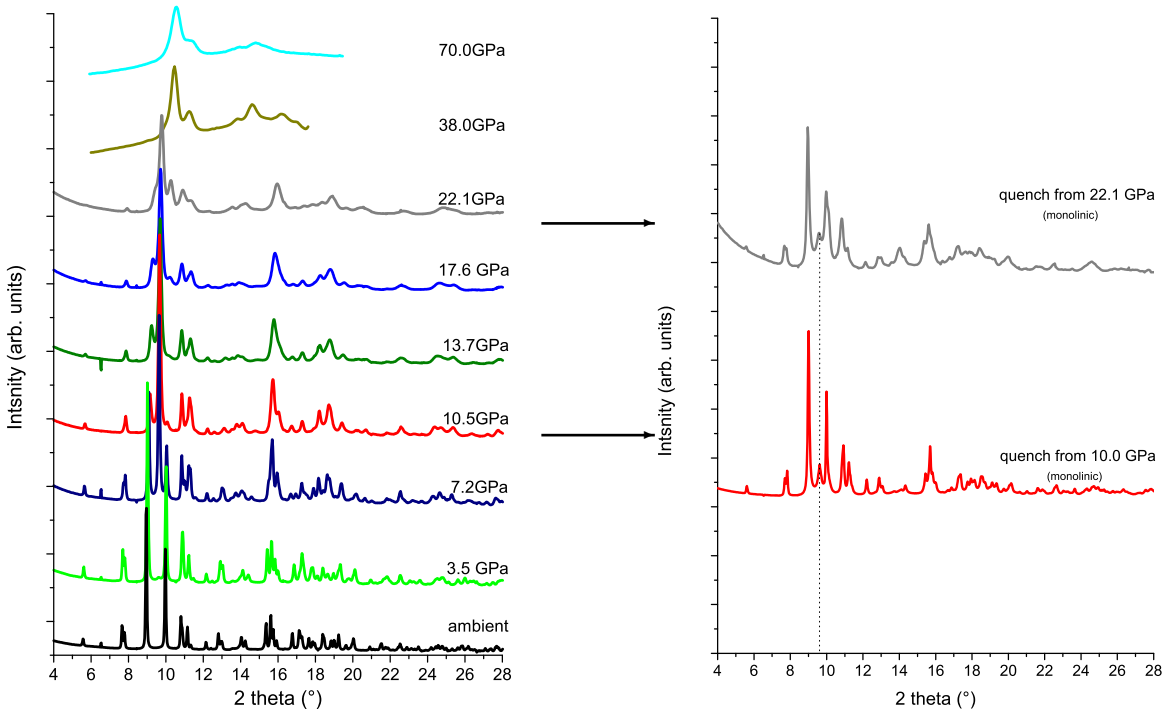

Figure 5.19: Left: X-ray diffraction pattern of ZrO_2 at various pressures. Right: X-ray diffraction pattern of ZrO_2 quenched from different pressures.

provided by high temperature helps to accelerate the phase transition. Above 600 °C, the ortho-II phase occurs already at 12.5 GPa, but in this case the transition does not start from the ortho-I but from the high-temperature tetragonal structure. It needs to be stressed, that even after pressurization up to 40 GPa the monoclinic structure was obtained after pressure release (quench). The sample quenched from 70 GPa shows a different result. At 70 GPa, ZrO_2 is well in the stability field of the ortho-II structure and with pressure excess of about 40 GPa from the transition boundary, only this phase can be expected. The ortho-II structure is the highest-pressure phase in ZrO_2 and stable up to at least 100 GPa [119]. Since the ortho-II phase (once produced) is quenchable, it can be maintained at ambient pressure. The gray (upper) spectrum on the right hand side in Fig. 5.18 shows the Raman spectrum of quenched ortho-II ZrO_2. The ortho-II spectrum shows eight new Raman bands at 161, 361, 382, 432, 556, 600, 618, and 657 cm^{-1}. This small number of bands indicate that the ortho-II phase has a crystal structure with high symmetry. From the Raman pressure series we conclude that up to 30 GPa we can be certain not to reach the quenchable ortho-II,

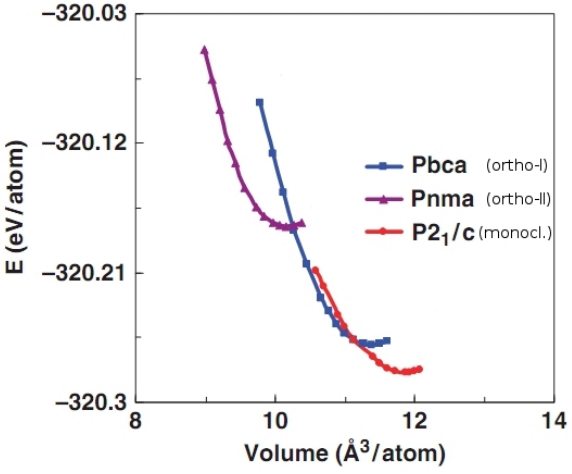

Figure 5.20: Computed energy of ZrO_2 phases as a function of volume for the monoclinic ($P2_1/c$), ortho-I (Pbca), and ortho-II (Pnma) structures. Diagram taken from [125]

Pressure (GPa)	Phase	a (Å)	b (Å)	c (Å)
ambient	monoclinic (100 %)	$(5.296 \pm 0.007)_m$	$(5.094 \pm 0.006)_m$	$(5.326 \pm 0.006)_m$
3.5	mono + ortho-I (2.1 ± 0.8) %	$(5.290 \pm 0.007)_m$	$(5.085 \pm 0.007)_m$	$(5.304 \pm 0.007)_m$
7.2	mono + ortho-I (53.4 ± 3.5) %	$(10.036 \pm 0.004)_{o-I}$	$(5.293 \pm 0.003)_{o-I}$	$(5.061 \pm 0.004)_{o-I}$
10.5	mono + ortho-I ((80.2 ± 4.2) %)	$(9.993 \pm 0.006)_{o-I}$	$(5.231 \pm 0.007)_{o-I}$	$(5.046 \pm 0.007)_{o-I}$
13.7	mono + ortho-I (96.5 ± 3.2) %	$(9.814 \pm 0.012)_{o-I}$	$(5.197 \pm 0.011)_{o-I}$	$(5.058 \pm 0.011)_{o-I}$
17.6	ortho-I (100 %)	$(9.698 \pm 0.016)_{o-I}$	$(5.111 \pm 0.016)_{o-I}$	$(5.047 \pm 0.017)_{o-I}$
22.1	ortho-I (100 %)	$(9.559 \pm 0.020)_{o-I}$	$(5.155 \pm 0.019)_{o-I}$	$(5.002 \pm 0.024)_{o-I}$
38.0	ortho-II (100 %)	$(5.453 \pm 0.004)_{o-II}$	$(3.121 \pm 0.003)_{o-II}$	$(6.265 \pm 0.004)_{o-II}$
70.0	ortho-II (100 %)	$(5.311 \pm 0.008)_{o-II}$	$(3.109 \pm 0.007)_{o-II}$	$(6.179 \pm 0.008)_{o-II}$

Table 5.4: Phase compositions of ZrO_2 at various pressures and list of lattice parameters for the predominating phases.

and that pressure alone in this regime can definitely not produce any change in the high-temperature polymorph.

For completeness, Figure 5.19 shows X-ray diffraction data of pressurized ZrO_2. Up to 22 GPa, the measurements were performed at DESY with a wavelength of 0.49467 Å. Unfortunately, due to the limit of beamtime only diffraction images up to this pressure could be gathered. But two X-ray diffraction images at higher pressures (38 and 70 GPa) were made with a commercial Bruker diffractometer with a wavelength of 0.7108 Å (Mo K_α) at the Bavarian Geological Institute (BGI) in Bayreuth, Germany. These spectra are plotted (wavelength-corrected) in Fig. 5.19. Up to a pressure of 3.5 GPa, no change in the sample phase is observed, whereas at 7.2 GPa a new band between the strong monoclinic bands appears at 9.64° which corresponds to the $[211]_o$ reflection of the ortho-I phase. In agreement with the Raman data we observe a mixture of monoclinic and ortho-I phases. Quantative Rietveld analysis of both structures shows a residual monoclinic fraction of (46 ± 4) %. With the increase of pressure, the monoclinic fraction decreases till it has completely vanished for pressures above 17.6 GPa. Quantative analysis of the phase compositions and lattice parameters are listed in Table 5.4.

The sample at 38 GPa only shows the characteristic XRD spectra of the ortho-II phase. Unfortunately these high-pressure spectra have only moderate resolution, but the main bands are well resolved. The strongest peak at $\sim 10.5°$ corresponds to an overlap of the $[102]_{oII}$ and $[200]_{oII}$ reflection, and the band next to it belongs to the $[111]_{oII}$ reflections. With increasing pressure (up to 70 GPa), the ortho-II phase is maintained, only the lattice parameters shrink under this tremendous stress, merging the reflection bands further together. Fig. 5.20 shows the computed total energy versus the volume in the three discussed structures [125]. At ambient pressure, the sample volume is not compressed and the monoclinic structure ($P2_1/c$) is the energetically lowest configuration. Under compression, the volume shrinks and a transition into the ortho-I phase (Pbca) becomes energetically most favorable. As one can see from Fig. 5.20, the minima of the energy curves of the monoclinic and ortho-I structure are very close, explaining the sluggish nature of the transition between these two phases. For further compression, the ortho-II offers the lowest energy configuration.

For two pressures (10.0 and 22.1 GPa), the samples were quenched and the remaining structure analyzed. The results are shown on the right-hand side of Fig. 5.6. Both quenched samples are predominantly monoclinic with some residues of the ortho-I phase (indicated by the peak at 9.6°), which is about 10 % for the sample quenched from 10.0 GPa and $\sim$ 15 % for the sample quenched from 22.1 GPa. In

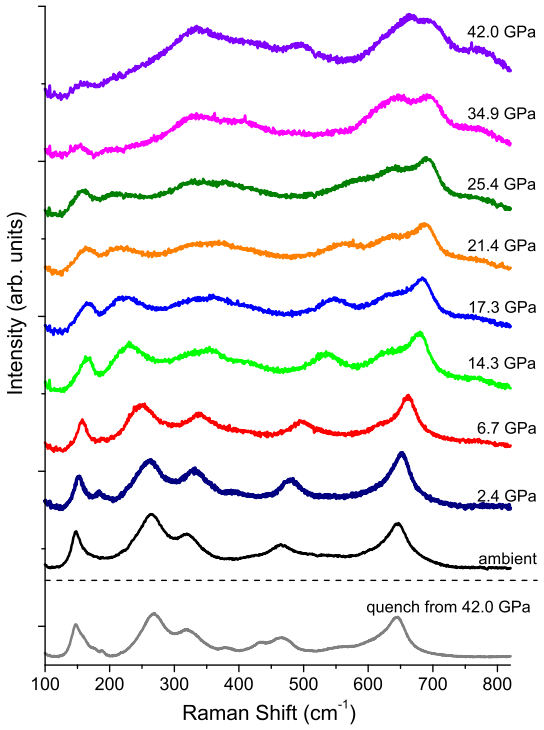

Figure 5.21: Raman spectra of irradiated ZrO_2 (5×10^{12} Pb-ions/cm^2) at various pressures. The grey (bottom) spectrum shows the sample quenched from 42.0 GPa.

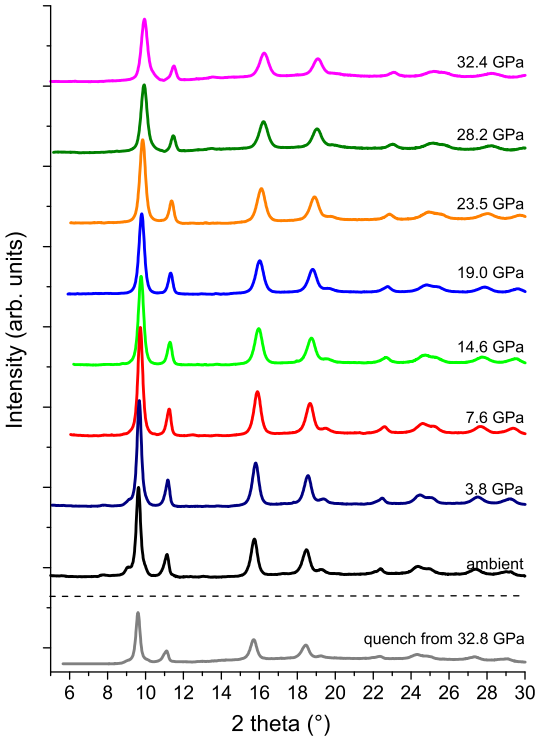

Figure 5.22: X-ray diffraction spectra of irradiated ZrO_2 (5×10^{12} Pb-ions/cm^2) at various pressures. The grey (bottom) spectrum shows the sample quenched from 32.4 GPa.

conclusion, we can say that Raman as well as X-ray analysis prove that samples quenched from pressures as high as 24 GPa always change back into the monoclinic phase.

5.1.9 Pressure dependence of irradiated ZrO_2

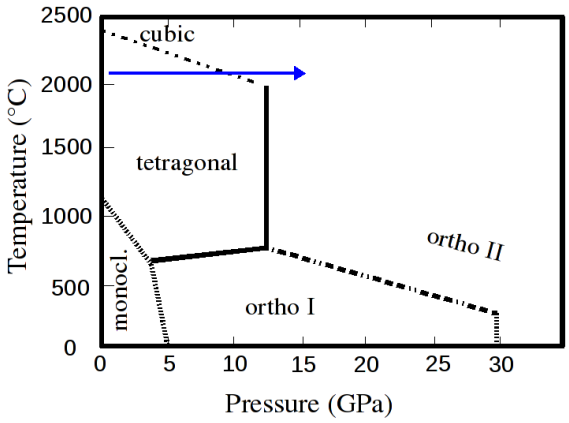

Figure 5.23: Phase diagram of ZrO_2 after [117]. The arrow indicates the possible transition route for an irradiated sample

So far, the pressure behavior of pristine ZrO_2 has been described, now the pressure behavior of already irradiated material will be discussed. For this study, a sample irradiated with 5×10^{12} Pb-ions/cm^2 was filled into a pressure cell and compressed up to 40 GPa for Raman and 32 GPa for X-ray measurements respectively. As mentioned in previous chapters, irradiated ZrO_2 exists in its tetragonal structure, and therefore the transition route is completely different compared to monoclinic ZrO_2. Pressure experiments on stabilized or nano-crystalline (size $<$ 15 nm) tetragonal ZrO_2 have been performed by some groups [118, 115, 186, 157], and it has been suggested that the initial structure transforms into the cubic modification under pressure

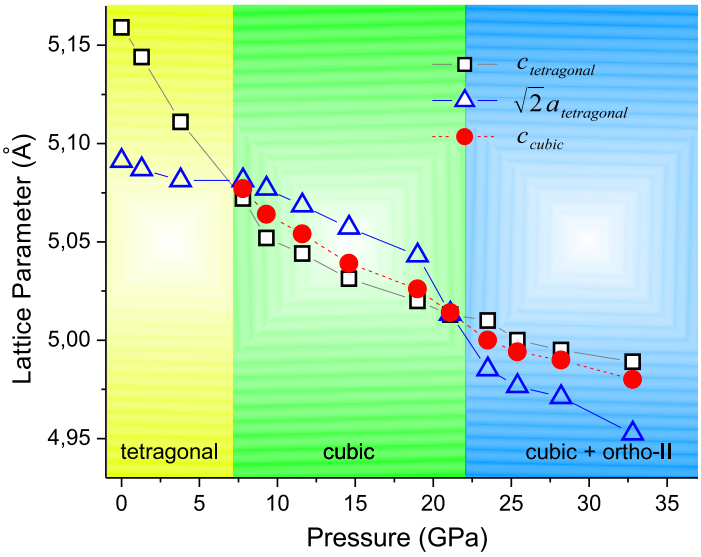

Figure 5.24: Refined lattice parameters of irradiated, tetragonal ZrO_2 up to pressures of 32 GPa.

before changing into the highest-pressure structure orthorhombic-II. Figure 5.21 shows the Raman spectra of a pressure series on irradiated ZrO_2. In the tetragonal structure of ZrO_2, six atoms are localized in the primitive cell, two Zr atoms and four O atoms, which occupy tetrahedral sites centered on the Zr atoms [115]. It exhibits six different Raman modes at 148, 265, 319, 465, 602, and 640 cm^{-1}. With increasing pressure, all lines except the one at 265 cm^{-1} shift to higher wavenumbers. Above 6 GPa, a shoulder arises at 620 cm^{-1} which increases with increasing pressure. This wavenumber position is usually attributed to the cubic structure. At pressures above 25 GPa, there is a noticeable loss of Raman intensity, and the spectra have their most dominant line at around 700 cm^{-1} indicating a second phase change. After quenching the irradiated sample from 42 GPa, it is tetragonal again.
More information can be obtained by the X-ray analysis of the sample shown in Fig. 5.22. The lattice parameters of the irradiated sample at ambient pressure were refined to $a = b = 3.593$ Å and $c = 5.159$ Å. As mentioned earlier, it is very difficult to distinguish the two high-temperature structures since the tetragonal phase is only slightly distorted from the cubic structure [157]. The only difference is the splitting of related diffraction peaks at $\sim 11°$ and 18°. Because of the broadening of the peaks due to strain induced by radiation and additionally by pressure, it is difficult to determine whether the tetragonal phase has transformed to the cubic one. The deviation from the ideal cubic arrangement can be described via the tetragonal distortion A of the cell parameters [186]:

$$A = \frac{c}{a\sqrt{2}} \tag{5.10}$$

The cubic structure is characterized when A becomes equal to one. All observed patterns were refined for the tetragonal as well as the cubic structure, which both fit well onto the measurements. Fig. 5.24 shows the refined lattice parameters of c and $\sqrt{2}a$ of the tetragonal phase and c of the cubic structure. With increasing pressure, c and $\sqrt{2}a$ become almost the same, indicating that the sample changes into the cubic structure. Zhang et al. [157] observed the same behavior for nano-crystalline, tetragonal

Pressure (GPa)	a_{tetra} (Å)	c_{tetra} (Å)	c_{cubic} (Å)
0	3.606	5.159	
1.3	3.597	5.144	
3.8	3.593	5.111	
7.8	3.593	5.072	5.077
9.3	3.590	5.052	5.064
11.6	3.584	5.044	5.054
14.6	3.576	5.031	5.039
19.0	3.566	5.020	5.026
21.1	3.545	5.013	5.014
23.5	3.525	5.010	5.001
25.4	3.519	5.000	4.994
28.2	3.515	4.995	4.989
32.8	3.502	4.989	4.980

Table 5.5: Refined lattice parameter for tetragonal as well as cubic structure of ZrO_2 irradiated with 5×10^{12} Pb-ions/cm^2.

ZrO_2. They observed a pressure induced transition from tetragonal to cubic at around 10 GPa. Here the transition occurs at a pressure of already 7 GPa indicated by the crossing of the lattice parameters for c and $\sqrt{2}a$. From 7 GPa on, also the cubic lattice parameters are plotted in Fig. 5.24. It seems that the radiation-induced, tetragonal ZrO_2 lowers the needed energy input (in the form of pressure) by several GPa for the transition from tetragonal to cubic. For even higher pressures, a second discontinuity occurs at around 22 GPa which might be due to a second transition into the orthorhombic-II structure. This agrees with the new small bump in the XRD spectra appearing around 14° above 30 GPa which belongs to the ortho-II phase (compare Fig. 5.19). Since this transition is of reconstructive type, which requires nucleation and growth of the new phase, it is very sluggish and far from completion at 32 GPa. The transition follows the path indicated by the arrow in Fig. 5.23. Highly irradiated ZrO_2 behaves like a sample above 2000 °C. Under compression it changes first into the denser ($\Delta\rho \cong 0.2$ g/cm^3) cubic before slowly changing into the ortho-II phase.

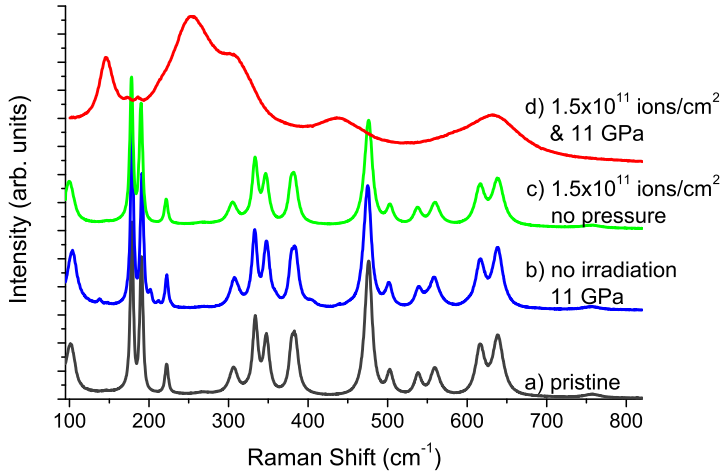

Figure 5.25: Raman spectra at ambient conditions of different ZrO_2 samples: (a) pristine, (b) pressurized without irradiation, (c) irradiated with 1.5×10^{11} U-ions/cm^2 but without pressure, (d) irradiated with 1.5×10^{11} U-ions/cm^2 at a pressure of (11.0 $\pm$ 0.3) GPa.

5.2 Irradiations under high pressure

To this point, the response of ZrO_2 to either irradiation or pressure alone has been described. By the relatively new experimental approach of combining ion irradiation with high-pressure, the behavior under two simultaneously existing, extreme conditions can be studied. Pressure applied during irradiation not only opens access to a large variety of structural conformations of the starting material but also allows new routes for phase transitions within the $p-T$ phase diagram. Additional pressure was shown to enhance or hinder certain radiation induced transformations [8, 187]. Conversely, ion irradiation can change the stability field of some materials [105, 106]. The exposure of pressurized samples to ion beams also provides insight into how pressure-induced phase transitions in minerals may be affected by pre-existing damage and by the microstructure of the starting material. Recent results also demonstrated that new structural phases may become accessible for analysis at ambient conditions [8].

Surprisingly, samples irradiated under high pressure and analyzed after pressure release show quite different results compared to specimens irradiated at ambient pressure conditions. First experiments in this work were performed with rather low ion fluences in the regime of a few 10^{11} ions/cm^2 with Au and U ions. In this fluence regime, no radiation damage could be observed at ambient pressure. ZrO_2 powder was mounted in a diamond anvil cell and hydrostatically compressed to a pressure of (11 $\pm$ 0.1) GPa. While pressurized, it was exposed to a fluence of 1.5×10^{11} U-ions/cm^2. Afterwards, the pressure was released, and the sample was carefully analyzed with Raman spectroscopy by measuring numerous different sample locations (mapping). The result is plotted together with the radiation and pressure references in Fig. 5.25. The upper curve shows that this sample underwent a staggering change only when exposed to high pressure and ion irradiation at the same time. We can see that a transformation to the tetragonal form has occurred. This is in clear contrast to the unpressurized reference sample, irradiated under the same conditions (Fig. 5.25(c)), which shows no deviation from a pristine sample

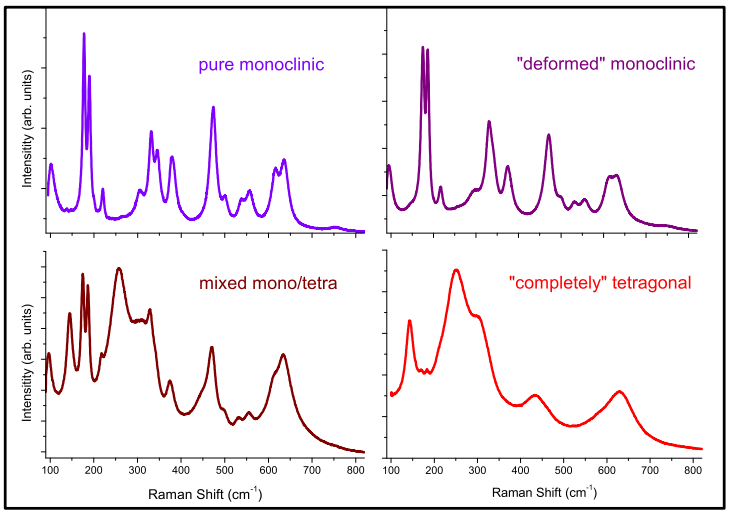

Figure 5.26: Raman spectra measured at ambient pressure of ZrO_2 irradiated with 2.5×10^{12} Au-ions/cm^2 under 10.9 GPa. The spectra show four different positions of the same sample each exhibiting a different degree of the phase transition.

at such low fluences. In transformed regions, the tetragonal fraction is 85.3 % as estimated by means of Eq. 5.7. Pressure alone as cause for the tetragonal fraction can be excluded, since the orthorhombic-I high-pressure phase is not quenchable as demonstrated by the unirradiated pressure reference sample (Fig. 5.25 (b)), which shows no significant difference towards the pristine sample, besides some small residues around 200 cm^{-1}.

It should be mentioned, that only some regions of the sample exhibit this strong change into the tetragonal phase, whereas other regions show no change at all [106]. Fig. 5.26 displays four examples of the local variations in the Raman spectra. Most regions show pure monoclinic ZrO_2, others a mixture of monoclinic and tetragonal in different concentrations and some areas are completely transformed like after ion irradiation with 1×10^{13} U-ions/cm^2. In total, the fraction of completely transformed regions is $\sim$ 10 %. This corresponds well to an area damaged by single ion hits at a fluence of 1.5×10^{11} U-ions/cm^2 assuming a track radius of 5.3 nm. Ion irradiation under pressure obviously allows a single ion impact to induce the phase transition. This experiment has been repeated with 2.5×10^{11} Au-ions/cm^2 which resulted in the same behavior.

In sections 5.1.4 and 5.1.5, the double-impact mechanism for the radiation induced monoclinic $\rightarrow$ tetragonal transformation has been discussed. Multiple damage overlap is necessary for the transformation process: first, a pre-damaging by the creation of vacancies and the therefore resulting strain on the sample, plus the second impact invoking the phase change. This might be an explanation for the pressure enhanced radiation response. The pressure additionally applied on the irradiated sample also induced large strain, that might be enough to take over the step usually performed by the first ion impact. Then, already one ion hit suffices to provoke a relaxing transformation into the denser high-temperature polymorph. To clarify this hypothesis, irradiation experiments of pressurized samples were performed with a fluence of which one can assume that the entire sample area has been hit just once. Therefore, ZrO_2 was pressurized to (10.3 $\pm$ 0.3) GPa and exposed to a fluence of 2×10^{12} U-ions/cm^2. Raman scans over

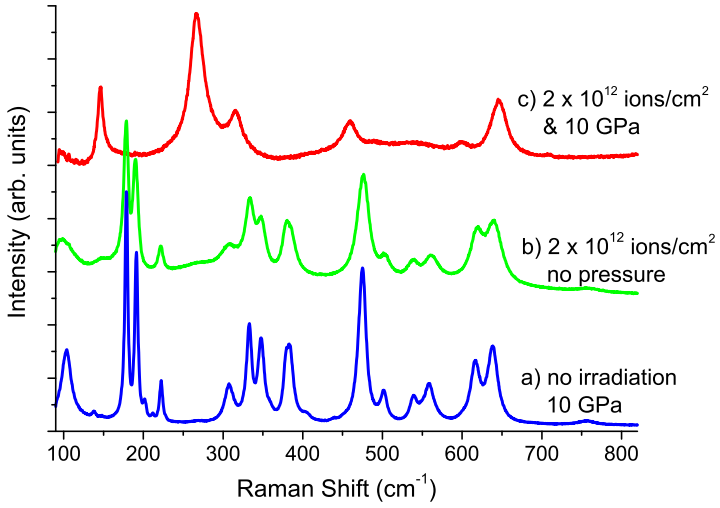

Figure 5.27: Raman spectra at ambient conditions of different ZrO_2 samples: (a) pressurized to 10.5 GPa but not irradiated, (b) irradiated with 2×10^{12} U-ions/cm^2 but without pressure, (c) irradiated with 2×10^{12} U-ions/cm^2 under pressure of (10.3 $\pm$ 0.3) GPa.

the whole sample have been performed. Again, one finds enhanced radiation response due to additional pressure. Homogeneously, each measured position yields Raman spectra as shown in Fig. 5.27(c). Obviously, the whole sample has changed into the tetragonal structure already at a fluence which normally does not suffice to induce this transformation at ambient pressure (see Fig. 5.27(b)). After irradiation of 2×10^{12} U-ions/cm^2, one can estimate roughly that one complete layer of pre-damaged material exists. But this alone, without pressure, would not have been enough to induce a phase change. Statistically, some areas might have been hit twice already. This is why the Raman spectra show the beginning of a transition in the reference sample. From Fig. 5.11, one can conclude that only $\sim$ 10 % of the sample have transformed, whereas the sample irradiated under pressure has completely changed. It is obvious that under pressure the monoclinic $\rightarrow$ tetragonal phase transformation is induced by a single ion rather than requiring a multiple hit process.

Additional information about the transformation mechanism can be gained by the investigation of the ZrO_2 sample irradiated with 2×10^{12} U-ions/cm^2 by analyzing the material while still being pressurized. Figure 5.28 shows the diffraction spectra of pristine, pressurized, and irradiated samples inside the DAC before and after quenching. At ambient pressure, the sample is in its monoclinic phase (Fig. 5.28 (a)). Under pressure of 10.3 GPa, it changes to the high-pressure orthorhombic-I phase, clearly visible by the $[211]_o$ reflex at 9.70 $^\circ$ (Fig. 5.28 (b)). The transition is not completed, and about 38 % of the sample remain in the monoclinic phase, indicated by the $[\text{-}111]_m$ and $[111]_m$ reflexes. If the sample rests at this pressure for one week and is then quenched to ambient pressure, it changes back to the monoclinic structure (Fig. 5.28 (c)) with a contribution of about 10 % of the orthorhombic phase. The situation is very different for the sample irradiated under a pressure of 10 GPa. Instead of the monoclinic or tetragonal structure, we find the second high-temperature cubic phase of ZrO_2 evidenced by the $[111]_c$ reflection at 9.72 $^\circ$, $[200]_c$ reflection at 11.17 $^\circ$, and $[220]_c$ reflection at 15.90 $^\circ$ (Fig. 5.28 (d)).

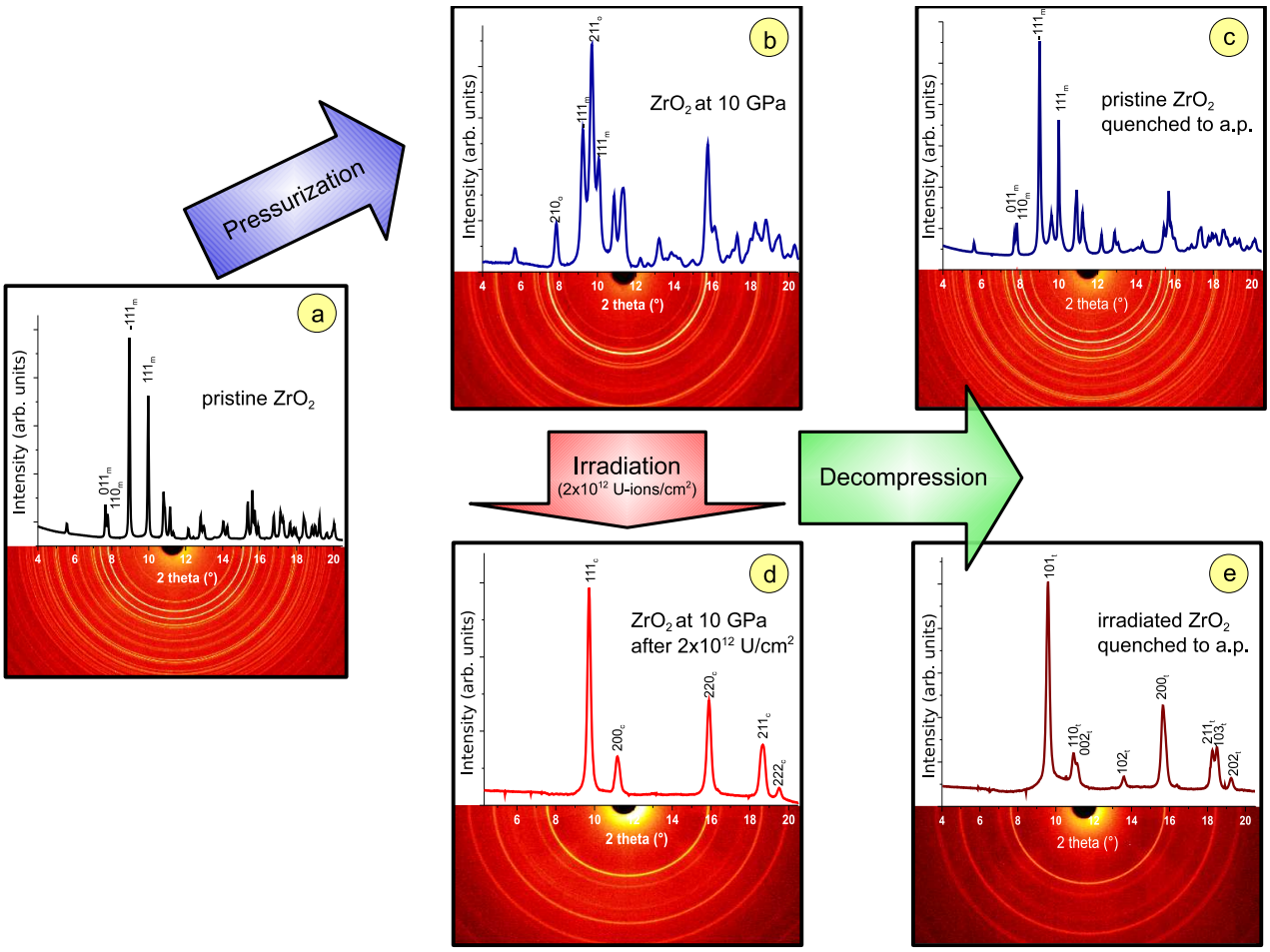

Figure 5.28: X-ray diffraction spectra of different stages of the experiment. At ambient conditions ZrO_2 shows peaks of the monoclinic structure (a). Pressurized to 10 GPa, new reflexes which belong to the ortho-I phase appear as a mixture of monoclinic/ortho-I (b). Additional irradiation with 2×10^{12} U-ions/cm^2 provokes a transformation into the cubic phase (d). When releasing the pressure, the unirradiated sample transforms back into its monoclinic form (c), whereas the irradiated sample transforms into the tetragonal structure and remains stable in this phase also at ambient pressure (e).

Rietveld refinement yields a lattice constant of $c = (5.072 \pm 0.002)$ Å. This stage could not be derived from the Raman data recorded at ambient pressure (see Fig. 5.27).

Surprisingly, during the pressure release the material neither stays cubic nor changes into the expected ambient monoclinic, but instead transforms into the tetragonal structure. This XRD result is in agreement with our observation by means of Raman spectroscopy at ambient pressure. When releasing the pressure, the cubic peak at 11.17 ° splits into two individual peaks belonging to the $[110]_t$ reflection at 10.94 ° and the $[002]_t$ reflection at 11.13 ° of the tetragonal phase. Similar splittings can be observed at larger diffraction angles, e.g. $[211]_t$ and $[103]_3$ reflections around $\sim$ 18.5 °. Also the $[102]_t$ reflection appearing at 13.57 ° is a clear indication of the tetragonal phase. During decompression, the cubic phase remains stable down to $\sim$ 3 GPa and then undergoes a sudden change into the tetragonal phase within the last decompression step [188].

There are a number of different possible explanations for this pressure enhanced radiation effect at low fluences. Firstly, a temperature effect due to the lowered transition boundary between ortho-I and tetragonal phase at elevated pressure. Secondly, a possible energy loss increase due to higher density of the pressurized material. And thirdly, the effect of pressure induced strain within the sample. With increasing pressure the temperature necessary for the monoclinic → tetragonal transition decreases from ∼ 1000 to ∼ 600 °C (see Fig. 5.2) at around 4 GPa. This means that above 4 GPa less energy in form of heat is needed to produce the tetragonal form. However, this can still not explain the existence of this phase at room temperature since the tetragonal phase would return to monoclinic once the temperature rise due to irradiation has thermalized. To further elucidate, the same experiment for the 1.5×10^{11} U-ions/cm^2 irradiation has been performed for pressures of 4.6, 7.6, 11.0, and 13.6 GPa (see Fig. 5.29). Here the transformation degree also varies with the sample position, so only the regions with the highest degree of transformation are displayed. The irradiation at 4.3 GPa created no enhanced radiation effect. The sample irradiated at 7.6 GPa shows signs of a beginning transformation, similar to an irradiation after a fluence of 10^{12} ions/cm^2. Above 11 GPa the transformation is completed. We can thus assume that temperature is not the driving force behind the strong transformation behavior since effect shows up at these low fluences only for higher pressures.

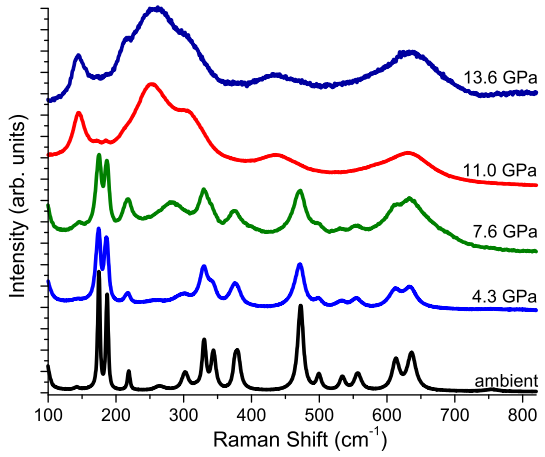

Figure 5.29: Raman spectra of the regions of ZrO_2 with highest degree of transformation that were irradiated with 1×10^{11} U-ions/cm^2 under various pressures.

Another effect might be an higher electronic energy loss in pressurized sample. As mentioned earlier, the irradiations of pressurized and pristine material are quite different since we start with the denser orthorhombic-I phase. At ambient conditions, ZrO_2 has a density of 5.70 g/cm^3. Via Rietveld refinement we determined the density of ZrO_2 at 10 GPa to be (6.04 ± 0.13) g/cm^3. The small density increase changes the electronic energy loss of U-ions in ZrO_2 only slightly from 37.3 to 39.3 keV/nm at an energy of 30 MeV/u. A density effect can therefore also be ruled out as possible influence, since the small energy loss difference of 2.2 keV/nm can be neglected considering that the ambient pressure experiment performed at the UNILAC provided an energy loss of 53.2 kev/nm [22] and did not reveal any phase transition for fluences ≤ 2×10^{12} ions/cm^2.

To summarize, the externally applied pressure provides internal stress in the sample, taking over the part of the first step of the ion impacts. We assume that with increasing pressure the strain field increases, explaining why at lower pressures the samples irradiated with low fluence did not transform into the tetragonal phase.

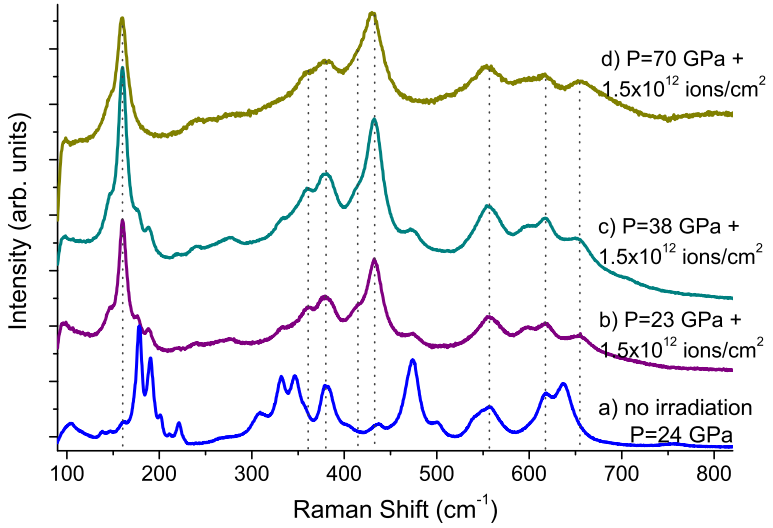

Figure 5.30: Raman analysis at ambient pressure of ZrO_2 irradiated with 1.5×10^{12} U-ions/cm^2 at 23 GPa (b), 38 GPa (c), and 70 GPa (d). Additionally, a pressure reference (pristine ZrO_2 quenched from 24 GPa (a)) is displayed.

5.2.1 Irradiations at very high pressures

To this point, high-pressure irradiations up to 11 GPa under hydrostatic conditions were discussed. For pressures up to 12.5 GPa, the temperature path comprises a transition from monoclinic → tetragonal → cubic (see Fig. 5.2). If ZrO_2 is irradiated at higher pressures (> 20 GPa) the previously discussed transition path is no longer possible. Therefore, additional experiments combining pressure and irradiation were performed at extreme pressures of 23, 38 and 70 GPa. The sample at 23 GPa is before the irradiation in the orthorhombic-I phase, while the samples at 38, and 70 GPa are well within the stability field of the second high-pressure phase orthorhombic-II. Starting at the orthorhombic-II phase, the beam-induced transformation route from monoclinic → tetragonal → cubic cannot occur (see Fig. 5.2). Outside the DAC, we recorded the Raman spectra of the samples which were irradiated under pressure with 1.5×10^{12} ions/cm^2 (Fig. 5.30). Most interestingly, after quenching the samples irradiated at 23 GPa consists predominantly of the orthorhombic-II phase (small monoclinic residues exist at 178 and 190 cm^{-1}, but the fraction is low). The bands of the orthorhombic-II phase are highlighted by dotted lines in Fig. 5.30 (b). The strongest peaks of this structure are located at 160 and 432 cm^{-1}, in agreement with earlier observations (see Fig. 5.18) and literature data where ZrO_2 was quenched from 40 and 60 GPa [112, 121]. The finding of the orthorhombic-II

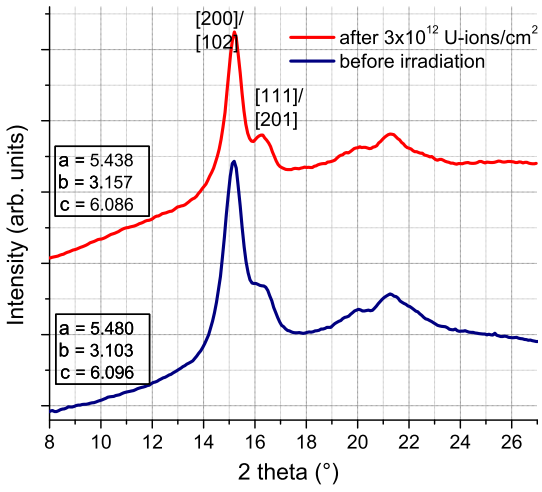

Figure 5.31: X-ray diffraction patterns of ZrO_2 at 70 GPa before and after irradiation with 3×10^{12} U-ions/cm^2 (λ = 0.7108 Å).

Ion	E_{init} (GeV)	dE/dx (keV/nm)	Fluence Φ (ions/cm^2)	Pressure (GPa)	Initial structure	Final structure
macro-crystalline ZrO_2						
^{238}U	7.14	39	1.5×10^{11}	11.0 ± 0.3	ortho-I	strong tetragonal regions
^{238}U	7.14	37	1.5×10^{11}	ambient	mono	mono
^{238}U	7.14	39	2.0×10^{12}	10.3 ± 0.3	ortho-I	cubic (10.3 GPa), tetragonal (ambient)
^{238}U	7.14	37	2.0×10^{12}	ambient	mono	mono
^{238}U	7.14	≥ 39	1.5×10^{12}	23 ± 1.0	ortho-I	ortho-II
^{238}U	7.14	≥ 39	1.5×10^{12}	38 ± 2.0	ortho-II	ortho-II
^{238}U	7.14	≥ 39	1.5×10^{12}	70 ± 4.0	ortho-II	ortho-II
^{238}U	7.14	≥ 39	3.0×10^{12}	70 ± 4.0	ortho-II	ortho-II
nano-crystalline ZrO_2						
^{238}U	7.14	39	2.0×10^{12}	10.5 ± 0.3	ortho-I	cubic (10.5 GPa), tetragonal (ambient)
non-hydrostatic conditions						
^{238}U	7.14	39	2.0×10^{12}	10.9 ± 0.8	ortho-I	cubic (10.9 GPa), monoclinic (ambient)
^{208}Pb	7.14	39	3.0×10^{12}	11.0 ± 1.0	ortho-I	cubic (11.0 GPa), monoclinic (ambient)

Table 5.6: Irradiation and pressure parameters for all samples irradiated at the SIS under high pressure. The table summarizes the crystalline structures before and after irradiation, as determined at ambient conditions.

phase is surprising because, at 23.1 GPa, ZrO_2 exists in its first high-pressure polymorph orthorhombic-I and is still ∼ 7 GPa away from the transition boundary to the orthorhombic-II phase. Irradiation with swift heavy ions obviously triggers the creation of this phase at a significantly lower pressure. Once produced, the orthorhombic-II phase is quenchable to ambient pressures. Pressure alone as cause for the transformation into the orthorhombic-II phase was excluded by quenching a reference sample from 24 GPa, which did not show any orthorhombic-II signal (see Fig. 5.30 (a)) even after one week. For pressures larger than ∼ 20 GPa, orthorhombic-II is the only possible high-temperature structure (see Fig. 5.23). It cannot be distinguished whether the ion-beam induced transition proceeds via the temperature or the pressure route.

Samples pressurized to 38 or 70 GPa are in the orthorhombic-II phase. Having no neighboring phase boundary, it is not surprising that the initial orthorhombic-II structure is preserved after irradiation (see Fig. 5.30 (c and d)). Due to the high bulk modulus of the orthorhombic-II structure (≥ 300 GPa [13]) and the characteristic of ZrO_2, it is considered as a good candidate for a new superhard material [13]. The radiation stability of the ortho-II phase was tested again with a doubled fluence of 3×10^{12} U-ions/cm^2 at 70 GPa. Fig. 5.31 shows the X-ray diffraction patterns of ZrO_2 recorded at 70 GPa before and after irradiation. No change can be observed. Due to the high pressure, the bands are very broad which makes it difficult to distinguish single peaks, but the crystalline structure remains ortho-II indicated by the strongest reflections [200] at 15.2° and [111] at 16.4°. The crystal structure parameters are very similar and no enhanced strain was measured. Since a fluence of 3×10^{12} U-ions/cm^2 has no influence on the orthorhombic-II structure, this high-pressure polymorph might be better suited for applications than the ambient pressure polymorphs.

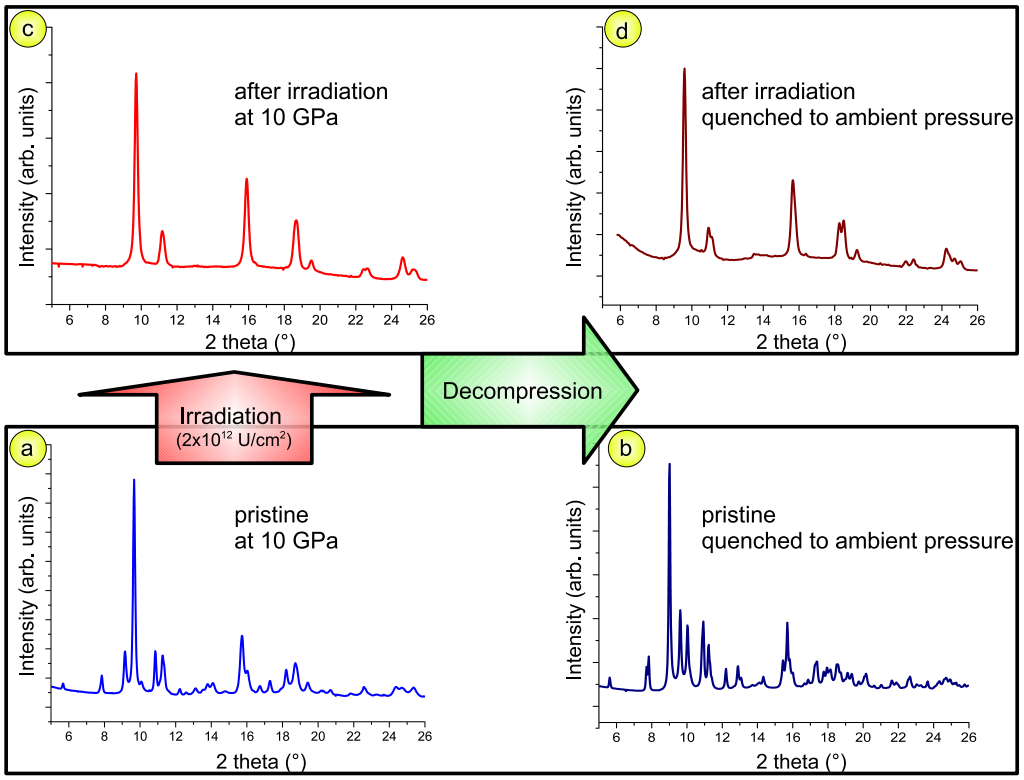

Figure 5.32: X-ray diffraction spectra of nano-cystalline ZrO_2 at different stages of the experiment. Pressurized to 10 GPa, the sample exist in a mixture of monoclinic and ortho-I (a). Additional irradiation with 2×10^{12} U-ions/cm^2 provokes a transformation into the cubic phase (c). When releasing the pressure, the unirradiated sample transforms back into its monoclinic form (b), whereas the irradiated sample transforms into the tetragonal structure and remains stable in this phase ambient also at pressure (d). This behavior is like for macro-crystalline ZrO_2.

5.2.2 Nano-crystalline ZrO_2 irradiated under pressure

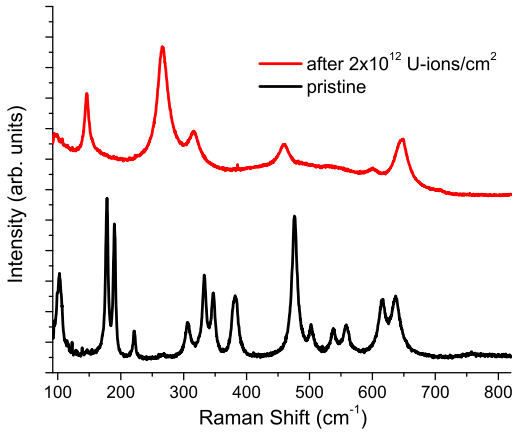

Figure 5.33: Raman spectra of nano-crystalline ZrO_2 quenched from 10 GPa after irradiation with 2×10^{12} U-ions/cm^2.

As already shown in section 5.1.7, at ambient pressure nano-crystalline ZrO_2 behaved in a similar way as macro-crystalline ZrO_2. Further, the effect of the crystal size on the radiation response of ZrO_2 under pressure has been investigated. For this purpose, ZrO_2 with an average grain size of $\sim$ 20 nm was hydrostatically loaded in a DAC and pressurized up to 10.5 GPa. At this pressure it was exposed to 2×10^{12} U-ions/cm^2. Figure 5.32 shows the development of the structural phases after the different experimental steps.

At 10.5 GPa, nano-crystalline ZrO_2 is mainly (80 %) in the ortho-I phase. After irradiation, the sample most likely changed into the cubic structure with lattice constant $c = (5.072 \pm 0.006)$ nm. When releasing the pressure from the unirradiated sample, it changes back into

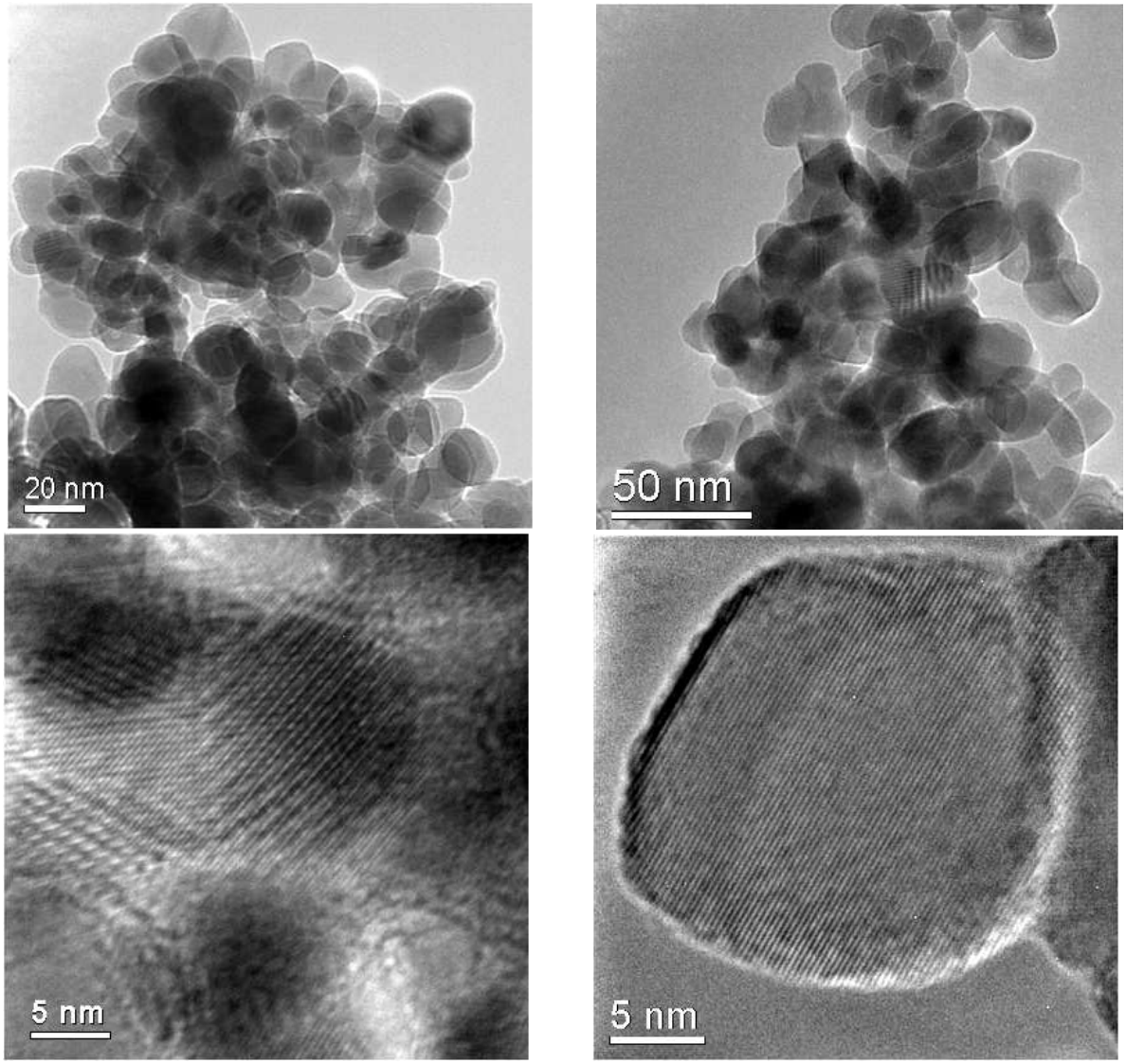

Figure 5.34: Left: TEM images of pristine nano-crystalline ZrO_2. Right: TEM images of quenched ZrO_2 after irradiation with 2×10^{12} U-ions/cm^2 at 10.5 GPa.

the monoclinic form (about 20 % remain orthorhombic immediately after the quenching). The irradiated sample on the other hand transforms into the tetragonal form as can be seen by the splitting of the bands at about 11° and 18.5°. The lattice parameters of the quenched tetragonal phase are $a = (3.641 \pm 0.006)$ nm and $c = (5.262 \pm 0.01)$. Raman analysis outside the DAC also confirmed the existence of the tetragonal phase (see Fig. 5.33). The transition is actually completed, no residues of the monoclinic structure are detectable. Even a small peak around 620 cm^{-1} is visible which might indicate remains of the cubic structure inside the quenched sample. Nano-crystalline ZrO_2 follows the same transition path as a macro-crystalline sample, from ortho-I-to-cubic at 10 GPa and then from cubic-to-tetragonal under decompression. It seems that the transition is a bit stronger in the nano-crystalline sample, which might be due to the fact that the pressure induced stress can act on a larger surface area relative to macro-crystalline ZrO_2. Also electron microscopy investigations of the quenched, irradiated material have been performed and compared to pristine nano-ZrO_2. The left side of Fig. 5.34 shows the pristine sample and the right side the irradiated one. Under the lower magnification, one can see that the grain size

did not change during irradiation under pressure. On average, it is still around 20 nm. From the highly magnified image one can see that the pristine sample shows a much more complex structure due to the tilted β angle of the monoclinic phase. The irradiated sample shows a nice even structure which could be cubic or tetragonal in this case. In conclusion one can say that the effect of grain size down to $\sim$ 20 nm can be neglected in the radiation response behavior of ZrO_2 for irradiations under pressure.

5.2.3 Irradiations under non-hydrostatic pressure conditions

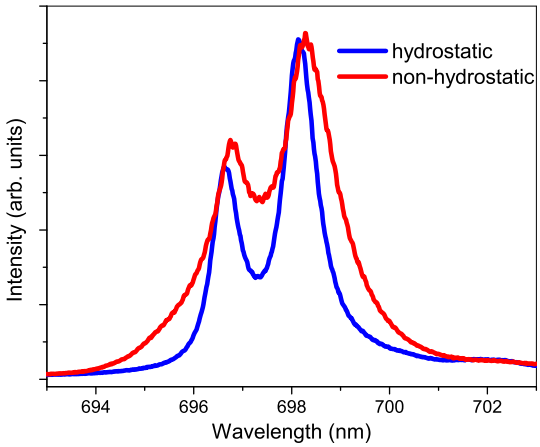

Figure 5.35: Ruby luminescence signal at around 11 GPa for hydrostatic (blue) and non-hydrostatic pressure conditions (red).

Up to this point, all experiments were performed under hydrostatic pressure conditions, although one can no longer speak of hydrostatic conditions above 11 GPa since the pressure transmitting medium (made of an alcohol mixture) solidifies. The onset of non-hydrostatic conditions in alcohol is associated with a glass transition [189]. Nevertheless the sample is sourrounded by a material. Upon pressure release the pressure medium becomes liquid again and the quenched sample is always retained in its powdery form. Pre-experiments [190] showed that strong non-hydrostatic pressure conditions can have a huge influence on the radiation response of the material. In the following experiments, ZrO_2 powder was mounted without any pressure medium inside a DAC. This means that the sample chamber was completely filled with powder without any space left in between. Under compression, the pressure was therefore exerted directly onto the sample along one direction, squeezing the powder sample together. The process is comparable to mechanical pressing of pills. In this case the conditions are highly non-hydrostatic. A typical sign of non-hydrostatic conditions is the broadening of Raman and X-ray diffraction lines. The prime indication of non-hydrostatic conditions is the broadening of the ruby luminescence signal. Figure 5.35 shows the Ruby signal from inside a DAC at around 11 GPa. At non-hydrostatic conditions the bands broaden severely.

Figure 5.36 shows the X-ray diffraction pattern of non-hydrostatically (medium-less) compressed ZrO_2 that has been irradiated with 2×10^{12} U-ions/cm^2 at 10.9 GPa. Similar to the experiment under hydrostatic conditions, the ion irradiation forces the sample to change to the cubic structure (probably a mixture of cubic and tetragonal) with a lattice parameter of $c = (5.042 \pm 0.002)$ Å. Upon decompression down to 4 GPa, this phase remains with the lattice relaxing a bit to $c = (5.052 \pm 0.002)$ Å at 7.2 GPa and $c = (5.063 \pm 0.002)$ Å at 4.0 GPa. Interestingly, at the last decompression step to ambient pressure, the sample changes back to the monoclinic structure (54 % with $a = (5.329 \pm 0.008)$, $c = (5.333 \pm 0.006$, and $c = (5.544 \pm 0.007)$ Å, and $\beta = 99.1°$) but some part remains in the cubic phase (46 % with $c = (5.178 \pm 0.004)$ Å). Due to extreme line broadening of the quenched sample, one can assume that some part of the sample is still under internal stress. As mentioned earlier, one can compare this non-hydrostatic compression with pill pressing, by which the extreme pressure glues the ZrO_2 grains

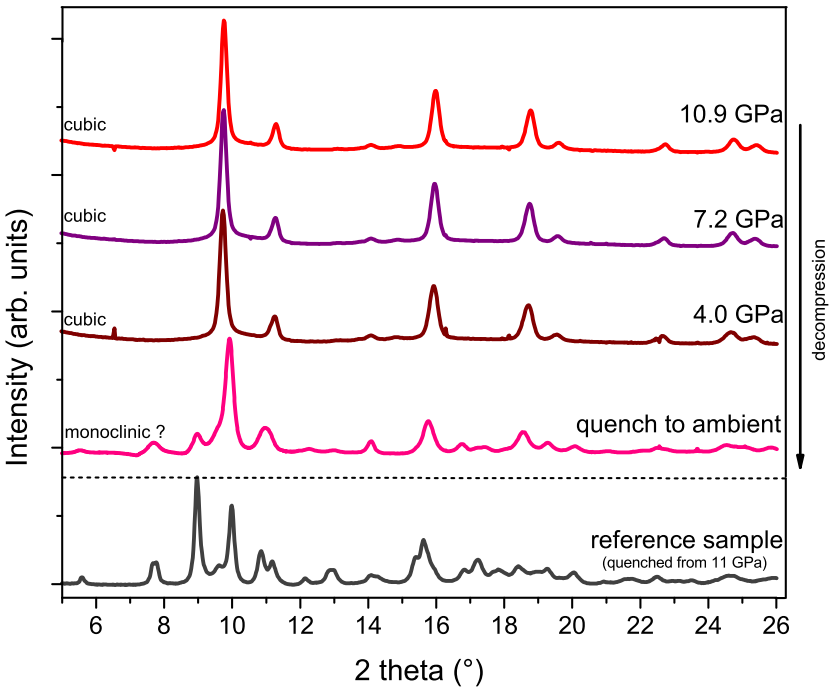

Figure 5.36: X-ray diffraction spectra of ZrO_2 irradiated with 2×10^{12} U-ions/cm^2 under non-hydrostatic conditions (10.9 GPa). The diagram shows X-ray patterns at different pressures during the decompression process.

together. Even after opening the pressure cell, the sample is one single piece and not powdery anymore. It can also not be removed from the gasket except of strong mechanical force under which it shows the brittle behavior of a crystal. This could explain the unusual XRD-signal. After pressure release, the free sides of the sample change back to the monoclinic structure clearly visible by the $[100]_m$ band at 5.52°, the merged $[011]_m$ and $[110]_m$ bands at 7.67°, and of course the strong $[-111]_m$ reflection at 8.97°. The strong peak around 10° is an overlap of the $[111]_m$ reflection of the monoclinic and the $[111]_c$ reflection of the cubic structure. Because of the high-energy X-rays, all regions of the sample contribute to the diffraction pattern. So, probably the inner part of the sample, still compressed by the sourrounding crystals, did not relax to monoclinic and therefore still shows a cubic diffraction pattern whereas the free sides did relax. But this still raises the question why it changes back at all into the monoclinic form. All previously reported experiments (see Section 5.2), performed under hydrostatic conditions, still showed a stronger enhanced radiation effect. After the same fluence and pressure the sample was completely tetragonal and did not return to the pristine monoclinic phase. To gain a better understanding of this behavior, the experiment was repeated with an in-situ Raman analysis.

Again, ZrO_2 was non-hydrostatically compressed up to 11.0 GPa and exposed to 3×10^{12} Pb-ions/cm^2. In this case, Raman analysis was performed under pressure. Fig. 5.37 shows the different experimental steps. After the irradiation the Raman signal shows a mixture of cubic and tetragonal phase. As mentioned before, these two structures are difficult to distinguish. Similar to experiments performed under hydrostatic conditions the pressure enhances the radiation effect so that the whole sample undergoes a transformation. Upon decompression the sample remains cubic/tetragonal down to 2.4 GPa. The de-

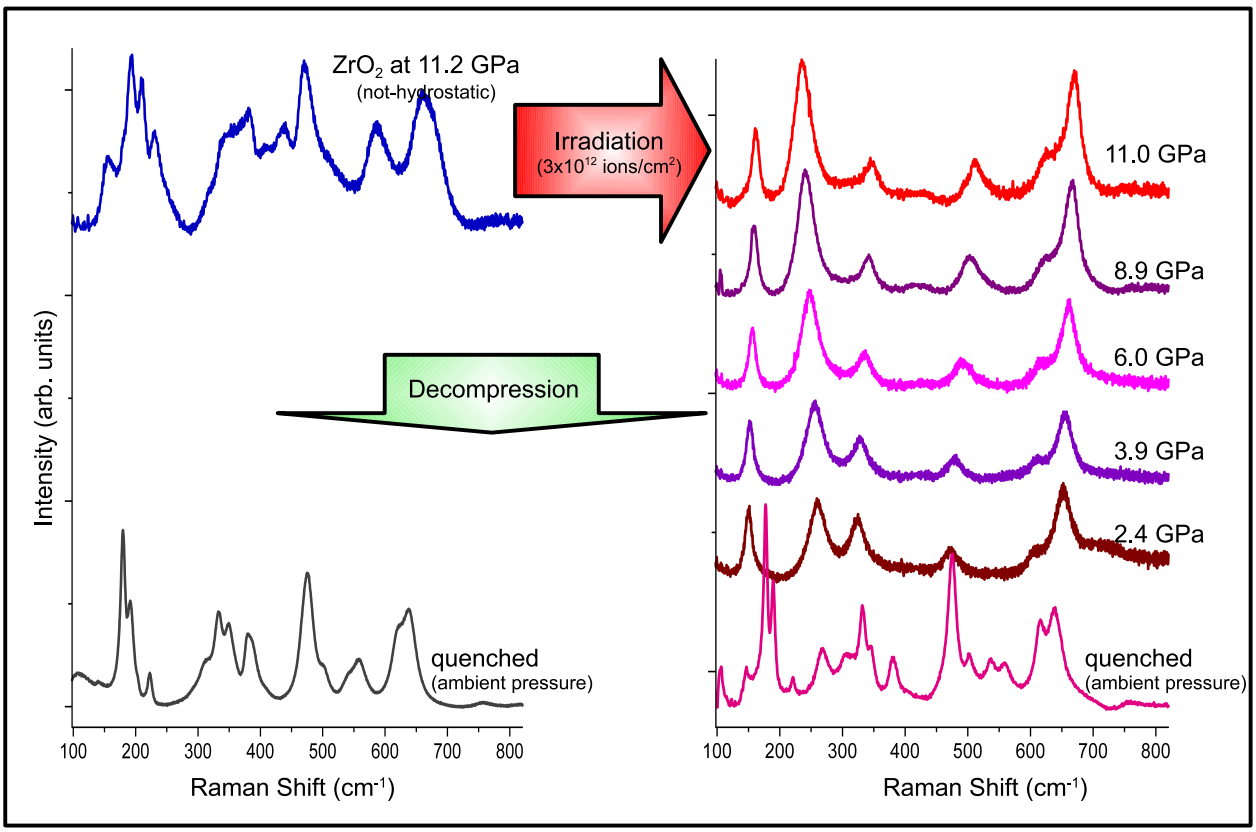

Figure 5.37: Raman spectra of ZrO_2 irradiated with 3×10^{12} Pb-ions/cm^2 under non-hydrostatic consitions at 11.0 GPa. The Figure shows the Raman spectra at different pressures during the decompression process.

compression process can be well observed by the movement of the lineshift of the different peaks. But also in this case, when the sample is quenched to ambient pressures it changes back to the monoclinic form. No indication of the previously strong transformation remains. Some signal of the tetragonal structure can be observed by the small peaks at 148 and 265 cm^{-1}. A fraction of about 12 % of the sample is tetragonal, this corresponds well to the result after an irradiation with the same fluence (3×10^{12} Pb-ions/cm^2) under ambient pressure. Obviously, non-hydrostatic pressure conditions can not preserve the enhanced radiation response down to ambient pressure. Raman spectroscopy yields the same result as X-ray diffraction. The reason why the Raman data showed no cubic/monoclinic mixture at ambient pressure in the quenched sample is due to the fact that Raman spectroscopy is only surface sensitive (penetration depth $\sim$ few μm), whereas XRD gathers information of the whole sample depth.

The question why pressure conditions have such a strong influence on the radiation response still remains unsolved. A pressure effect alone can be excluded since a reference sample compressed non-hydrostatically to 11.2 GPa and then quenched shows no phase change (see Fig. 5.37). The spectrum of the quenched non-hydrostatic sample is also monoclinic, but by means of the broad band one can clearly distinguish the pressure conditions under which the sample has been exposed to the beam. One possible explanation might be the crystalline character of the non-hydrostatically compressed sample. As mentioned before, the different grains of the sample are compressed in a way that the sample becomes one single piece. It would be wrong to describe it as a single-crystalline material, but it shows the

mechanical characteristics of one large crystal. As shown in section 4.1, for single-crystalline material the direction of the damage can play an important role. In the described experiment, the applied pressure and ion irradiation were directed along the same axis which might be disadvantageous for a strong radiation response. Possibly, irradiation of a ZrO_2 single crystal or irradiation perpendicular to the pressure direction (in the non-hydrostatic case) could shed more light onto this behavior. Unfortunately, the geometry of our experimental setup limits us to the irradiation in only one sample direction.

5.3 Hafnia (HfO_2)

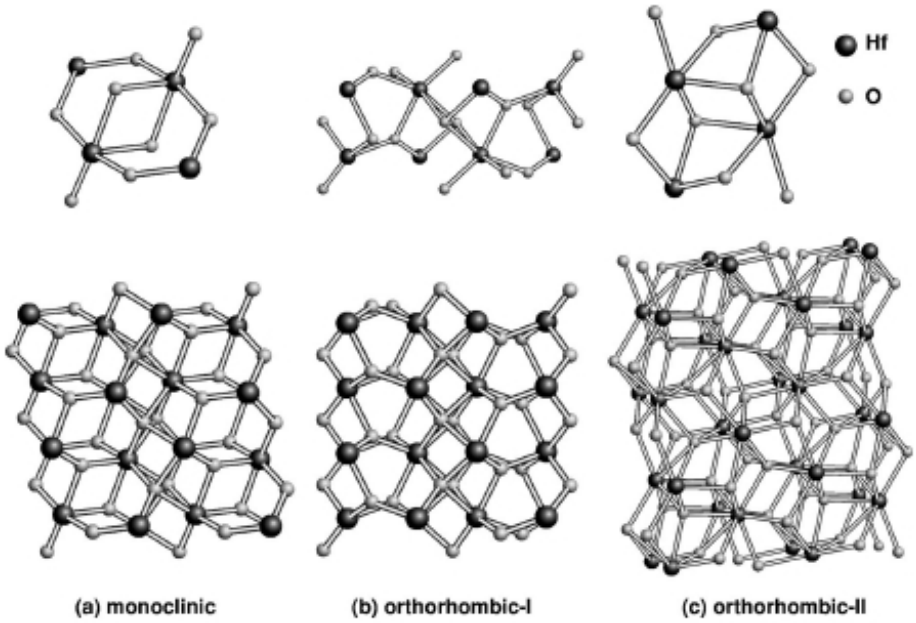

Figure 5.38: The unit cells of the ambient and high pressure crystal structures of HfO_2, i.e. monoclinic, orthorhombic-I, and orthorhombic-II. Depiction taken from [191].

Hafnia or hafnium dioxide (HfO_2) is like zirconia a ceramic material with excellent structural stability and dielectric properties and a wide range of industrial applications [192, 193]. Zr and Hf belong to the same column in the periodic table and and show a remarkable resemblance in their metal state as well as their compounds. This similarity is stronger than for any other pair of two elements [194]. This similarity is due to the so called lanthanide contraction. The main difference between these two elements in terms of the electronic structure is the f states. Hf has a closed $4f$ subshell whereas Zr has no f electrons at all. Because the weak shielding of the $4f$ electrons the atomic (1.6 Å for Zr and 1.67 Å for Hf) and ionic (0.8 Å for Zr and 0.81 Å) radii of Zr and Hf are almost identical despite the huge difference in cation mass (91.2 for Zr and 178.5 for Hf) [182]. Besides all similarities there a small differences between Zr and Hf as and their oxide compounds. For instance, Hf has a smaller electronegativity (1.16) compared to Zr (1.32), indicating a slightly stronger tendency to form ionic bonds with other more electronegative elements such as oxygen. Gutowski et al. also found that HfO_2 is more stable than ZrO_2 (i.e., it has a larger heat of formation from its constituent elements). This amounts to more than 42 kJ/mol [196]. Also the band

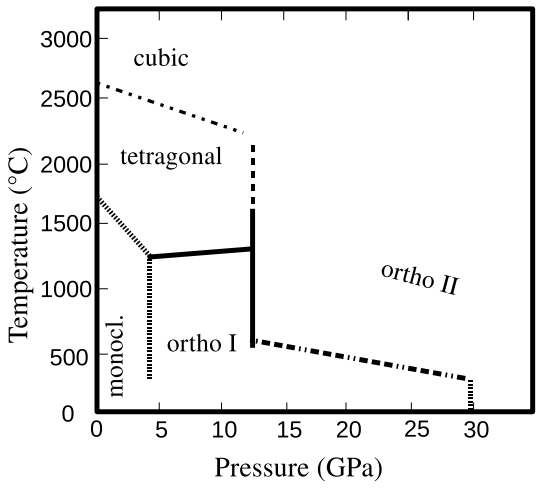

Figure 5.39: Phase diagram of HfO_2. (Modified picture from [195])

crystal structure	lattice group	lattice parameter [Å]	density [g/cm^3]
monoclinic $a \neq b \neq c$ $\alpha = \gamma = 90°$ $\beta > 90°$	$P2_1/c$	$a = 5.128$ $b = 5.191$ $c = 5.297$ $\beta = 99.3°$	9.68
tetragonal $a = b \neq c$ $\alpha = \beta = \gamma = 90°$	$P4_1/nmc$	$a = 3.578$ $c = 5.200$	~ 10.2
cubic $a = b = c$ $\alpha = \beta = \gamma = 90°$	$F_{m\bar{3}m}$	$c = 5.063$	-
orthorhombic I $a \neq b \neq c$ $\alpha = \beta = \gamma = 90°$	Pbca	$a = 10.220$ $b = 5.310$ $c = 5.080$	~ 10.1
orthorhombic II $a \neq b \neq c$ $\alpha = \beta = \gamma = 90°$	Pnma	$a = 5.553$ $b = 3.303$ $c = 6.482$	~ 11

Table 5.7: Structural data of all five solid-state phases of HfO_2 [191, 107, 113, 192, 182].

gap of HfO_2 is slightly bigger than in ZrO_2 (3.58 eV for ZrO_2 and 3.95 eV for HfO_2) [182]. But still, no other two compounds have a comparable similarity. Because of their strong chemical, physical, and thermodynamical similarities, it is very attractive to test if this resemblance can be extended to their behavior under swift heavy ion irradiation, with and without additional pressure.

5.3.1 Phase transitions in HfO_2

Like ZrO_2, HfO_2 has five different crystalline conformations (for details see Table 5.7). Besides the monoclinic phase at ambient conditions, it has two high-temperature (tetragonal and cubic) and two high-pressure (orthorhombic-I and orthorhombic-II) polymorphs. At around 1700°C, HfO_2 changes to the tetragonal, and above 2500°C to the cubic phase. Melting occurs for temperatures above 2800°C. The structural phase behavior of HfO_2 is displayed in the phase digram in Fig. 5.39.

5.3.1.1 monoclinic → orthorhombic I transition

The same pressure induced transitions as in ZrO_2 occur also in HfO_2. At pressures between 4 and 9 GPa, the transition from monoclinic to the first high-pressure phase orthorhombic-I (space group Pbca) takes place [195, 197]. This displacive transition is very sluggish at room temperature, so that up to 12 GPa residues of the monoclinic phase are still observed. The ortho-I structure of HfO_2 is not quenchable to ambient pressure.

5.3.1.2 orthorhombic I → orthorhombic II transition

For higher pressures, a transition occurs from the first orthorhombic to the second orthorhombic phase occurs. Like for ZrO_2, the stability field of this ortho-II phase begins around 30-35 GPa and extends up

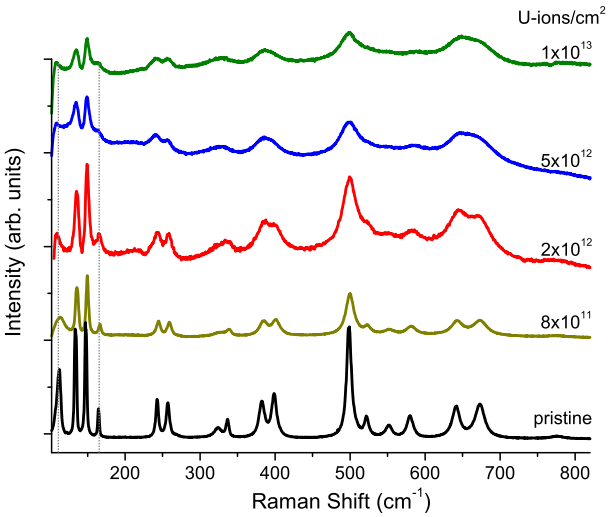

Figure 5.40: Raman spectra of HfO_2 irradiated at ambient pressure with 11.1 MeV/u U-ions for various fluences.

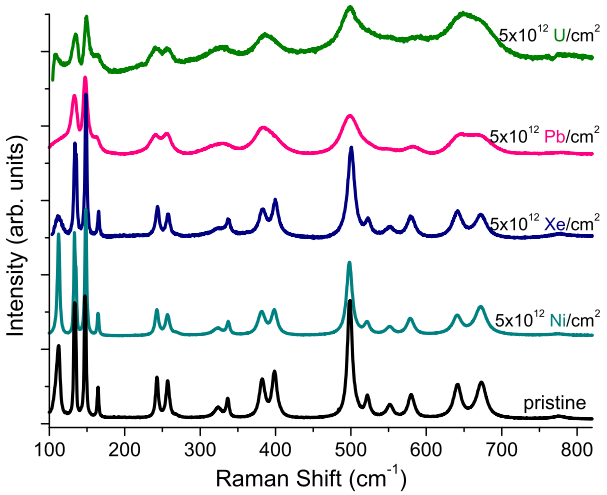

Figure 5.41: Raman spectra of HfO_2 irradiated with the same fluence (5×10^{12} ions/cm^2 for various ion species.

to at least 105 GPa [195, 192]. This transition is accompanied by a volume decrease of $\sim$ 9 %. This reconstructive transition is also very sluggish at ambient temperature. At elevated temperatures (above 1300°C), the transition into the ortho-II phase starts from the tetragonal structure and occurs then quite temperature independent at 14.5 GPa. The ortho-II phase is highly incompressible, with a bulk modulus of $\sim$ 312 GPa [195], and thus a candidate for ultra-hard materials. Once the ortho-II phase has been fully formed, it is quenchable down to ambient pressure.

5.3.2 Irradiations at ambient pressure

Under swift heavy ion irradiation, HfO_2 behaves similar to ZrO_2. Fluence series for different ion species were performed with 11.1 MeV/u. All irradiation parameters are listed in Table 5.8. The Raman analysis of the fluence series with U-ions is shown in Fig. 5.40. The lowest spectum belongs to a pristine (monoclinic) HfO_2 sample. It has 16 dominant Raman bands at 112, 133, 148, 165, 242, 257, 324, 326, 383, 398, 499, 521, 550, 580, 641, and 673 cm^{-1}. This Raman spectrum resembles the one of ZrO_2 as can be expected. The higher-frequency bands belong to the oxygen vibration and, since the configuration of HfO_2 resembles strongly the one of ZrO_2, they appear at almost the same positions. It was proposed, that because the substitution of Zr with Hf doubles the cation mass (from 91.2 to 178.5), all vibration frequencies primarily produced by the cationen motion would decrease by $\sim$ 30 %, whereas frequencies related to oxygen motion would retain their position [185]. This agrees well with observed results. Above 400 cm^{-1} the ZrO_2 and HfO_2 look alike. And in the low-frequency region, the two strongest peaks at 133 and 148 cm^{-1} in HfO_2 are comparable to the two strongest peaks at 178 and 190 cm^{-1} in ZrO_2. This corresponds to a shift of $\sim$ 25 %, agreeing well with the prediction. This allows us to compare the Raman behavior of HfO_2 with the one of ZrO_2.

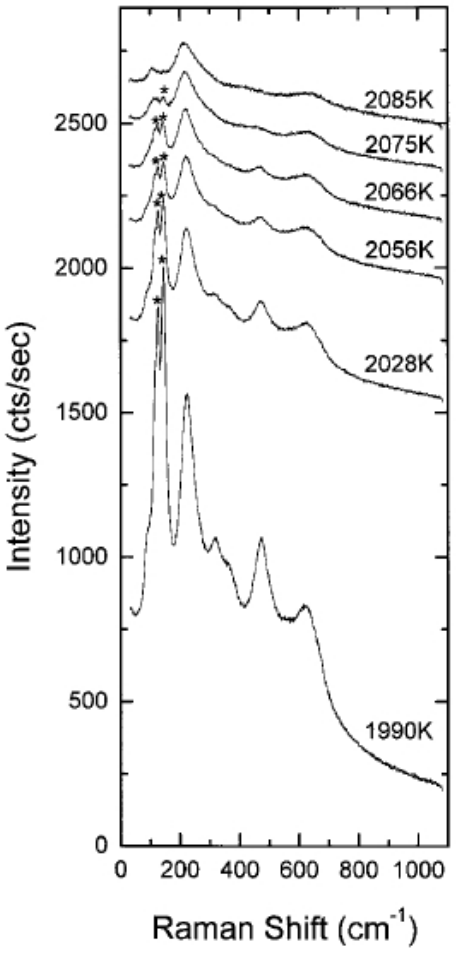

Figure 5.42: Raman spectra of HfO_2 at various high temperatures. Diagram taken from [198].

The radiation response to the Raman spectra is displayed in Fig. 5.40. With increasing ion fluence the bands broaden and merge together. Also a severe intensity loss is observed. The most obvious effect is the vanishing of the bands at 112 and 165 cm^{-1} indicated by the dotted lines. Due to the strong analogy between the two compounds, one would also expect a transition into the tetragonal phase. Although one can observe an obvious change, it does not resemble those the spectra of tetragonal ZrO_2. Comparing the spectra of highly irradiated HfO_2 with spectra reported in literature at high temperatures (see Fig. 5.42), one can see that they resemble a spectrum obtained at around 1990 K, which is the transition temperature from the monoclinic to the tetragonal phase. (For higher temperatures it displays the characteristic six-band spectra of the tetragonal structure). This gives us the information that the energy input from the U-ions causes a temperature increase of $\sim$ 1700 K. Of course, the effect is more complex than a pure temperature increase. The tetragonal phase can indeed be produced by high temperature but not stabilized to ambient temperature. In the case of ZrO_2 a temperature increase of 1700 K is sufficient to be well within the stability field of the tetragonal phase which starts above 1450 K. This is the reason why the transformation is far more progressed for ZrO_2 than for HfO_2 after ion irradiation with the same fluence.

Fluence series have been performed for Ni, Xe, Pb, and U ions. Figure 5.41 shows the results of an irradiation with $5{\times}10^{12}$ ions/cm^2 for various ion species. Heavier ions produce more damage at the same ion fluence. This is not surprising since the electronic energy loss scales with increasing charge state Z^2 of the projectile. At the energy of 11.1 MeV/u, the electronic energy loss is 11.9 keV/nm for Ni, 34.8 keV/nm for Xe, 53.5 keV/nm for Pb, and 67.8 keV/nm for U-ions. Similar to ZrO_2, one has to surpass an energy loss threshold before the ions can induce a phase transformation. Experimentally, this threshold lies at $\sim$ 20 keV/nm [199]. Using the thermal spike approach and assuming that the product of specific heat and density is the same for ZrO_2 and HfO_2, one can expect the following relation [199]:

$$\frac{\left(\frac{dE}{dx}\right)_{thr.}^{HfO_2}}{\left(\frac{dE}{dx}\right)_{thr.}^{ZrO_2}} \cong \frac{(T_c - T_0)^{HfO_2}}{(T_c - T_0)^{ZrO_2}} \tag{5.11}$$

with T_c being the transition temperature and T_0 the starting temperature of the sample. According to the thermal spike model, the energy loss threshold should scale with the corresponding transition temperature. Using Eq. 5.11, we get a theoretical energy loss of 19.2 keV/nm which agrees well with experimental findings.

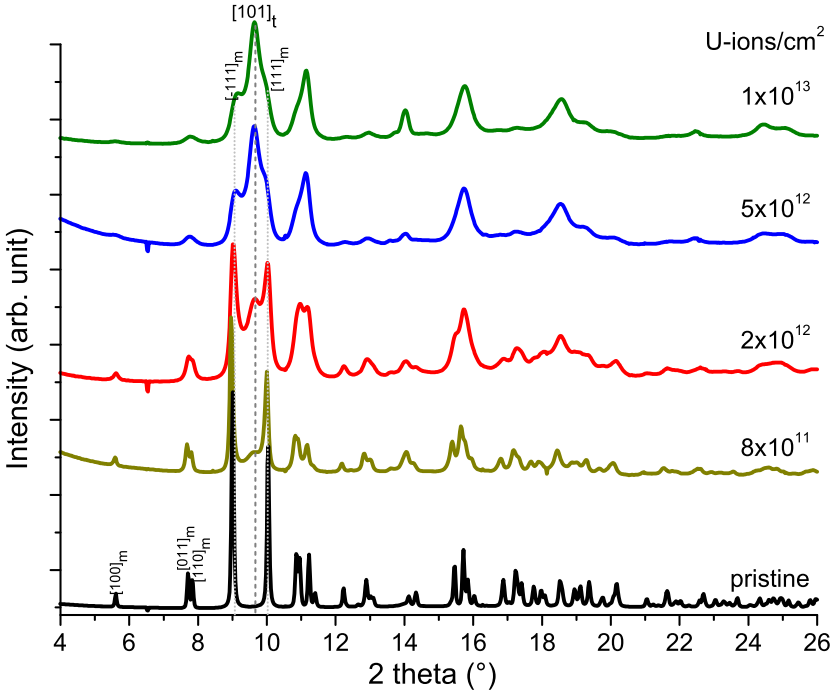

Figure 5.43: X-ray spectra of HfO_2 irradiated at ambient pressure with 11.1 MeV/u U-ions for various fluences (same sample as in Fig. 5.40).

For irradiation with Ni ions, the energy loss of 11.9 keV/nm is not high enough to provoke any phase transformation, therefore no deviation from a pristine sample can be observed in Fig. 5.41. For all other ion species, the electronic energy loss lies well above the threshold, therefore inducing a structural change in the sample. Already for the Xe irradiation, the first Raman peak drops drastically and is completely gone for Pb and U ion irradiation.

Complementary X-ray diffraction analysis has also been performed on the HfO_2 samples irradiated with U-ions. The diffraction patterns are displayed in Fig. 5.43. Pristine HfO_2 has the same monoclinic structure as ZrO_2 with its two strongest reflections $[-111]_m$ and $[111]_m$ at 9.01° 2θ and 10.04°, respectively. The refined lattice constants are a = 5.126, b = 5.186, and c= 5.295 Å and an angle β of 99.3°. With increasing fluence, the $[101]_t$ reflection from the tetragonal phase starts to appear at 9.59° (indicated by the dashed gray line). This band becomes stronger with increasing fluence while

Table 5.8: Irradiation parameters for all HfO_2 samples irradiated at the UNILAC at ambient pressure conditions.

Ion	E_{init} (GeV)	dE/dx (keV/nm)	Fluence Φ (ions/cm^2)	Pressure (GPa)	Initial structure	Final structure	Radius (nm)
macro-crystalline HfO_2							
^{238}U	2.64	67.8	0.05 - 1.0×10^{13}	ambient	mono	part. tetragonal for Φ ≥ 5×10^{12}	6.8
^{208}Pb	2.31	53.5	0.05 - 7.5×10^{12}	ambient	mono	part. tetragonal for Φ ≥ 7×10^{12}	5.7
^{132}Xe	1.47	34.8	0.05 - 1.0×10^{13}	ambient	mono	part. tetragonal for Φ > 1×10^{13}	4.0
^{59}Ni	0.65	11.9	0.1 - 1.0×10^{13}	ambient	mono	no transition induced	—

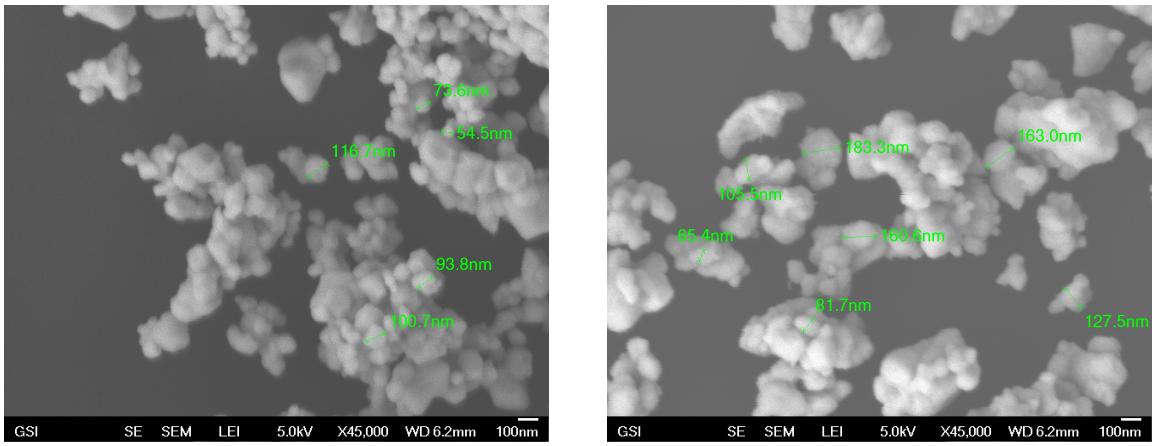

(a) (b)

Figure 5.44: Scanning electron microscopy images of pristine (a) and irradiated (1×10^{13} U-ions/cm^2) HfO_2(b).

the monoclinic reflections weaken. This is the same bahavior as for ZrO_2. In contrast to irradiation of ZrO_2, the radiation induced phase transition is far from being complete for 1×10^{13} ions/cm^2. It is still a mixture of two phases with a tetragonal amount of $\sim$ 55 %. The tetragonal fraction seems to saturate at this value. The $[-111]_m$ and $[111]_m$ reflections of the monoclinic phase are still clearly visible (indicated by the gray dotted lines). Also the weaker bands ($[100]_m$ at 5.6°, $[011]_m$ at 7.7°, and $[110]_m$ at 7.8°) are stable up to this high fluence. For ZrO_2 the monoclinic fraction is no longer detectable. The calculated lattice parameters for the tetragonal structure after 1×10^{13} U-ions/cm^2 are $a = 3.636$ and $c = 5.153$ Å. In principle, the radiation induced transformation mechanism is the same for HfO_2 and ZrO_2 but the energy introduced into the system by ion irradiation is not sufficient to complete the transformation in HfO_2. This might be due to the fact that the transition temperature is $\sim$ 550 K higher in HfO, or that the HfO_2 compound is by 42 kJ/mol more stable than ZrO_2 [196].

5.3.3 Strain analysis

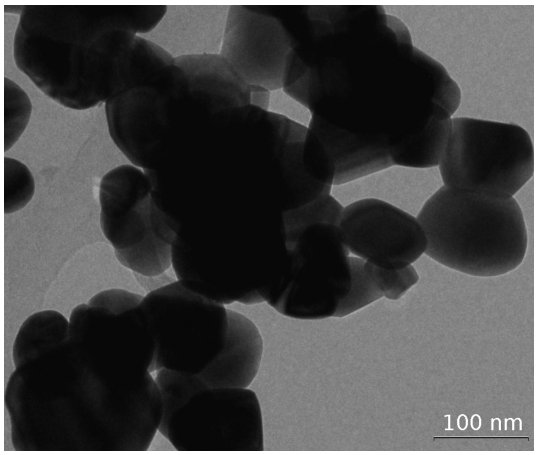

Figure 5.45: TEM image of pristine HfO_2.

Pure HfO_2 is like ZrO_2 a fine white powder. For all experiments a 99.95 % pure HfO_2 powder, purchased from Alfa Aesar™, was used. Via scanning- and transmission electron microscopy (see Figs. 5.44 and 5.45)the crystallite size was estimated to be around $\sim$ 150 nm. The SEM image indicates no change in the crystallite size after irradiation with 1×10^{13} U-ions/cm^2 (see Fig. 5.44(b)). As for ZrO_2, the induced transformation is probably due to radiation induced defects in the form of oxygen vacancies and the therefore resulting strain within the sample. The microstrain in the HfO_2 sample was extracted from the X-ray diffraction data and is depicted in Fig. 5.43. With increasing fluence, a strong broadening of the XRD bands can be observed. The integral

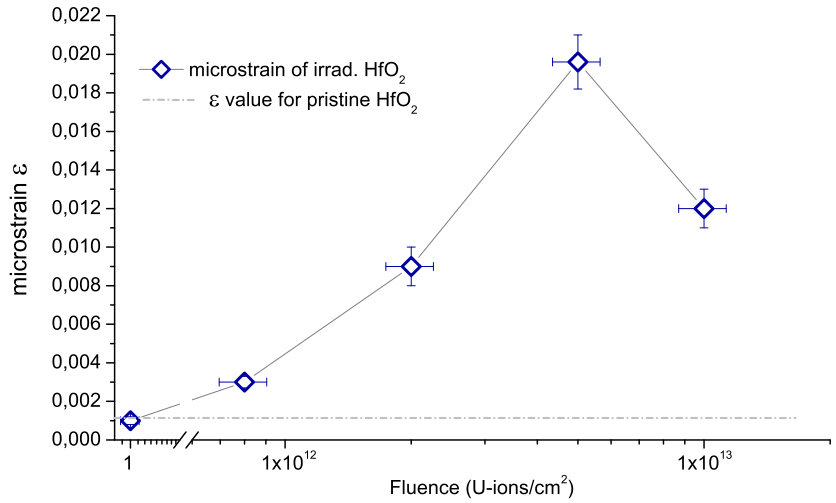

Figure 5.46: Calculated microstrain ϵ in HfO_2 versus ion fluence.

breadth of the reflections broadens by a factor more than five indicating strong strain in the sample. The integral breadth β of the monoclinic $[-111]_m$ and $[200]_m$ and the tetragonal $[101]_t$ reflection as well as the calculated microstrain are summarized in Table 5.9.

Figure 5.46 shows the progression of microstrain in the sample versus the U-ion fluence. The strain in HfO_2 shows a similar behavior as for ZrO_2. The strain increases with increasing fluence, and peaks for $5{\times}10^{12}$ U-ions/cm^2 before going down to a medium high value. Although the trend is the same, the values are higher for HfO_2 than for ZrO_2. As mentioned before, the ions are not able to induce a complete phase change in the material, so that always a mixture of the two phases is produced. Because the tetragonal structure is denser than the monoclinic one, the radiation induced strain is enhanced by the strain along the surface boundaries between the two crystal structures. For low fluence, one can imagine a monoclinic crystal in which small domains of the tetragonal structure occur. Due to the density difference of ~ 0.5 g/cm^3, a "ripping" occurs in the material. This strain should have a maximum at an equal concentration of monoclinic and tetragonal phases. This agrees well with the peak at fluence of $5{\times}10^{12}$ U-ions/cm^2 as the tetragonal fraction was estimated to be 49.7 %. With further increase of the fluence, the phase mixture is shifted in favor of the tetragonal structure and less phase boundaries

Table 5.9: Integral breadth for two monoclinic reflections and one tetragonal reflection of irradiated HfO_2. The microstrain ϵ was calculated from Rietveld profile parameters.

Fluence (ions/cm^2)	**β for $[-111]_m$**	**β for $[200]_m$**	**β for $[101]_t$**	**microstrain ϵ**
0	0.089 ± 0.002	0.088 ± 0.002		0.001 ± 0.0002
8×10^{11}	0.139 ± 0.042	0.0.232 ± 0.033		0.003 ± 0.0003
2×10^{12}	0.266 ± 0.050	0.284 ± 0.048	0.422 ± 0.055	0.009 ± 0.0001
5×10^{12}	0.429 ± 0.055	0.369 ± 0.041	0.604 ± 0.060	0.020 ± 0.0014
1×10^{13}	0.589 ± 0.055	0.381 ± 0.052	0.805 ± 0.063	0.011 ± 0.0010

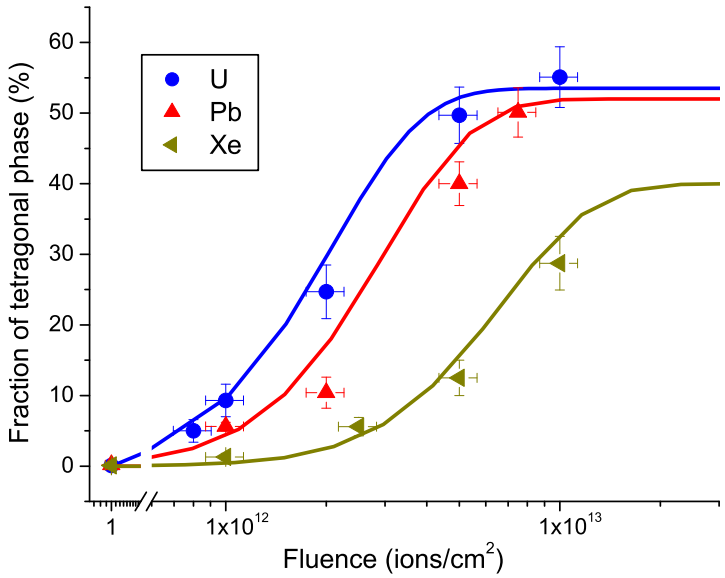

Figure 5.47: Evolution of the tetragonal phase in HfO_2 versus ion fluence for Xe, Pb, and U ions. The solid curves are the best fit of Eq.(5.9) to the experimental data using a cascade-overlap model.

exist in the sample. Probably the strain derived from the X-ray diffraction data can be attributed to ion irradiation and the resulting phase boundaries.

5.3.4 Transformation process

Figure 5.47 shows the tetragonal amount in percent of HfO_2 versus the ion fluence for three different ion species. Similar to ZrO_2 the evolution of the tetragonal phase shows a sigmoidal shaped behavior so that one can assume the same double damage overlap mechanism as described for ZrO_2 in Section 5.1.5. Note that the curves do not saturate around 100 % but far lower at $\sim$ 50 % for heavy and 40 % for medium heavy ions. The ions are not capable to induce a full transformation. The curves give the best fit of Eq. 5.9 to the measured data. From this, we derived a saturation value of $A(\infty) = (53.5 \pm 1.6)$ %, $\sigma = (1.45 \pm 0.08) \times 10^{-12}$ cm^2 for U-ions, $A(\infty) = (52.0 \pm 1.8)$ %, $\sigma = (1.01 \pm 0.08) \times 10^{-12}$ cm^2 for Pb-ions, and $A(\infty) = (40.3 \pm 2.4)$ %, $\sigma = (4.45 \pm 0.20) \times 10^{-13}$ cm^2 for Xe-ions. From the damage cross section σ the following ion track radii were deduced: (6.79 $\pm$ 0.2) nm for U, (5.67 $\pm$ 0.2) nm for Pb, and (3.76 $\pm$ 0.2) nm for Xe ions. The radii are also listed in Table 5.8.

5.3.5 Comparison to thermal spike calculations

As for ZrO_2, thermal spike calculations have been performed to compare our experimental results with the theoretical model. The band gap energy of monoclinic HfO_2 is 3.95 eV [182]. From Fig. 5.13, one can see that the electron-lattice interaction mean free path λ should be around 5 nm. For ZrO_2 we already showed that the “melt-phase” approach, which means that the energy introduced into the sample is high enough to raise the temperature from the irradiation temperature to the melting temperature (3030 K

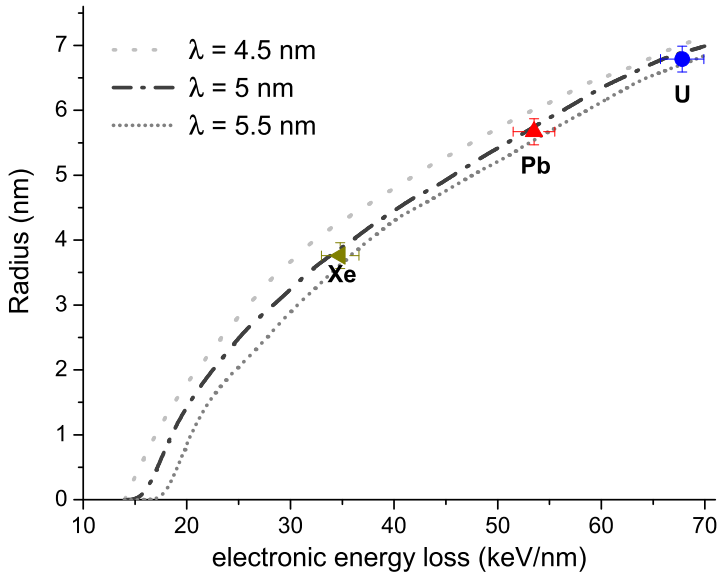

Figure 5.48: Measured track radii in HfO_2 produced by Xe, Pb, and U ion irradiation at 11.1 MeV compared to thermal spike calculations assuming track creation by melting $T > T_m$ for various mean free paths λ.

for HfO_2 [131]), provided best agreement with the measured data. The thermal conductivity of HfO_2 is 1.8 W/K m. Thermal spike calculations have been performed for λ = 4, 4.5, and 5 nm. The resulting curves are shown in Fig. 5.48. The measured track radii for all tested ion species agree (within error bars) well with the theoretical values calculated for the molten track mechanism. Also for HfO_2, the best agreement occurs for λ = 5 nm with the reasonable assumption of a band gap energy of 3.95 eV (see Fig. 5.13). Also for HfO_2, the thermal spike calculations are a useful tool for predicting the damage track radius.

5.3.6 Pressure dependence of pristine HfO_2

Before combining irradiation and high pressure in the forthcoming experiments, the influence of pressure alone on HfO_2 was tested. Therefore, HfO_2 was hydrostatically compressed in a DAC, and Raman as well as X-ray diffraction measurements were performed under pressure. Several compression cycles have

Table 5.10: Lattice parameters and structural composition for HfO_2 at various pressures.

Pressure (GPa)	**Phase**	**a (Å)**	**b (Å)**	**c (Å)**	β (°)
ambient	monoclinic (100 %)	$(5.126 \pm 0.003)_m$	$(5.186 \pm 0.003)_m$	$(5.295 \pm 0.003)_m$	99.3
4.3	mono + ortho-I (3.0 ± 0.6) %	$(5.087 \pm 0.003)_m$	$(5.191 \pm 0.004)_m$	$(5.235 \pm 0.003)_m$	98.9
7.5	mono + ortho-I (39.8 ± 3.5) %	$(9.967 \pm 0.008)_{o-I}$	$(5.196 \pm 0.005)_{o-I}$	$(5.172 \pm 0.007)_{o-I}$	90
10.5	mono + ortho-I ((64.3 ± 3.8) %)	$(9.923 \pm 0.010)_{o-I}$	$(5.201 \pm 0.006)_{o-I}$	$(5.011 \pm 0.006)_{o-I}$	90
14.	mono + ortho-I (83.5 ± 3.5) %	$(9.881 \pm 0.006)_{o-I}$	$(5.191 \pm 0.004)_{o-I}$	$(4.989 \pm 0.04)_{o-I}$	90
17.7	ortho-I (92.4 ± 4.0 %)	$(9.825 \pm 0.010)_{o-I}$	$(5.180 \pm 0.010)_{o-I}$	$(4.938 \pm 0.012)_{o-I}$	90
21.5	ortho-I (100 %)	$(9.780 \pm 0.008)_{o-I}$	$(5.172 \pm 0.008)_{o-I}$	$(4.927 \pm 0.010)_{o-I}$	90
45.0	ortho-II (100 %)	$(5.152 \pm 0.006)_{o-II}$	$(3.131 \pm 0.008)_{o-II}$	$(6.432 \pm 0.008)_{o-II}$	90

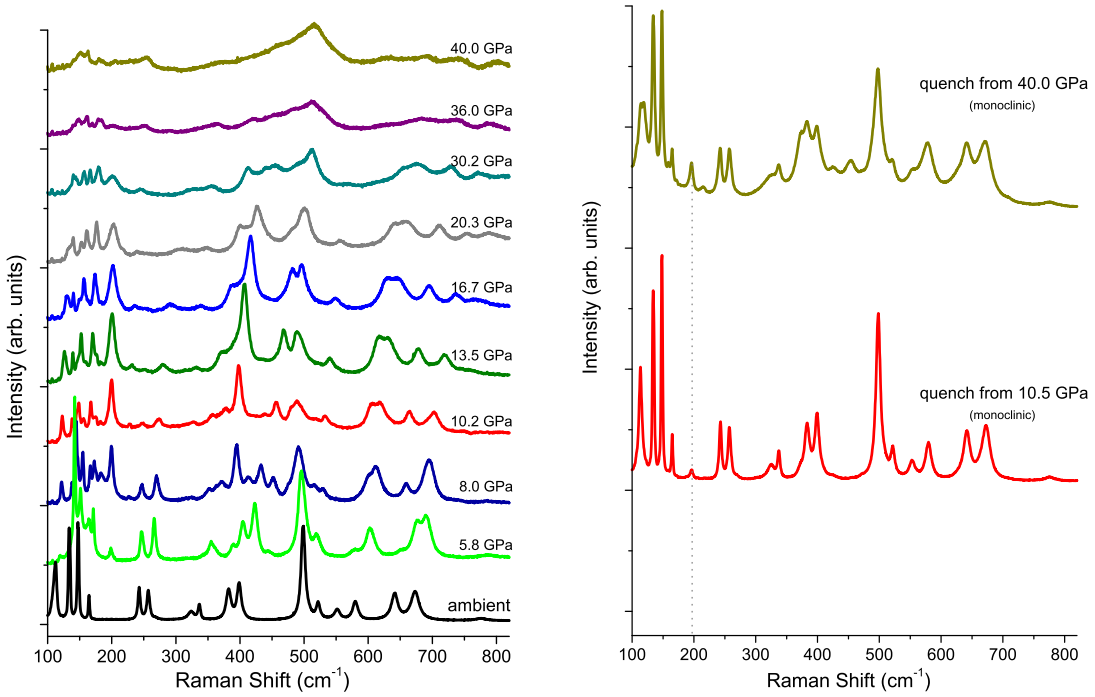

Figure 5.49: Left: Raman spectra of HfO_2 at various pressures. Right: Raman spectra of HfO_2 quenched from different pressures.

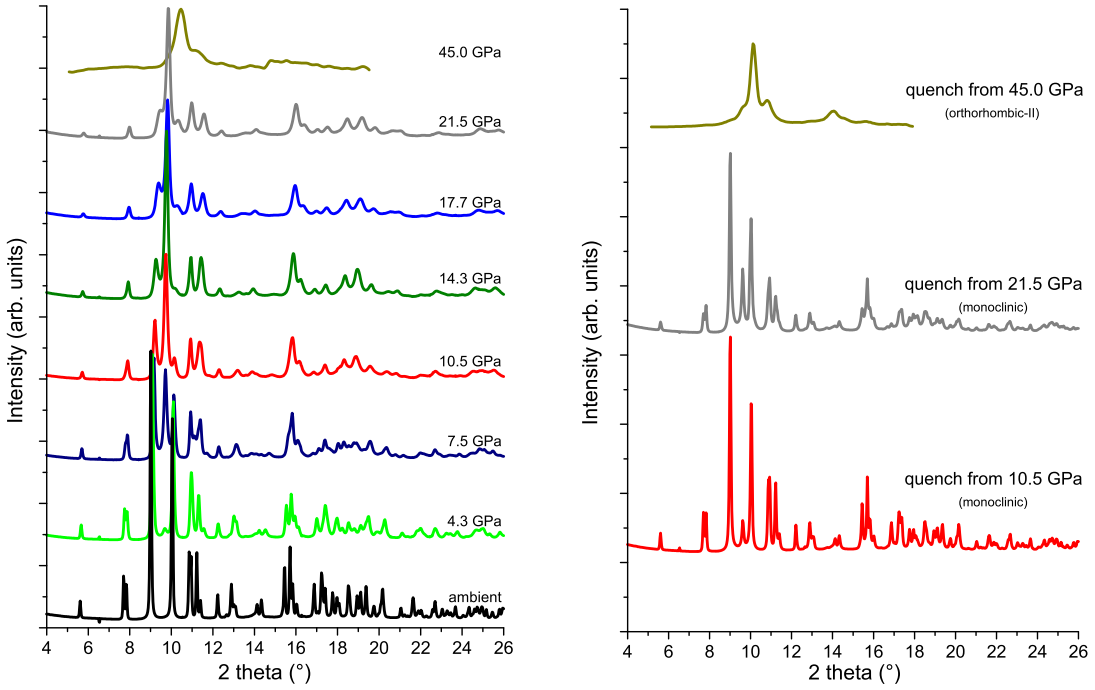

Figure 5.50: Left: X-ray diffraction patterns of HfO_2 at various pressures. Right: X-ray diffraction pattern of HfO_2 quenched from different pressures.

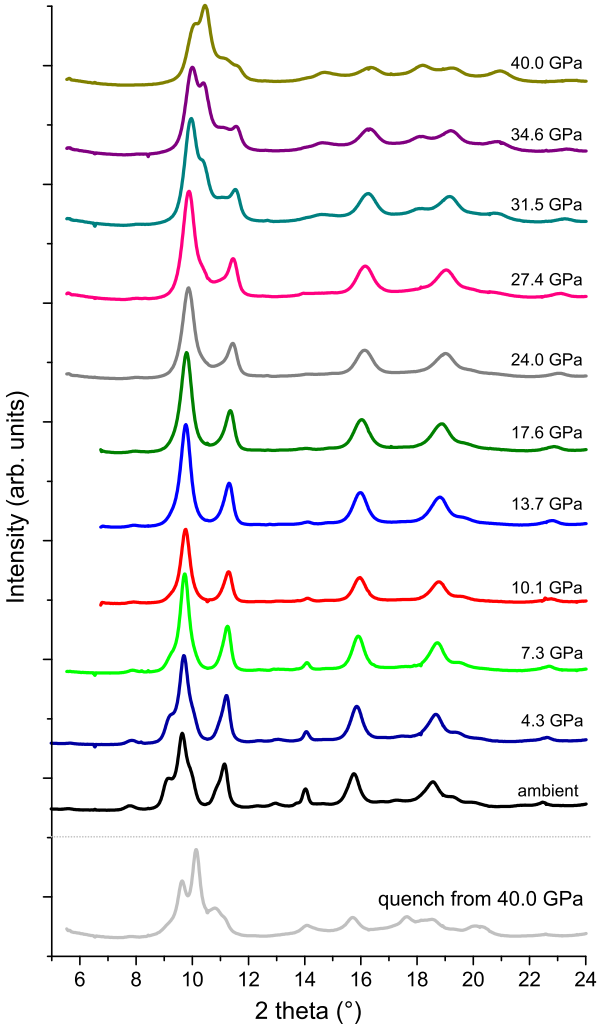

Figure 5.51: X-ray diffraction patterns of HfO_2 irradiated with 1×10^{13} U-ions/cm^2 under various pressures.

been performed to quench the sample from different pressures. The Raman spectra of pressurized HfO_2 are displayed in Fig. 5.49. At ambient pressure, 16 Raman modes can be observed. With increasing pressure most bands shift to higher wavenumbers before new bands appear above 5 GPa, belonging to the first high-pressure phase orthorhombic-I. The most prominent change is in the low-frequency region in which more bands appear, the most important at 199 and 397 cm^{-1}. Up to 14 GPa, there is still an overlap of the monoclinic and ortho-I structures. Around 17 GPa, the sample has completely transformed. For pressures above 30 GPa, a transition into the second high pressure phase (orthorhombic-II) occurs, indicated by the intensity drop of the band at lower wavelength and the dominance of the broad band at 513 cm^{-1}. So far, the behavior with respect to pressure does not differ between HfO_2 and ZrO_2. Even the phase boundaries are located at similar pressures. In order to know in which phase the sample exists after quenching from various pressures, two pressurization and quenching cycles have been performed. The quenching results from 10 and 40 GPa are shown in the right graph of Fig. 5.49. For both cases, the samples returned to the ambient, monoclinic pressure phase. Since the first high-pressure phase is not quenchable, this was expected, but the second high-pressure phase should be quenchable once produced. Similar to ZrO_2, the ortho-I to ortho-II transition is of reconstructive type needing a large amount of excess energy to complete the transformation. Obviously, 40 GPa does not suffice to stabilize the ortho-II phase, and additional pressure would be needed. One should mention that the sample remained 1 day at this high pressure before being quenched. It might be that this in not long enough to overcome the inertness of the transformation process. Under elevated temperature, the transition into the ortho-II phase occurs already at 14.5 GPa [195]. But some indication of the pressure history is visible for both quenched samples. A small band at 199 cm^{-1} could be detected, which belongs to the first high-pressure phase.

For completeness, also X-ray analysis was performed on pressurized HfO_2. Figure 5.50 shows the X-ray diffraction patterns of a different pressurization cycle for pressures up to 21.5 GPa. Additionally a spectrum measured at the BGI at 45 GPa (X-ray energy corrected) was included into the graph. The X-ray measurements give the same results as the Raman measurements. The monoclinic → ortho-I transition

Pressure (GPa)	a (Å)	b (Å)	c (Å)
tetragonal			
0	3.636		5.153
4.2	3.600		5.084
7.3	3.583		5.071
10.1	3.578		5.051
13.7	3.568		5.039
17.6	3.554		5.022
cubic			
7.3			5.071
10.1			5.051
13.7			5.040
17.6			5.023
21.3			5.009
24.0			5.004
27.4			5.004
31.5			5.010
orthorhombic-II			
34.6	5.680	3.455	6.601
40.0	5.653	3.434	6.594

Table 5.11: Refined lattice parameters for the predominating crystalline structures of HfO_2 irradiated with 1×10^{11} U-ions/cm^2 under pressure.

starts at around 4.3 GPa and can be observed best by the very weakly appearing $[211]_{o-I}$ reflection at 9.7°. This reflection grows stronger with increasing pressure whereas the monoclinic reflections $[\text{-}111]_m$ at 9.0° and $[111]_m$ at 10.1° become weaker. The transition is also quite sluggish, so that a mixture of both phases can be observed up to very high pressures. For example at 10.5 GPa, 35.7 % of the sample are still monoclinic although it is already well within the stability field of the first high-pressure structure. The monoclinic concentration decreases with increasing pressure and disappears above 17 GPa. At 45 GPa, the sample displays all characteristic features of the second high-pressure phase. The refined crystal lattice parameters for the predominant structure and phase concentration are summarized in Table 5.10. After quenching from 21.5 and 10.5 GPa, the sample changes back into its monoclinic form which is shown in the right graph of Fig. 5.50. All bands which belong to the monoclinic phase return and are dominating the spectra. But, as already observed in the Raman data, some small amount of the ortho-I phase remains in the obtained sample. About 15.7 % for the sample quenched from 21.5 GPa and 7.5 % for the sample quenched from 10.5 GPa are still ortho-I. This very small amount is probably due to still unrelaxed grains within the sample. HfO_2 pressurized up to 45.0 GPa remains in the ortho-II phase even after the pressure is released which is not surprising since ortho-II is quenchable. So one should keep in mind that for pressures up to at least 21.5 GPa no high pressure phase can be perserved to ambient conditions.

5.3.7 Pressure dependence of irradiated HfO_2

Now the pressure behavior of already irradiated material will be discussed. HfO_2 powder previously irradiated with 1×10^{13} U-ions/cm^2 was mounted hydrostatically in a DAC. Upon pressurization, the diffraction patterns of the sample were recorded at several pressure steps (see Fig. 5.51). Different from ZrO_2, only about 53 % of the irradiated sample had changed into the tetragonal form, so a different

pressure behavior might be possible. With increasing pressure, the monoclinic fraction disappears so that sidebands next to the $[101]_t$ reflection at 9.7° are no longer detectable. It seems that the additional introduced energy in the form of pressure increases the tetragonal amount. At the same time, a second transition occurs in the sample. As already observed for ZrO_2, we probably see a transition from the tetragonal to the cubic structure. Due to the very broad peaks, both structural models can be fitted to the spectra. But since we observed a transformation from the tetragonal into the cubic phase in ZrO_2 during pressurization, the cubic structure can be assumed in this case. All refined lattice parameters are listed in Table 5.11. For lower pressures, the calculated lattice parameters are given for the refinement with the cubic and the tetragonal structure. Around 30 GPa, the transition from the cubic into the ortho-II structure begins. This can be observed by the band of the $[200]_{oII}$ reflection appearing at 10.4°. At 40 GPa the sample exists in a mixture of cubic and orthorhombic-II HfO_2. The sample quenched from 40 GPa (see Fig. 5.51) exhibits mainly orthorhombic-II features, comparable to the quench behavior of unirradiated HfO_2. The ortho-II phase seems to be a superior structure. In spite of the extremely damaged starting material, it is formed at the same pressure conditions and when quenched shows no longer evidence of the radiation history. Although the crystalline structure is not the same as at ambient conditions, this behavior might be an indication of pressure induced defect annealing.

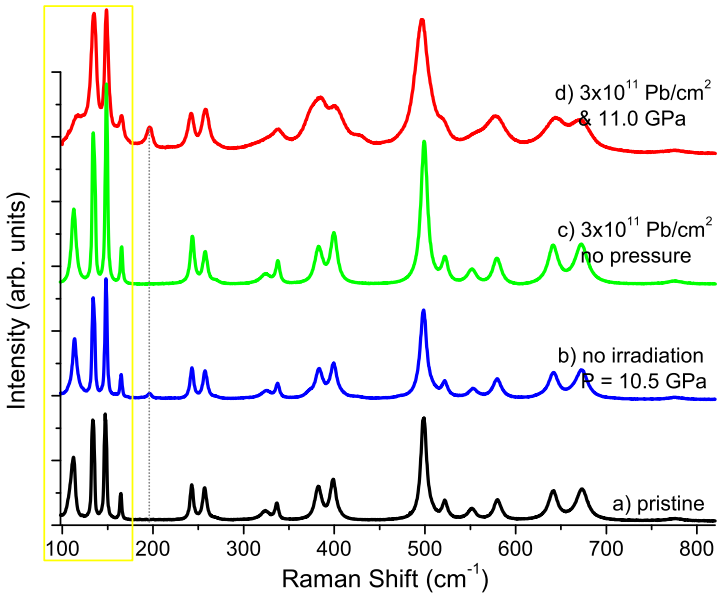

Figure 5.52: Raman spectra at ambient conditions of different HfO_2 samples: (a) pristine, (b) pressurized without irradiation, (c) irradiated with 3×10^{11} Pb-ions/cm^2 but without pressure, (d) irradiated with 3×10^{11} Pb-ions/cm^2 at a pressure of (11.0 $\pm$ 0.3) GPa.

5.4 Irradiations under high pressure

As already shown, the response of a material to swift heavy ion irradiation changes if it is simultaneously exposed to high external pressure. Experiments for high as well as low fluences and different pressures have been conducted. Also in the case of HfO_2 the results differ from irradiations at ambient conditions. For the first experiment, HfO_2 was mounted in a DAC and hydrostatically pressurized up to 11.0 GPa. Then, the sample was exposed to 3×10^{11} Pb-ions/cm^2, a fluence at which usually no detectable change happens. Afterwards the pressure was released, the sample unmounted, and analyzed via Raman spectroscopy. The result compared to pressure- and irradiation- reference samples are shown in Fig. 5.52. The red (top) curve is the Raman spectrum of the HfO_2 sample irradiated while being pressurized. This looks like a spectrum of a sample irradiated with much higher fluences (compare with Fig. 5.40). The band at 112 cm^{-1} is almost completely gone and the one at 165 cm^{-1} is also strongly diminished. At higher wavenumbers a strong broadening of the Raman bands can be observed. The sample exhibits a spectrum usually observed when irradiated with a fluence of one order of magnitude higher. The reference samples prove that neither pressure (blue curve) nor irradiation alone (green curve) could have provoked this strong deformation. But as for irradiations at ambient pressure, no complete transformation into the tetragonal phase is observed. The red curve exhibits one other change which has not been observed for any previous investigated radiation response. At 197 cm^{-1}, a small peak appears which does not belong to any high-temperature polymorph of HfO_2. Comparing it with the pressure reference sample, one can assume that this band is some relict of the first high-pressure phase which did not relax back yet during the decompression. This is surprising since the first high-pressure phase is not stable at ambient pressure. This peak is even stronger pronounced than for the reference

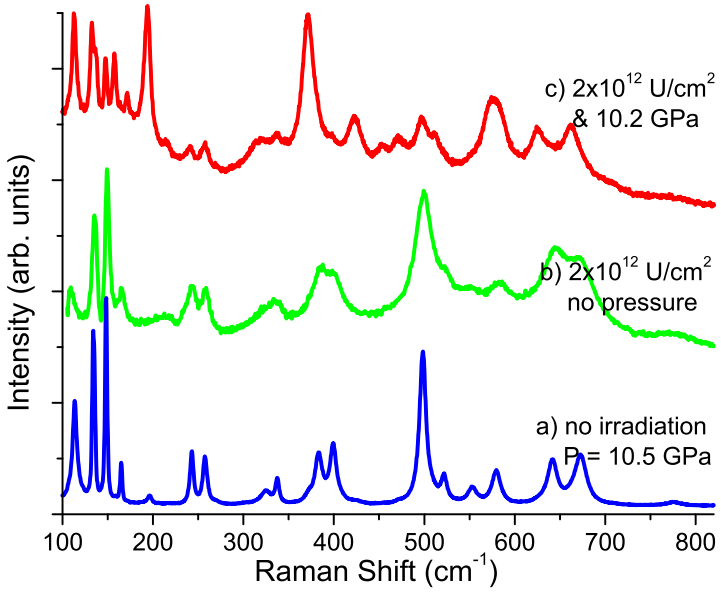

Figure 5.53: Raman spectra at ambient conditions of different HfO_2 samples: (a) pressurized to 10.a GPa but not irradiated, (b) irradiated with 2×10^{12} U-ions/cm^2 but without pressure, (c) irradiated with 2×10^{12} U-ions/cm^2 under pressure of (10.2 $\pm$ 0.3) GPa.

sample. This is the first indication of an interesting radiation response behavior which can be clearly identified for high-fluence radiation conditions.

The radiation response under pressure is more pronounced when the ion fluence reaches the overlap regime. Therefore, a similar experiment has been performed for a fluence of 2×10^{12} U-ions/cm^2 on a sample compressed to 10.2 GPa. The results plus comparison to references is shown in Fig. 5.53. The sample irradiated under pressure shows quite a surprising response. Instead of changing into the high-temperature tetragonal form as observed for ZrO_2, it remains in the high-pressure (ortho-I) structure, clearly indicated by the strong bands at 113, 132, 193, and 370 cm^{-1}. Besides the red shift, due to the applied pressure, the measured sample looks exactly like the one obtained at 10.2 GPa (compare with Fig. 5.49). Since this high-pressure phase is usually not quenchable it is amazing to see it preserved to ambient conditions. The sample remains stable over a period of at least one year and is not influenced by the energy of the detecting Raman laser light. It is also noteworthy that besides all the strong similarities of ZrO_2 and HfO_2, their radiation response under pressure differs immensely. To gain a better understanding of this transformation process, the experiment was repeated to look at the transformation steps also under high pressure. Figure 5.54 shows the transition route after pressurization, irradiation and decompression. The first picture (Fig. 5.54(a)) shows the XRD spectrum of pristine HfO_2 in its monoclinic structure with its two strong peaks at around 9° and 10°. This structure possesses the largest number of degrees of freedom with the unit cell having three different cell vectors and one not right-angle β [113]. Therefore the diffraction image shows a large number of diffraction rings. With increasing pressure the ortho-I structure begins to form clearly indicated by the $[211]_o$ peak growing between the two monoclinic peaks at 9.7°. Of course, also peaks at lower and higher diffraction angles change but the transition becomes most obvious in the region around 10°.

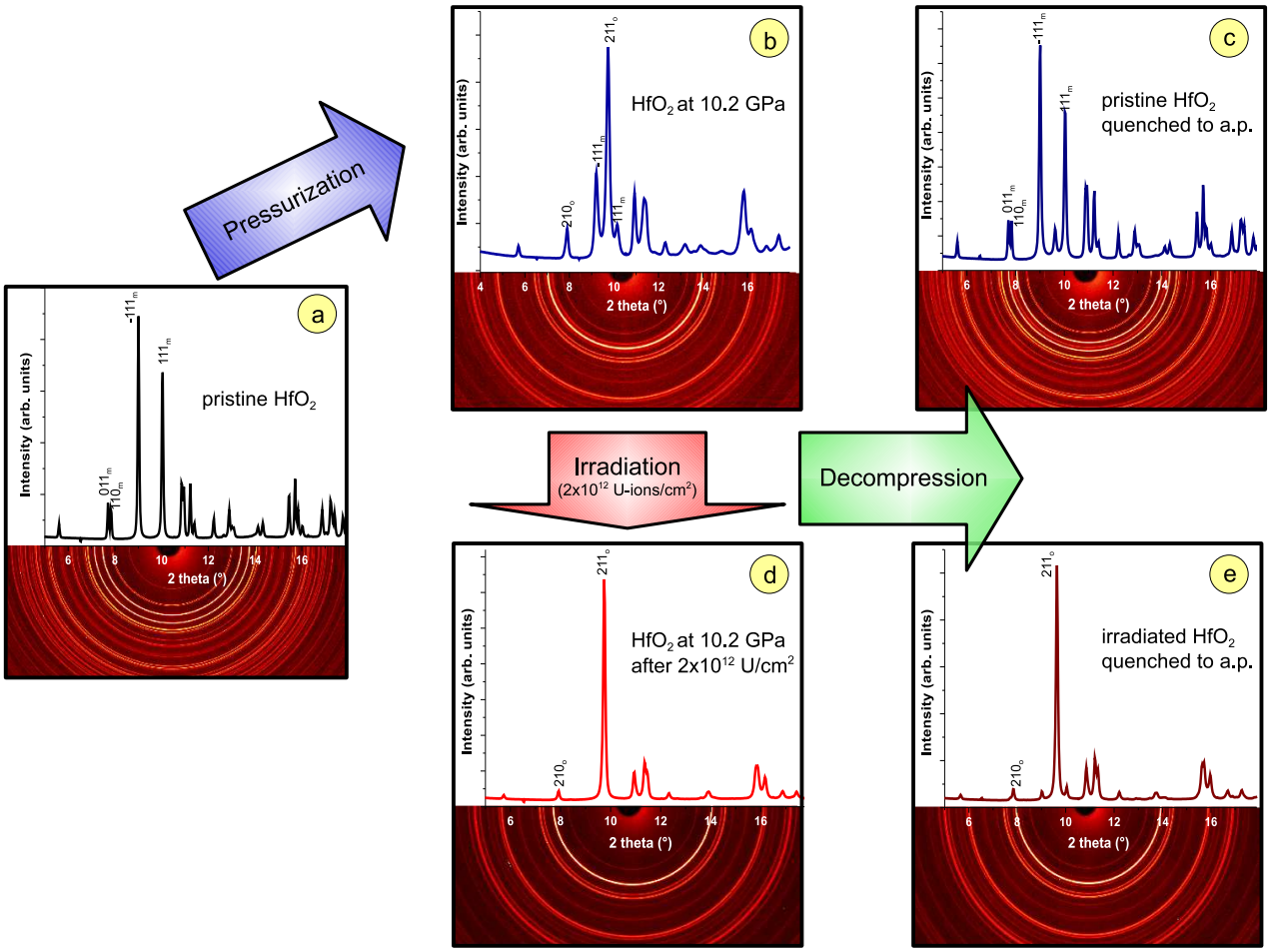

Figure 5.54: X-ray diffraction spectra of the different stages of the experiment. At ambient conditions HfO_2 shows peaks of the monoclinic structure (a). Pressurized to 10.2 GPa, new reflexes which belong to the ortho-I phase appear as a mixture of monoclinic/ortho-I (b). Additional irradiation with 2×10^{12} U-ions/cm^2 provokes a completion of the transition into ortho-I (d). When releasing the pressure, the unirradiated sample transforms back into its monoclinic form (c), whereas the irradiated sample remains stable in the high pressure phase (e). Below the X-ray spectra, their respective diffraction images are shown.

Although the ortho-I structure is dominating at 10.2 GPa, there is still more than 30 % of the sample in the monoclinic phase. Quenching the unirradiated sample back to ambient pressure it changes back into the monoclinic structure. Directly after quenching, a very small signal of the previously existing high-pressure phase ($\sim$ 7.5 %) remains, which further decreases when the sample has more time to relax. If however the sample is irradiated under a pressure of 10.2 GPa, we observe a complete transformation into the first high-pressure phase with a lattice structure of $a = 10.012$, $b = 5.189$, and $c = 5.051$ Å. Not even the slightest signal of the monoclinic phase is detected. This transformation is even stronger progressed than under a simple pressurization up to 20 GPa. Due to the higher symmetry of ortho-I compared to monoclinic, the diffraction image shows fewer but very strong diffraction rings. This degree of transformation is truly remarkable. But the most remarkable situation can be observed after decompression. As mentioned before, the ortho-I structure can not be quenched neither for HfO_2 nor for ZrO_2.

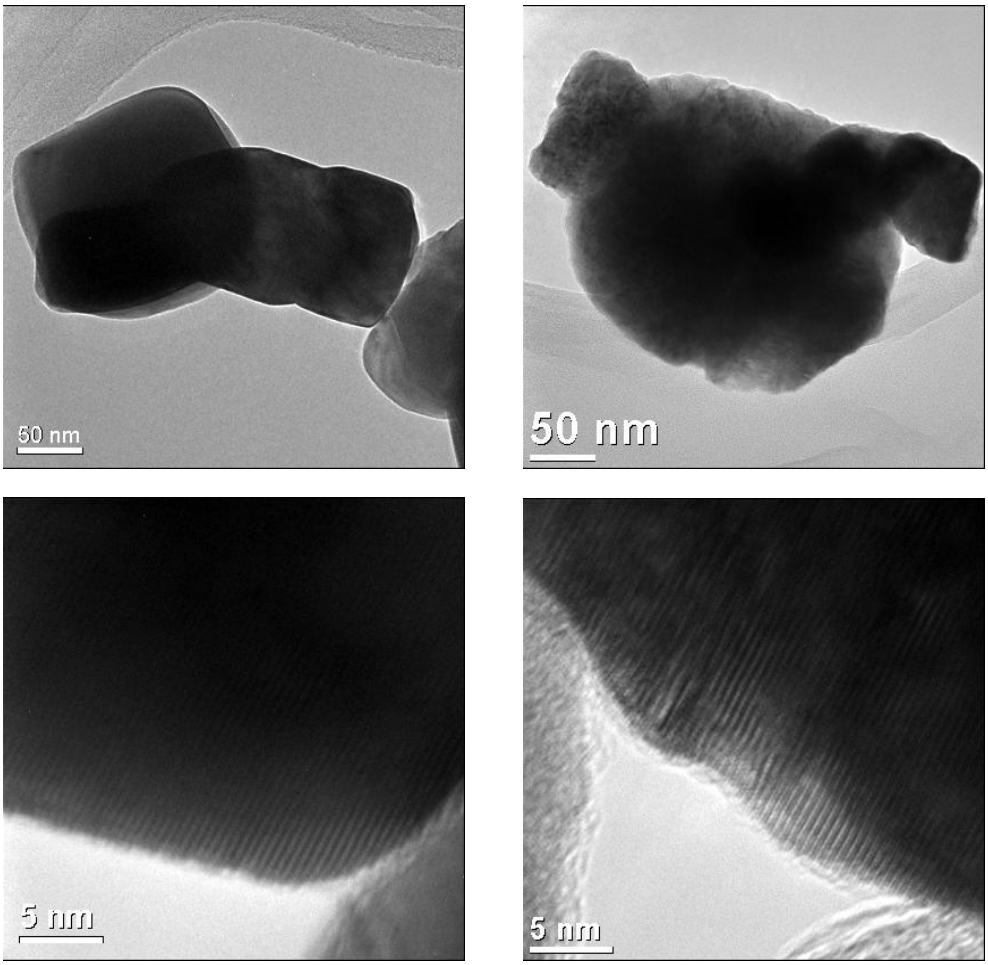

Figure 5.55: Transmission electron microscopy images of pristine (left column) and under pressure irradiated (10.2 GPa and 2×10^{12} U-ions/cm^2) HfO_2 (right column).

Therefore, it is extremely surprising to observe that the ortho-I structure is perserved down to ambient pressure. Small impurities of the monoclinic phase are visible at ambient pressure but more than 93 % of the sample exists in its ortho-I structure. This phase is not only stable directly after quenching but could be preserved until this day. The refined lattice parameters are $a = 10.043$, $b = 5.239$, and $c = 5.071$. This is a very good example how the combination of swift-heavy ion irradiation with high-pressure is capable to not only induce untypical phase transformations but also stabilize usually unstable structures to ambient conditions.

To additionally confirm the orthorhombic structure (besides Raman and XRD), TEM examinations have been performed (see Fig. 5.55). As for ZrO_2 no nanocrystallization effect can be observed after irradiation. But the irradiated samples also show a ripple-like structure pointing to a large amount of strain within the sample. As for the high-resolution images, one can clearly see that no amorphization was induced since the irradiated sample still shows a periodical structure. The observed structure and additional diffraction measurements also point to the orthorhombic phase with probably some small mixture of the monoclinic one. The lattice structure is not even as is should be for the cubic or tetragonal phase so a transition into these structures can definitely be ruled out.

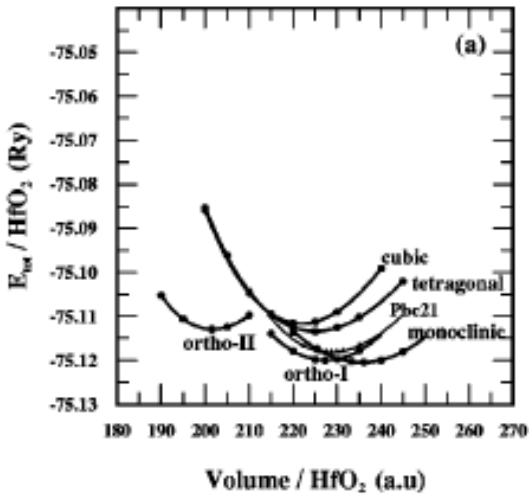

Figure 5.56: Total energies of HfO_2 conformations vs. volume. This picture is taken from [191].

Now the question arises what, despite all the strong similarities between HfO_2 and ZrO_2, causes this difference in radiation response under pressure. As shown before, the behavior under pressure alone is the same for ZrO_2 and HfO_2. Also the radiation response is very similar for both materials. A multiple-damage overlap mechanism induces a phase change from monoclinic to tetragonal. But the behavior under ion irradiation is not exactly the same. Whereas ZrO_2 transforms completely into the tetragonal form, HfO_2 can only be shifted to the transition boundary of these two phases. HfO_2 seems to be much less sensitive to irradiation than ZrO_2. The energy transferred by the ions does not suffice to invoke a phase transformation in the target: this is attributed to the higher transition temperature. Under pressure, the transition temperature is lowered by $\sim$ 400 K but still the irradiation process does not change the sample to the high-temperature phase. Actually the additional irradiation completes the sluggish process of transformation into the high pressure phase in whose stability field the sample already exists (see Fig. 5.54(d)). The fact that HfO_2 is more stable than ZrO_2 [196] might have an effect on the radiation response under pressure. Lowther et. al. and other groups have shown, via total-energy calculations, that besides the general similarity between the phases of ZrO_2 and HfO_2, the relative ordering in energy of the phases has some influence on the formation of the phases, especially the first orthorhombic phase and its formation from the monoclinic phase [113]. The total energies of the monoclinic and ortho-I phases lie within a much closer energy range ($\sim$ 10 meV [113]) for HfO_2 than for ZrO_2 suggesting that the transformation between these two structures is more sensitive towards external factors (see Fig. 5.56). Therefore, already at 10 GPa a completion of the transition into the ortho-I structure seems to be energetically more favorable than a change into the tetragonal one. Still, the ions introduce some additional stabilization which allows the quenching of this usually unstable phase. If again strain, evoked by lattice defects and vacancies, is the dominating fact, this demands further insight into the defect production mechanism.

5.4.1 Irradiation under various pressure conditions

So far, only irradiation experiments conducted around 10 GPa, with pressures well within the stability field of the ortho-I structure, have been discussed. We observed a completion of the transition into ortho-I which remained stable even at ambient conditions. Additional experiments have been performed at 3.6, 24.1, and 45.0 GPa, where each sample existed in a different phase before irradiation. At 3.6 GPa, HfO_2 is monoclinic as at ambient pressures, at 24.1 in the ortho-I structure but close to the transition boundary of the ortho-II phase, and at 45.0 GPa it is well within the ortho-II phase. For the sample irradiated at 3.6 and 24.1 GPa, XRD measurements have been performed with a wavelength of $\lambda = 0.7108$ Å (Mo K_{alpha}) under pressure at the BGI. The results are shown in Figs. 5.57 and 5.58. On all samples Raman measurements were performed after decompression to ambient pressure, outside the pressure cell (see

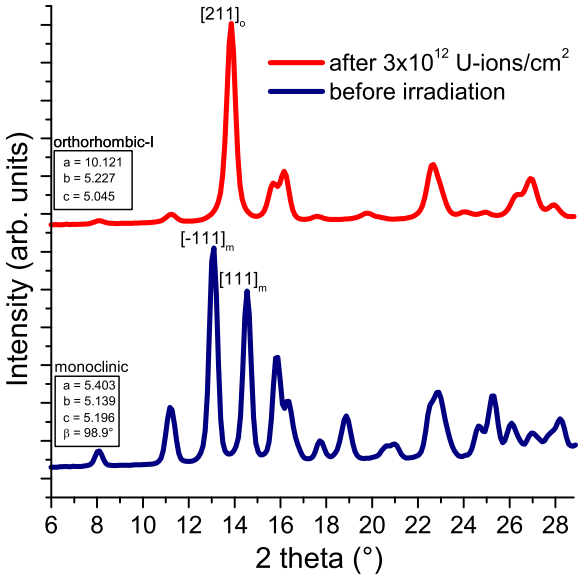

Figure 5.57: X-ray diffraction pattern of HfO_2 at 3.6 GPa before and after irradiation with 3×10^{12} U-ions/cm^2 (λ = 0.7108 Å)

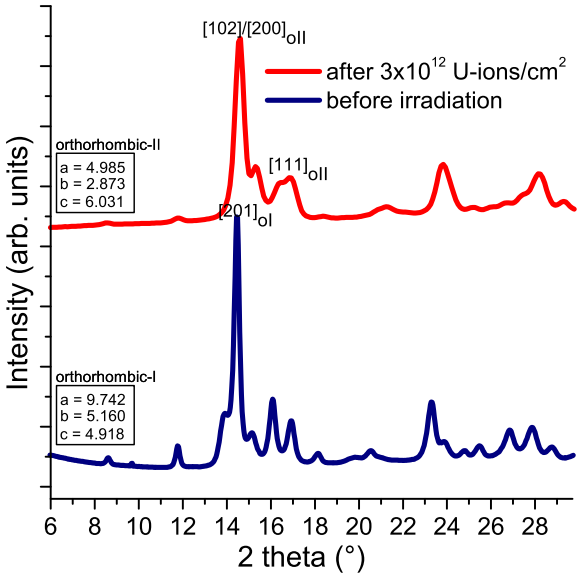

Figure 5.58: X-ray diffraction pattern of HfO_2 at 24.1 GPa before and after irradiation with 3×10^{12} U-ions/cm^2 (λ = 0.7108 Å)

Fig. 5.59). Before irradiation, the sample at 3.6 GPa displays all characteristic peaks of the monoclinic structure. After irradiation with 3×10^{12} U-ions/cm^2 the pattern has completely changed into the one of the ortho-I structure, clearly visible by only one band at around 14° belonging to the $[211]_{oI}$ reflection of the orthorhombic structure. It should be noted, that also in this case the sample exists completely in the ortho-I phase. Obviously, already at these low pressures the ions provoke a complete transformation into the high-pressure phase. This is a similar behavior to an irradiation at around 10 GPa, but obviously the ions not only enhance the transformation process but can also induce it. The pressure was determined after irradiation and showed no increased value; so internal pressure increase can be excluded. However, after pressure release the sample changed again (see Fig. 5.59). It is a mixture of the monoclinic and tetragonal phase which would be observed after irradiation with high fluences. Although a transition into the high-pressure phase occurred, the sample could not maintain it to ambient pressure, in contrast to a sample irradiated at 10.5 GPa. Whatever causes the stabilization of the first high-pressure phase after an irradiation at about 10 GPa, this result is not only due to the combination of high pressure and ion irradiation but the energy introduced by these two parameters has to be above a certain threshold to stabilize the ortho-I phase once produced under irradiation.

For irradiation at even higher pressures the behavior changes again. Figure 5.58 shows the diffraction patterns of HfO_2 at 24.1 GPa before and after irradiation with 3×10^{12} U-ions/cm^2. Before irradiation, the sample exists in the first high-pressure phase ortho-I. As shown in Section 5.3.6, HfO_2 exists in this structure up to 30 GPa above which the second high-pressure phase, ortho-II, is formed. After irradiation the diffraction pattern changed. The sample is no longer ortho-I but changed entirely into the ortho-II structure. Obviously, close to the transition boundary as for ZrO_2, the ions are capable to induce a transition along the pressure route. It seems that the ions can induce stress within the sample which

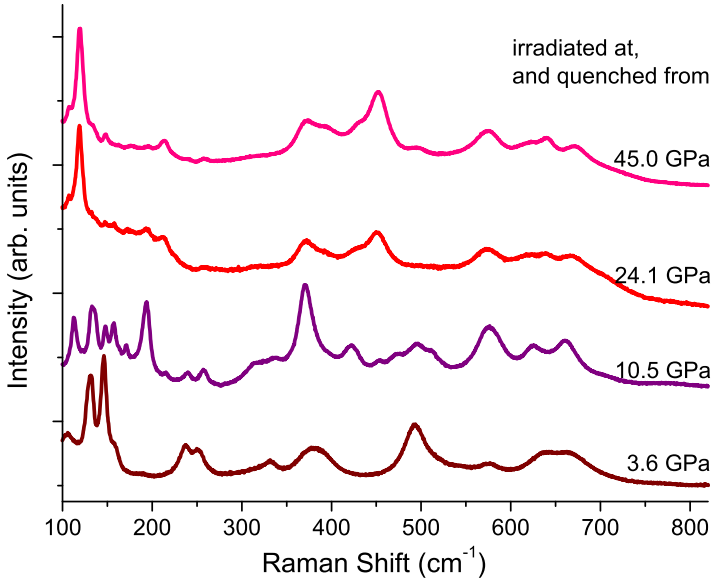

Figure 5.59: Raman spectra of quenched HfO_2 irradiated at various pressures with 3×10^{12} U-ions/cm^2

corresponds to a pressure of more than 6 GPa to evoke this pressure transition and complete it. Because the ortho-II structure is quenchable to ambient conditions, it could be measured outside the pressure cell (see Fig 5.59). The strong Raman band at 119 cm^{-1} is a clear indication of the ortho-II phase [121]. For ZrO_2 and HfO_2, both quenched spectra from irradiations under very high pressures exhibit very similar features, stressing again that both oxides are isostructural (compare with Fig. 5.30). After irradiation of HfO_2 which already exists in the second high-pressure phase before irradiation no additional leads to no additional phase change. Also no obvious radiation defects can be observed. For HfO_2 as well as for ZrO_2, ortho-II is the most stable structure showing no influence towards high-fluence irradiations with swift heavy ions.

6 Conclusion

This thesis sheds light on the response behavior of ZrO_2 and HfO_2 ceramics to heavy-ion irradiation, high pressure, and the combination of these two extreme conditions. Emphasis is placed on the structural conformations and their stability induced by these parameters.
Under high pressure, both materials pass through different crystalline phases. At ambient conditions, they exist in the monoclinic structure and change into the first orthorhombic phase (ortho-I) for pressures above 4 GPa. This phase only exists under pressure and can not be recovered to ambient pressure. Increasing the pressure above 30 GPa, a transition occurs into the second high-pressure phase (ortho-II) which is also of orthorhombic nature. This phase can be quenched to ambient pressure.
It is demonstrated that in HfO_2 as well as ZrO_2, high-fluence irradiations at ambient pressure result in a transformation from the monoclinic into the first high-temperature structure (tetragonal). Not only is the tetragonal phase produced, but also stable at ambient conditions after irradiation, allowing a thourough analysis of the transformation mechanism. Heavy ion irradiation with Xe, Au, Pb, and U ions show that the radiation induced transformation requires multiple ion impacts to produce sufficient defects within the sample. Therefore, very high fluences are needed to evoke any transformation. Grain-size and strain analysis prove that pronounced internal strain is introduced during irradiation. This strain is associated to defects such as interstitials and vacancies which are generated by this process. The double impact mechanism for ambient irradiations can be explained by the need to provide sufficient defect density to induce local strain fields. An ion hitting a pre-damaged region, triggers at the same spot the transformation from defective monoclinic to the tetragonal. Damage track radii for all tested ion species are deduced from the experimental data and prove to be in good agreement with calculated values. The thermal spike model is identified as a valuable tool to predict radiation damage cross sections within the two investigated materials.

The simultaneous exposure to heavy ion irradiation and high pressure, however, shows different results. At pressures around 10 GPa, the ions already induce the above mentioned structural transition for fluences more than one order of magnitude less than at ambient conditions. This is attributed to the pressure induced strain, taking over the part of the first ion pre-damaging the material. Therefore, the first ion is sufficient to trigger the transformation. XRD spectroscopy of pressurized samples reveals that the transformation is not a direct transition from monoclinic to tetragonal phase but takes a detour via the cubic phase. At pressures above 20 GPa, the two high-temperature polymorphs are no longer accessible. In this case, the radiation provokes a transition into the second high-pressure phase which can be quenched to ambient presssure.
HfO_2 exhibits the same structural conformations (monoclinic, tetragonal, cubic, orthorhombic-I, and orthorhombic-II) as ZrO_2. A comparative study of ZrO_2 and HfO_2 shows that their close similarity is mirrored in their response to either irradiation or high pressure. However, for pressures up to 11 GPa, the response to the combination of both conditions differs from that observed in ZrO_2. Ion irradiation

at 10 GPa does not induce a phase transition into a different (high-temperature) phase, but results in an intensification of the predominating orthorhombic-I phase. Under decompression, this phase can be quenched down to ambient pressure and remains stable indefinitely. This is a very remarkable effect since the orthorhombic-I structure is usually not stable at ambient pressure and therefore can not be preserved. At higher pressures, when the sample is already close to or in the second high pressure phase, HfO_2 behaves similar to ZrO_2. The orthorhombic-II phase shows no response to radiation up to 3×10^{12} U-ions/cm^2. The highest-pressure structure seems to be extraordinarily radiation resistant making it interesting for further radiation hardness tests.

Obviously, the combination of high pressure and heavy ions play an important role in the phase transformation process, including pressure-enhanced radiation effects as well as pressure effects enhanced by radiation. This methodological approach provides a powerful tool for gaining access to unique, unstable high-pressure phases and recovering them to ambient conditions. This might lead to a future use of new materials that have so far been inaccessible.

7 Outlook

As shown in this work, combination of high pressure and ion irradiation offers a powerful method for inducing structural changes far from their actual stability field and stabilizing usually unstable structures to ambient conditions. Due to the novelty of this approach, there is of course a vast reservoir of materials with numerous structural configurations that need to be tested under similar conditions. Introducing high temperature as a third parameter during irradiation under high pressure opens access to even more structural configurations and allows the study of materials response to the simultaneous exposure of several extreme conditions. In this way, transformation processes may occur that are usually hindered at ambient conditions.
Often, high-pressure structures are associated with enhanced properties, which make their stabilization desirable. It is a well-known fact that under extremely high pressure most materials become conductive or even superconductive [200]. It is an ambitious goal to maybe one day stabilize a conductive structure of insulators to ambient conditions.
As for the investigated materials, I have shown that the orthorhombic-II structure shows very good radiation hardness making it a promising candidate as superhard material for industrial applications and replacing the artificially stabilized tetragonal form.

In this work, only the structural properties of the samples were analyzed via X-ray diffraction, Raman spectroscopy, and electron microscopy (REM and TEM). But during the period of this thesis, new analysis possibilities have been developed and introduced which could shed more light onto the changes induced by irradiation. The following pre-experiments with two analytical methods have proven to be quite useful and should be considered for future investigations.

7.1 SAXS experiments under high pressure

When looking at ion track structures, one can use either indirect measurements by deriving the damage cross section from the defect evolution, or imaging methods such as TEM or AFM. Indirect methods are not always possible or afflicted with large uncertainties and imaging methods often induce a damage of the material. Also, the access channel of the imaging probe (i.e. electron beam for TEM and tip for AFM) is incompatible with high-pressure apparatuses. To study the size of the the ion track which forms under pressure, or the kinetics of ion tracks under increasing pressure, an *in-situ* analysis method has to be applied. Small angle X-ray scattering (SAXS) offers a powerful tool to investigate the ion track size under pressure. Similar to wide angle scattering (WAXS) the photons interact with the electrons of the sample are thus scattered. Interference patterns of the scattered photons are recorded. The intensity $I(q)$ is measured as a function of the angle 2θ at a certain distance to the sample. If the scattering objects become large compared to the incident X-ray wavelength, interference patterns occur at smaller angles. Typical detection angles for SAXS are $\leq 5^\circ$, so structures in the size of several ten nm can be resolved. However a cylindrical ion track

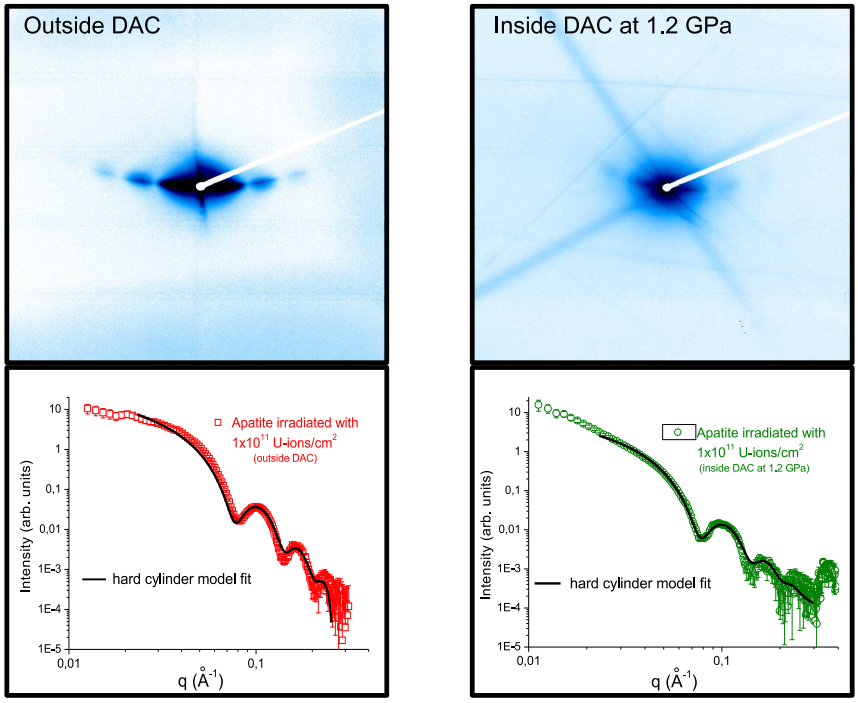

Figure 7.1: Upper row: Scattering image of ion tracks in apatite at ambient pressure, outside a DAC (left) and at a pressure of 1.2 GPa inside a DAC (right). Lower row: Scattering intensities as a function of scattering vector q. The black solid lines are fits of a hard cylinder model to the data.

and the crystalline matrix in which it exists consist of the same material. Therefore, SAXS is only observed when electron density inhomogeneities of a certain magnitude exist in the sample [201].

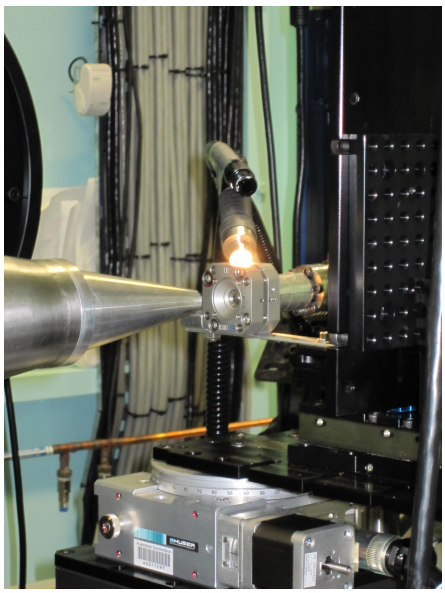

Figure 7.2: Experimental setup for SAXS measurements inside a DAC at the Australian Synchrotron in Melbourne.

The scattered intensity is proportional to the square of the electron density difference $(\rho_1 - \rho_2)$. If ρ_1 and ρ_2 are equal, the X-ray beam sees only a homogeneous electron density continuum and no track [202]. Pre-experiments have been performed on Durango apatite $[Ca_10(PO_4)_6(OH, F, Cl)_2$, because ion tracks with low electron density compared to the matrix are easily created. A thin ($\sim$ 50 μm) apatite crystal was irradiated with 1×10^{11} U-ions/cm^2 with a kinetic energy of 11.1 MeV/u. At this fluence, on can assume that around ten percent of the sample is covered with ion tracks. The SAXS measurements were performed at the Australian Syncrotron in Melbourne with a X-ray energy of 12 keV (1.033 Å) and a sample to detector distance of 1.6 m. The samples were mounted on a three-axis gomiometer for precise alignment. All samples were tilted by 10 ° during the measurements. The upper row of Fig. 7.1 shows the detector images of Apatite outside a DAC (left) and inside a DAC at 1.2 GPa (right). Although they are very weak under pressure, in both cases a streaky scattering pattern resulting from the ion tracks can be observed. The lower row of Fig. 7.1 shows the

scattering intensities as a function of the scattering vector q. The black lines are fits of a hard cylinder model (assuming cylindrical ion tracks with sharp boundaries and constant density inside the track) to the data. The scattering intensity is expressed by $I(q) \sim |f(q)|^2 \cdot e^{-\sigma_D^2 q}$ where σ_D is the phenomenological roughness parameter and $f(q)$ the form factor [203]. The form factor for the hard cylinder model is given by $f(q) = (2\pi LR\Delta\rho/q) \cdot J_1(Rq)$, where L is the track length, R the track radius, $\Delta\rho$ the electron density difference between track and matrix, and J_1 the first-order Bessel function [203]. For a pressure of 1.2 GPa no strong change in the track radius could be observed. In both cases the fits resulted in values of 5.1 nm. With increasing pressure the signal intensity weakens, and the track size becomes difficult to derive. These were just some preliminary test results, but in principle SAXS can be performed *in-situ* on pressurized samples and allows the study of ion track behavior as a function of pressure.

7.2 NMR analysis of radiation defects

In this study the investigated material responded to heavy ion irradiation via a structural phase change. But besides some other materials which amorphize under irradiation, most materials show a different behavior. In the case of ionic crystals, especially LiF, point defects and related clusters are formed. Mainly F-centers (also called color centers) consiting of an electron and an anion vacancy are created [204]. Structural analysis yields no information about this kind of defect. Because these defects are paramagnetic, nuclear magnetic resonance (NMR) is a very good analyzing method to provide information about the dynamics and concentration of the F-centers [205]. A new experimental setup at the Technical University of Darmstadt designed by A. Gädke and H. Stork allows depth resolved investigation of radiation defects within ion irradiated crystals without destroying the sample.

The great advantage of the setup designed by A. Gädke and H. Stork is the use of a magnet with static field gradient and the change from ordinary coils to specialized flat coils [206, 207, 208].

The maximum of the field gradient is at the center with 160 T/m [206] but the field profile radial to z has a very strong curvature which results in a inhomogeneous radial distribution of the magnetic field on a macroscopic sample. As measured by A. Gädke, the iso field lines are very flat at a distance of $\pm$ 10 cm from the z-center of the magnet. Here, the field gradient with 74 T/m at a magnetic field of 3.8 T is still large enough for our needs. The advantage of using a magnet with strong field gradient is that each position of the sample feels a different magnetic field therefore only, a small part fulfils the resonance condition when a radio-frequency pulse is introduced into the sample. One gathers only information of a thin slice Δz of the sample which can be calculated with [207].

$$\Delta z = \frac{1}{\gamma \; t_p \; G} \tag{7.1}$$

with G being the magnetic field gradient and t_p the pulse duration of the radio-frequency pulse. With a very accurate stepping motor, the sample is moved, so that each position of the sample is scanned. This allows a depth resolved analysis of radiation induced defects with an resolution of a few μm.

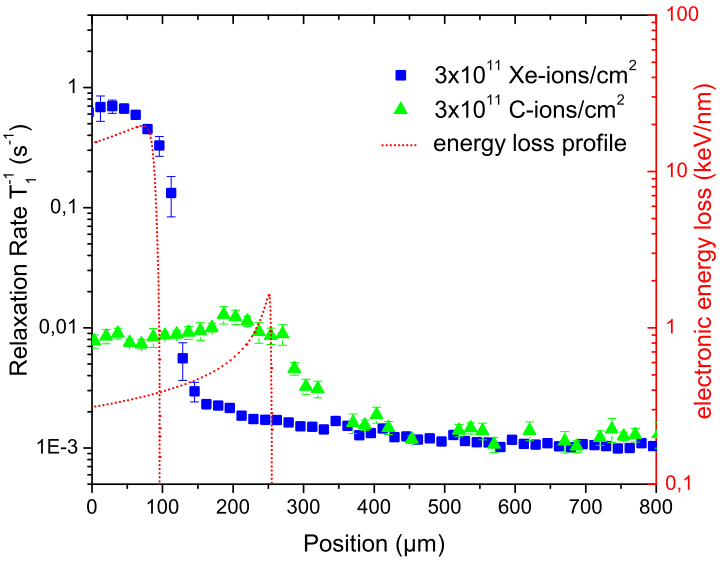

Figure 7.3: Relaxation rate versus sample depth for LiF irradiated with 3×10^{11} Xe- and C-ions/cm^2. The red curves are the calculated energy losses within the sample.

7.2.1 Unilac irradiated samples

In ionic crystals, the spin-lattice relaxation is dominated by the spin relaxation on paramagnetic defects. The electron spins of the radiation-induced, paramagnetic F-center interacts via dipole-dipole coupling with the nuclear spins which creates a faster relaxation of the system towards thermal equilibrium [209]. From this, one can easily conclude that higher concentration of F-centers leads to faster relaxation times (T_1) of the magnetization towards equilibrium and therefore higher relaxation rates (T_1^{-1}). When heavy ions are shot into LiF with typical UNILAC energy of 11.1 MeV/u, the penetration depth is limited to $\sim$ 100 μm. This means that for samples thicker than 100 μm only a small part of the crystal has been irradiated. For previous NMR analysis on irradiated samples, one could investigate a the whole sample, measuring a signal mixture of irradiated and unirradiated material. Now, signals from irradiated and unirradiated positions can be clearly distinguished. Figure 7.3 shows the relaxation rate profile at various positions for LiF irradiated with 3×10^{11} Xe- and C-ions/cm^2. The red curves are the calculated energy loss within the sample [22]. The ion range is about 96 μm for Xe ions and 255 μm for C ions. In the first hundred μm of the Xe-irradiated sample, the relaxation rate is elevated. Behind the penetration depth of the ions, the relaxation rate decreases strongly but is still enhanced compared to a pristine sample. The same effect can be observed in C-irradiated LiF. The calculated projected range is about 255 μm. Deeper within the crystal the magnetization rate decreases again to a similar level as for the Xe-irradiated crystal. Assuming that each F-center has the same effect on the relaxation rate, one can see that the F-center creation depends strongly on the electronic energy loss.

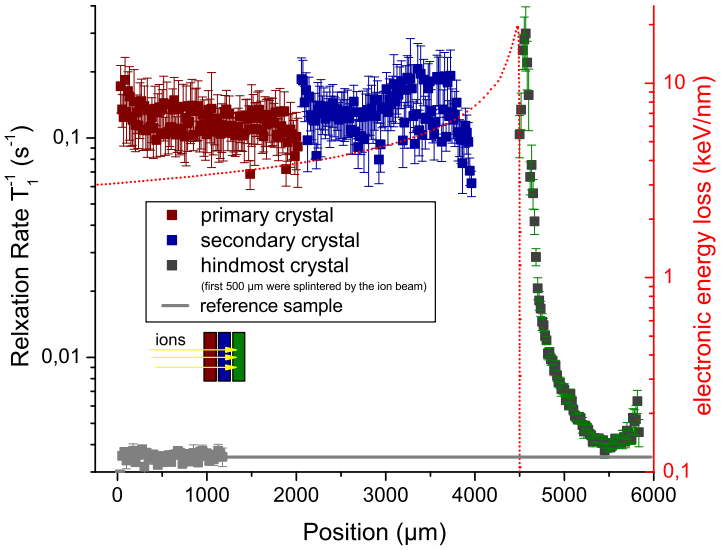

Figure 7.4: Relaxation rate versus the sample depth. This graph contains the signal of three individual LiF crystals which have been irradiated with 3×10^{11} Xe-ions/cm^2 and an energy of 170 MeV/u behind one another. The red line is the calculated electronic energy loss within the sample.

7.2.2 SIS Irradiated Samples

This method can also be applied to larger crystals. This way, the defect profile over a large range can be investigated. By using mechanically uncoupled crystals behind one another, the origin of defects beyond the projected ion range can be investigated. Fig. 7.4 shows the relaxation rate profile of three individual LiF crystals that have been irradiated behind each other at the SIS with 3×10^{11} Xe-ions/cm^2 and an energy of 170 MeV/u. The ion beam travelled completely though the first two crystals and stopped 500 μm below the surface of the last crystal. Because of the high energy input at the end of the ion range (Bragg maximum) the sample cracked due to large strain at the interface of irradiated and unirradiated crystal. In the first crystal, in which the energy loss is nearly constant, the relaxation rate also remains constant at a value which is almost two magnitudes higher than for unirradiated LiF (grey curve). At the end of the second crystal the energy loss starts to rise to peak eventually in the Bragg maximum, therefore a rise in the relaxation rate can be observed. In the hindmost crystal unfortunately the first 500 μm are missing due to the crack, but one can still observe a heightened relaxation rate which corresponds to the Bragg maximum. Beyond the penetration depth of the ions, the relaxation rate drops but is still elevated for more than 1000 μm. Possible causes of this long-ranging defects, beyond the ion range, might be recoil atoms, fragments, and X-ray emission during irradiation. Stork et al. [210] proposed that, especially for the low energy irradiations, mainly the emission of characteristic X-rays produced during the irradiation are the cause of the enhancement of the relaxation rate beyond the ion range.

Although momentarily limited to the detection of paramagnetic defects in samples at ambient conditions, this spatially resolved technique allows a new insight into the defect concentration and can be used to study large-scale defect diffusion e.g. under high temperature conditions. Although very difficult to

accomplish, a further development of the setup might in future allow studies under high-temperature and high-pressure conditions.

Bibliography

[1] C. Trautmann. *Ion beams in nanoscience and technology*, chapter Micro- and Nanoengineering with ion tracks, pages 369–387. Springer Verlag Berlin-Heidelberg, 2010.

[2] M. Rauber, I. Alber, S. Müller, R. Neumann, O. Picht, C. Roth, A. Schökel, M.E. Toimil-Molares, and W. Ensinger. Highly-ordered supportless three-dimensional nanowire networks with tunable complexity and interwire connectivity for device integration. *Nano Lett.*, 11:2304–2310, 2011.

[3] A. Benyagoub, F. Levesque, F. Couvreur, C. Gibert-Mougel, C. Dufour, and E. Paumier. Evidence of a phase transition induced in zirconia by high energy heavy ions. *Appl. Phys. Lett.*, 77:3197, 2000.

[4] P.F. McMillan. New materials from high-pressue experiments. *Nature Materials*, 1:19–25, 2002.

[5] P.F. McMillan. New materials from high pressure experiments: challenges and oppertunities. *High Press. Res.*, 1-2:7–22, 2003.

[6] Y. Al-Khatatbeh, K.K.M. Lee, and B. Kiefer. Phase relations and hardness trends of ZrO_2 phases at high pressure. *Phys. Rev. B.*, 81:214102, 2010.

[7] S. Tateno, K. Hirose, Y. Ohishi, and Y. Tatsumi. The structure of iron in Earth's inner core. *Science*, 330:359–361, 2010.

[8] M. Lang, F. Zhang, J. Zhang, J. Wang, B. Schuster, C. Trautmann, R. Neumann, U. Becker, and R.C. Ewing. Nanoscale manipulation of the propertries of solids at high pressure with relatistic ions. *Nature Materials*, 8:793, 2009.

[9] M. Lang, J. Lian, F. Zhang, B.W.H. Hendricks, C. Trautmann, R. Neumann, and R. Ewing. Fission tracks simulated by swift heavy ions at crustal pressures and temperatures. *Earth Plan. Sci. Lett.*, 274:355, 2008.

[10] W.L. Gong, W. Lutze, and R.C. Ewing. Zirconia ceramics for excess weapons plutoium waste. *J. Nucl. Mat.*, 277:239–249, 2000.

[11] M.A. Pouchon, M. Nakamura, CH. Hellwig, F. Ingold, and C. Degueldre. Cermet sphere-pac concept for inert matrix fuel. *J. Nucl. Mat.*, 319:37–43, 2003.

[12] C. Degueldre and CH. Hellwig. Study of a zirconia based inert matrix fuel under irradiation. *J. Nucl. Mat.*, 320:96–105, 2003.

[13] J.E. Lowther. Superhard materials. *Phys. Stat. Sol. B*, 217:533, 2000.

[14] J. Sarrao. Matter interactions in extremes. In *Decadal challenges for predicting and controlling materials performances in extremes*, pages 27–29, 2010.

[15] N. Itoh and K. Tnimura. Formation of interstital-vacancy pairs by electronic excitaions in pure ionic crystals. *J. Phys. Chem. Solids*, 51:717–735, 1990.

[16] R.L. Fleischer, P.B. Price, and R.M. Walker. *Nuclear Tracks in Solids*. University of California Press, 1975.

[17] Peter Sigmund. *Stopping of Heavy Ions: A Theoretical Approach*. Springer Verlag, 2004.

[18] J.D. Jackson. *Klassische Elektrodynamik*. Walter de Gruyter Verlag, Berlin, 1983.

[19] R. Spohr. *Ion Tracks and Microtechnology*. Vieweg Verlag, 1990.

[20] F. Bloch. Zur Bremsung rasch bewegter Teilchen beim Durchgang durch Materie. *Ann. Physik*, 16:285–320, 1933.

[21] Dimitry Varentsov. *Energy loss dynamics on intense heavy ion beams interacting with dense matter*. PhD thesis, Technische Universität Darmstadt, 2002.

[22] J.F. Ziegler and J.P. Biersack. *The stopping and the Range of Ions in Matter SRIM-2008*. http://www.srim.org, 2008.

[23] B. Gervais and S. Bouffard. Simulation of the primary stage of the interaction of swift heavy ions with condensed matter. *Nucl. Instr. Meth. B*, 88:355–364, 1994.

[24] R. L. Fleischer, P. B. Price, and R. M. Walker. Ion explosion spike mechanism for formation of charged-particle tracks in solids. *J. Appl. Physics*, 36:3645–3652, 1965.

[25] S. Klaumünzer, M.-D. Hou, and G. Schumacher. Coulomb explosions in a metallic glass due to the passage of fast heavy ions? *Phys. Rev. Lett*, 57:850–853, 1986.

[26] F. Dessauer. Über einige Wirkungen von Strahlen I. *Zeitschrift für Physik A: Hadrons and Nuclei*, 12:38–47, 1923.

[27] G.H. Vineyard. Thermal spikes and activated processes. *Rad. Effects*, 29:245–248, 1976.

[28] M. Toulemonde and C. Dufour. Transient thermal process after a high-energy heavy-ion irradiation of amorphous metals and semiconductors. *Phys. Rev. B*, 46:14362, 1992.

[29] M. Toulemonde, E. Paumier, and C. Dufour. Thermal spike model in the electronic stopping power regime. *Rad. Eff. Def. Solids*, 126:1–4, 1993.

[30] M. Toulemonde, Ch. Dufour, A. Meftah, and E. Paumier. Transient thermal processes in heavy ion irradiation of crystalline inorganic insulators. *Nucl. Instr. Meth. B*, 166-167:903, 2000.

[31] C. Trautmann. *Spuren energiereicher Ionen in Polymeren und metallischen Gläsern*. PhD thesis, Universität Frankfurt, 1994.

[32] M. Toulemonde, C. Trautmann, E. Balanzat, K. Hjort, and A. Weidinger. Track formation and fabrication of nanostructures with MeV-ion beams. *Nucl. Instr. Meth. B*, 216:1–8, 2004.

[33] E. Smith and G. Dent. *Modern Raman Spectroscopy: A Practical Approach*. John Wiley & Sons, Ltd, 2005.

[34] F.-M. Schnepel. *Physikalische Methoden in der Chemie*, chapter Raman-Spektroskopie. VCH Verlagsgesellschaft mbH, 1985.

[35] M.J. Pelletier. *Analytical Applications of Raman Spectroscopy*. Kaiser Optical Systems, Inc., 1999.

[36] Kazuo Nakamoto. *Infrared and Raman Spectra of Inorganic and Coordination Compounds*. John Wiley & Sons, Inc, 5 edition, 1997.

[37] Lehrstuhl für Physikalische Chemie, editor. *Grundlagen der Infrarot- und Ramanspektroskopie*. Universität zu Köln.

[38] H. Kuzmany. *Festkörperspektroskopie, Eine Einführung*. Springer Verlag, 1990.

[39] G. Will. *Powder Diffraction: The Rietveld Methode and the two-stage Methode*. Springer Verlag, 2006.

[40] L. Spieß, G. Teichert, R. Schwarzer, H.B., and C. Genzel. *Moderne Röntgenbeugung*. Vieweg+Teubner Verlag, 2009.

[41] Robert E. Dinnebier. Kristallstrukturbestimmung molekularer Substanzen aus Röntgenbeugungsaufnahmen an Pulvern. *Berichte aus Arbeitskreisen der DGK Nr. 7*, pages 1–108, 2000.

[42] Harold P. Klug and Leroy E. Alexander. *X-ray diffraction procedures*. John Wiley and Sons, 1974.

[43] `http://www.weltderphysik.de/_img/article_large/technologie_sase1_rdax_200x95_80.jpg`.

[44] O.H. Seeck and C. Deiter. The high resolution diffration beamline P08 at PETRA III. Technical report, Hasylab, DESY, Germany, 2009.

[45] David Attwood. *Soft X-rays and extreme ultraviolet radiation*. Cambridge University Press, 1999.

[46] P. Papon, J. Leblond, and P.H.E. Meijer. *The physics of phase transitions: Concepts and Applications*. Springer Verlag, 2002.

[47] J.A. Pople. Introduction to physics and chemistry at ultra-high pressue. In Society of chemical industry, editor, *The physics and chemistry of high pressures*, pages 119–121, 1962.

[48] M.T. Dove. Theory of displacive phase transitions in minerals. *Am. Mineralogist*, 82:213–244, 1997.

[49] F.P. Bundy. Pressure-temperature phase diagram of elemental carbon. *Physica A*, 156:169–178, 1989.

[50] R.S. Bradley. *High pressure physics and chemistry*, volume 1. Acadamic Press, London, 1963.

[51] Andrew Putnis. *Introduction to Mineral Sciences*. Cambridge University Press, 4 edition, 2001.

[52] M. Lang. *The Effect of Pressure on Ion Tack Formation in Minerals*. PhD thesis, University of Heidelberg, 2004.

[53] J. M. Besson, S. Klotz, G. Hamel, I. Makarenko, R. J. Nelmes, J. S. Loveday, R. Wilson, and W. G. Marshall. High pressure neutron diffraction. present and future possiilities using the paris-edinburgh cell. *High Press. Research*, 14:1–6, 1995.

[54] S. Klotz, J. M. Besson, G. Hamel, R. J. Nelmes, J. S. Loveday, and W. G. Marshall. High pressure neutron diffraction using the paris-edinburgh cell:experimental possibilities and future prospects. *High Press. Research*, 14:249–255, 1996.

[55] L. Merrill and W. A. Bassett. Miniature diamond anvil cell for single-crystal x-ray diffraction studies. *Rev. Sci. Instr.*, 45:290–294, 1974.

[56] W. A. Bassett. Diamond anvil cell, 50th birthday. *High Press. Research*, 29:163–186, 2009.

[57] R. Miletich, D. R. Allan, and W. F. Kuhs. High-pressure single crystal techniques. In *High-temperature and high-pressure crystal chemistry*, pages 445–519. 2000.

[58] S. Klotz, J.-C. Chervin, P. Munsch, and G. Le Marchand. Hydrostatic limits of 11 pressure transmitting media. *J. Phys. D: Appl. Phys*, 42:075413, 2009.

[59] C. Weikusat. *Modification of natural minerals by irradiation with relativistic heavy-ions with and without external pressure*. PhD thesis, Ruprecht-Karls Universität Heidelberg, 2010.

[60] Y. Akahama and H. Kawamura. Pressure calibration of diamond anvil Raman gauge to 310 GPa. *J. Appl. Phys.*, 100:043516, 2006.

[61] R.A. Forman, G.J. Piermarini, J.D. Barnett, and S. Block. Pressure measurement made by the utilization of ruby sharp-line lumimnescence. *Science*, 176:248, 1972.

[62] G. Piermarini and S. Block. The diamond anvil pressure cell. *http://nvl.nist.gov/pub/nistpubs/sp958-lide/100-103.pdf*, 2000.

[63] G.J. Piermarini, S. Block, J.D. Barnett, and R.A. Forman. Calibration of the pressure dependence of the R_1 ruby fluorescence line to 195 kbar. *J. Appl. Phys.*, 46:2774–2780, 1975.

[64] A. Jayaraman. Ultrahigh pressures. *Rev. Sci. Instr.*, 57:1013–1031, 1986.

[65] H.K. Mao, J. Xu, and P.M. Bell. Calibration of the ruby pressure gauge to 800 kbar under quasi-hydrostatic conditions. *J. Geophys. Res.*, 91:4673, 1968.

[66] H.K. Mao, P.M. Bell, J.W. Shaner, and D.J. Steinberg. Specific volume measurements of Cu, Mo, Pd, and Ag and calibration of the ruby R1 fluorescence pressure gauge from 0.06 to 1 Mbar. *J. Appl. Phys.*, 49:3276, 1978.

[67] A.D. Chijioke, W.J. Nellis, A. Soldatov, and I.F. Silvera. The ruby pressure standard to 150 GPa. *J. Appl. Phys.*, 98:114805, 2005.

[68] J.H. Eggert, K.A. Goettel, and I.F. Silvera. Ruby at high pressure. I. optical line shifts to 156 GPa. *Phys. Rev. B*, 40:5724–5732, 1989.

[69] Jon H. Eggert, Kenneth A. Goettel, and Isaac F. Silvera. Ruby at high pressure II. Fluorescence lifetime of the R line to 130 GPa. *Phys. Rev. B*, 40(8):5733–5738, Sep 1989.

[70] M. Popov. Pressure measurement from Raman spectra of stressed diomond anvils. *J. Appl. Phys.*, 95:5509, 2004.

[71] http://www inj.gsi.de/index.php.

[72] Peter Forck. Lecture notes on beam instrumentation an diagnostics. Technical report, GSI Helmholtzzentrum für Schwerionenforschung, 2009.

[73] M. Lang, U.A. Glasmacher, R. Neumann, D. Schardt, C. Trautmann, and G.A. Wagner. Energy loss of 50-GeV uranium ions in natural diamond. *Appl. Phys. A*, 80:691, 2005.

[74] Horiba Jobin Yvon™. HR 800 user manual.

[75] N.J. Everall. Modeling and measuring the effect of refeaction on the depth resolution of confocal raman spectroscopy. *Appl. Spectr.*, 54:6, 2000.

[76] A.P. Hammersley. Fit2d: An introduction and overview. *ESRF Internal Report*, page ESRF97HA02T, 1997.

[77] Luca Lutterotti. *MAUD-Material Analysis Using Diffraction Programm*. http://www.ing.unitn.it/ maud/, 2010.

[78] B.H. Toby. Expgui, a graphical user interface for GSAS. *J. Appl. Cryst.*, 34:210–213, 2001.

[79] K. Syassen. Ruby under pressure. *High Press. Res.*, 28(2):75, 2008.

[80] A.M. Ahmed. *Einkristallzüchtung und spektroskopische Untersuchungen von Fe-haltigen Korunden und Spinellen*. PhD thesis, Universität Bonn, 1976.

[81] J.D. Barnett, S. Block, and G.J. Piermarini. An optical fluorescence system for quantative presssure measurement in the diamond anvil cell. *Rev. Sci. Instr.*, 44:1, 1973.

[82] W.B. Holzapfel. Refinement of the ruby luminescence pressure scale. *J. Appl. Phys.*, 93:3, 2003.

[83] P.I. Dorogokupets and A.R. Oganov. *Phys. Rev. B*, 75:024115, 2007.

[84] G.C. Brown. Fluorescence lifetimes of ruby. *J. Appl. Phys.*, 35:3062, 1964.

[85] M. Millot, J.-M. Broto, J. Gonzalez, and F. Rodríguez. *Phys. Rev. B*, 81:075120, 2010.

[86] J.C Chervin, B. Canny, and M. Mancinelli. Ruby-spheres as pressure gauge for optically transparent high pressure cells. *High Press. Res.*, 21:305, 2001.

[87] X.A. Shen and Y.M. Gupta. Effect of crystal orientation on ruby R-line shifts under shock compression and tension. *Phys. Rev. B*, 48:5, 1993.

[88] M. Chai and J.M. Brown. Effects of static non-hydrostatic stress on the R-lines of ruby. *Geophys. Res. Lett.*, 23:24, 1996.

[89] Y.M. Gupta and X.A. Shen. Potential use of the ruby R_2-line shift for static high-pressure calibration. *Appl. Phys. Lett.*, 58:583, 1991.

[90] R. Rao, T. Sakuntala, S. N. Achary, and A.K. Tyagi. High pressure behaviour of $ZrGeO_4$: A Raman spectroscopic and photoluminescence study. *J. Appl. Phys.*, 106:123517, 2009.

[91] H. Dong, D. He, T.S. Duffy, and A. Zhao. Elastic moduli and strength of nanocrystalline cubic BC_2N from x-ray diffraction under nonhydrostatic compression. *Phys. Rev. B*, 79:014105, 2009.

[92] G.H. Watson and W.B. Daniels. Measuremets of raman intensities and pressure dependence of phonon frequencies in sapphire. *J. Appl. Phys.*, 52:956, 1981.

[93] S.P.S. Porto and R.S. Krishnan. Raman effect of corundum. *J. Chem. Phys.*, 47:1009, 1967.

[94] V. Mizeikis, S. Kimura, N.V. Surovtsev, V. Jarutis, A. Saito, H. Misawa, and S. Juodkazis. Formation of amorphous sapphire by a femtosecond laser pulse induced micro-explosion. *Appl. Surf. Sci.*, 255:9745–9749, 2009.

[95] S.H. Margueron and D.R. Clarke. Effect of polarization and uniaxial stress on the R-line luminescence of single crystal sapphire. *J. Appl. Phys.*, 101:094902, 2007.

[96] V.A. Skuratov, G. Bujnarowski, Yu.S. Kovalev, and K. Havanscak. Piezospectroscopic study of mechanical stress on Al_2O_3:Cr under swift heavy ion irradiation. *Vacuum*, 83:S65, 2009.

[97] V.A. Skuratov, G. Bujnarowski, Yu.S. Kovalev, J. O'Connell, and K. Havanscak. In situ postradiation analysis of mechanical stress in Al_2O_3:Cr induced by swift heavy-ion irradiation. *Nucl. Inst. Meth. B*, 2010.

[98] G. Bujnarowski, V.A. Skuratov, K. Havanscak, and Yu.S. Kovalev. Accumulation of mechanical stress in Al_2O_3:cr under swift heavy ion irradiation. *Rad. Eff. Def. Solids*, 7-8:409, 2009.

[99] B. Canut, A. Benyagoub, G. Marest, A. Meftah, N. Moncoffre, S.M.M. Ramos, F. Studer, P. Thevenard, and M. Toulemonde. Swift-uranium-ion-induced damage in sapphire. *Phys. Rev. B*, 51:18, 1995.

[100] A Kabir, A. Meftah, J.P. Stoquert, M. Toulemonde, and I. Monnet. Amorphization of sapphire induced by swift heavy ions: A two step preocess. *Nucl. Instr. Meth. B*, 266:2976, 2008.

[101] B. Canut R. Brenier and S.M.M. Ramos. Surface swelling of sapphire induced by MeV and GeV heavy-ion. *Nucl. Instr. Meth. B*, 90(1-4):339–343, 1994.

[102] B. Schuster, C. Weikusat, R. Miletich, C. Trautmann, R. Neumann, and F. Fujara. Influence of radiation damage on ruby as pressure gauge. *Phys. Rev. B*, 82:184110, 2010.

[103] J.F. Gibbons. Ion implantation in semiconductors-part II: Damage production and annealing. *Proc. IEEE*, 60:1062, 1972.

[104] W.J. Weber. Models and mechanisms of irradiation-induced amorphization in ceramics. *Nucl. Instr. Meth. B*, 166-167:98, 2000.

[105] U.A. Glasmacher, M. Lang, H. Keppler, F. Langenhorst, R. Neumann, D. Schardt, Ch. Trautmann, and G.A. Wagner. Phase transitions in solids stimulated by simultaneous exposure to high pressure and relativistic heavy ions. *Phys. Rev. Lett.*, 96:195701, 2006.

[106] B. Schuster, M. Lang, R. Klein, C. Trautmann, R. Neumann, and A. Benyagoub. Structural phase transition in ZrO_2 induced by swift heavy ion irradiation at high pressure. *Nucl. Instr. Meth. B*, 267:964, 2009.

[107] J.E. Jaffe, R.A. Bachorz, and M. Gutowski. Low-temperature polymorphs of ZrO_2 and HfO_2 A density-functional theory study. *Physical Review B*, 72:144107, 2005.

[108] Hendril Rijnten. Zirconia. Master's thesis, Technische Hogeschool Delft, 1971.

[109] J. Eichler, U. Eisele, and J. Rödel. Mechanical propoerties of monoclinic zirconia. *J. Am. Ceram. Soc.*, 87:1401–1403, 2004.

[110] Stephan Rudolph. Zirconia. *http://www.a-m.de/englisch/lexikon/zirkonoxid.htm*, 2004. Büro für angewandte Mineralogie, Tönisvorst.

[111] O. Ohtaka, E. Ito, and S. Kume. Synthesis and phase stability of cotunnite-type zirconia. *J. Am. Ceram. Soc.*, 71:448–449, 1988.

[112] H. Arashi, T. Yagi, S. Akimoto, and Y. Kuhdoh. New-high-pressure phase of ZrO_2 above 35 GPa. *Phys. Rev. B*, 41:7, 1990.

[113] J.E. Lowther and J.K. Dewhurst. Relative stability of ZrO_2 and HfO_2 structural phases. *Phys. Rev. B*, 60:21, 1999.

[114] J. Haines, J.M. Leger, and A. Atouf. Crystal structure and equation of state of cotunnite type zirconia. *J. Am. Ceram. Soc.*, 78:445–448, 1995.

[115] P. Bouvier and G. Lucazeau. Raman spectra and vibrational analysis of nanometric tetragonal zirconia under high pressure. *J. Phys. Chem. Solids*, 61:569–578, 2000.

[116] C.J. Howard, R.J. Hill, and B.E. Reichert. Structures of the ZrO_2 polymorphs at room temperature by high-resolution neutron powder diffraction. *Acta Cryst.*, B 44:116–120, 1988.

[117] O. Ohtaka, H. Fukui, T. Kunisada, and T. Fujisawa. Phase relations and equations of state of ZrO_2 under high temperature and high pressure. *Phys. Rev. B*, 63:174108, 2001.

[118] P. Bouvier, E. Djurado, and G. Lucazeau. High-pressure structural evolution of undoped tetragonal nanocrystalline zirconia. *Phys. Rev. B*, 62:13, 2000.

[119] O. Ohtaka and D. Andrault. Phase relations and equations of state of ZrO_2 to 100 GPa. *J. Appl. Cryst.*, 38:727–733, 2005.

[120] J.M. Leger, P.E. Tomaszewski, A. Atouf, and A.S. Pereira. Pressure-induced structural phase transition in zirconia under high pressure. *Phys. Rev. B*, 47:21, 1993.

[121] S. Desgreniers and K. Lagarec. High-density ZrO_2 and HfO_2 : Crystalline structures and equation of state. *Phys. Rev. B*, 59:13, 1999.

[122] J. Haines, J.M. Leger, S. Hull, J.P. Petitet, A.S Pereira, C.A Perottoni, and J.A.H da Jornada. Characterization of the cotunnite-type phases of zirconia and hafnia by neutron diffraction and Raman spectroscopy. *J. Am. Ceram. Soc.*, 80:1910–1914, 1997.

[123] R.E. Cohen, M.J. Mehl, and L.L. Boyer. Phase transition and elasticity in zirconia. *Physica B*, 150:1–9, 1988.

[124] J.K. Dewhurst and J.E. Lowther. Relative stability, structure, and elastic properties of several phases of pure zirconia. *Phys. Rev. B*, 57:2, 1998.

[125] H. Öztürk and M. Durandurdu. Formation of cotunnite phase in ZrO_2 under uniaxial stress : A first principle study. *J. Am. Ceram. Soc.*, 94:932–937, 2011.

[126] J.E. Lowther. Superhard ceramic oxids. *MRS Bulletin*, 28:189–193, 2003.

[127] X. Lio, W. Zhou, S.V. Ushakov, A. Navrotsky, and A.A. Demkov. Monoclinic to tetragonal transformations in hafnia and zirconia: A combined calorimetric and density functunal study. *Phys. Rev. B*, 80:134119, 2009.

[128] A. Mondal and S. Ram. Formation of a new polymorph of ZrO_2 with orthorombic crystal structure contained in a mesoporous structure. *Chem. Phys. Lett.*, 382, 2003.

[129] J. Seydel. *Nanokristallines Zirkoniumdioxid für Hochtemperatur-Brennstoffzellen*. PhD thesis, Technische Universität Darmstadt, 2003.

[130] Breviary Technical Ceramics. Zirconium oxide, 2009. Informationszentrum Technische Keramik.

[131] E. Wuchina, E. Opila, M. Opeka, W. Fahrenholtz, and I. Talmy. UHTCs: Ultra hard temperature ceramic materials for extreme environment applications. *Electrochem. Soc. Interfaces*, Winter:30–36, 2007.

[132] G. Pezzotti and A.A. Porporati. Raman spectroscopic analysis of phase-transformation and stress pattern in zirconia hip joints. *J. Biomdeical Optics*, 9:372–384, 2004.

[133] G. Willmann. Normung von Zikonoxidkeramiken für Hüftprotesen. *Biomed. Technik*, 42:342–346, 1997.

[134] W.L. Gong, W. Lutze, and R.C. Ewing. Reaction sintered glass: a durable matrix for spinel-forming nuclear waste composition. *J. Nucl. Mat.*, 278:73–84, 2000.

[135] V.M. Oversby, C.C. McPheeters, C. Degueldre, and J.M. Paratte. Control of civilian plutonium inventories using burning in a non-fertile fuel. *J. Nucl. Mat.*, 245:17–26, 1997.

[136] K.E. Sickafus, H. Matzke, K. Yasuda, J.A. Valdez, P. Chodak III, M. Nastasi, and R.A. Verrall. Radiation damage effects in zirconia. *J. Nucl. Mat.*, 274:66–77, 1999.

[137] D. Simeone, J.L. Bechade, D. Gosset, A. Chevarier, P. Daniel, H. Pilliaire, and G. Baldinozzi. Investigation on the zirconia phase transition under irradiation. *J. Nucl. Mat.*, 281:171–181, 2000.

[138] R.H.J. Hannink, P.M. Kelly, and B.C. Muddle. Transformation toughening in zirconia-containing ceramics. *J. Am. Ceram. Soc.*, 83:461–487, 2000.

[139] Robert Klein. Impedanzspektroskopische Untersuchungen an stickstoffdotierten Einkristallen. Master's thesis, Universität Giessen, 2006.

[140] M.E. Contreras, H. Orozco, and A. Medina-Flores. Structural analysis of yttria partially stabilized zirconia. *Rev. Mex. Fisica S*, 1:127–129, 2009.

[141] N. Khorshidi. *In-situ X-ray studies of model elcectrode surfaces for solid oxide fuel cells*. PhD thesis, Max-Planck-Institut für Metallforschung Stuttgart, 2010.

[142] K. Kawata, H. Maekawa, T. Nemoto, and T. Yamamura. Local structure analysis of YSZ by ^{89}Y MAS NMR. *Solid State Ionics*, 177:1687–1690, 2006.

[143] D.L. Porter, A.G. Evans, and A.H. Heuer. Transformation-toughening in partially stabilized zirconia (PSZ). *Acta Metallurgica*, 27:1649–1654, 1979.

[144] R.C. Garvie, R. H. Hannik, and R.T. Pascoe. Ceramic steel ? *Nature*, 258:703–704, 1975.

[145] J. A. Valdez, M. Tang, Z. Chi, M. I. Peters, and K. E. Sickafus. Characterization of an ion irradiation induced phase transformation in monoclinic zirconia. *Nucl. Instr. and Meth. B*, 218:103–110, 2004.

[146] J.A. Valdez, Z. Chi, and K.E. Sickafus. Light ion irradiation-induced phase transformationin the monoclinic polymorph of zirconia. *J. Nucl. Mater.*, 381:259–266, 2008.

[147] D. Simeone, D. Gosset, J.L. Bechade, and A. Chevarier. Analysis of the monoclinic-tetragonal phase transition of zirconia under irradiation. *J. Nucl. Mat.*, 300:27–38, 2002.

[148] A. Benyagoub. Mechanism of the monoclinic-to-tetragonal phase transition induced in zirconia and hafnia by swift heavy ions. *Phys. Rev. B*, 72:094114, 2005.

[149] A. Benyagoub. Kinetics of the crystalline to crystalline phase transformation induced in pure zirconia by swift heavy ion irradiation. *Nucl. Instr. Meth. B*, 206:132–138, 2003.

[150] G. Baldinozzi, D. Simeone, D. Gosset, I. Monnet, S. Le Caër, and L. Mazerolles. Evidence of extended defects produced in pure zirconia irradiated by swift heavy ions. *Phys. Rev. B*, 74:132107, 2006.

[151] D. Simeone, G. Baldinozzi, D. Gosset, S. Le Caër, L. Mazerolles, I. Monnet, and S. Bouffard. Effect of the energy deposition modes on the structural stability of pure zirconia. *Nucl. Instr. Meth. B*, 266:3023–3026, 2008.

[152] C. Gibert-Mougel, F. Couvreur, J.M. Costantini, S. Bouffard, et al. Phase transition of polycrysralline zirconia induced by swift heavy ion irradiation. *J. Nucl. Mat.*, 295:121–125, 2001.

[153] J.-M. Costantini, A. Kahn-Harari, F. Beuneu, and F. Couvreur. Thermal annealing study of swift heavy-ion irradiated zirconia. *J. Appl. Phys.*, 99:123501, 2006.

[154] A. Benyagoub. Phase transformations in oxides induced by swift heavy ions. *Nucl. Instr. Meth. B*, 245:225–230, 2006.

[155] B. Kim, J. Hahn, and K. R. Han. Quantitative phase analysis in tetragonal-rich tetragonal/monoclinic two phase zirconia by Raman spectroscopy. *J. Mat. Sci. Lett.*, 16:669–671, 1997.

[156] A. Benyagoub, F. Couvreur, S.Bouffart, et al. Phase transformation induced in pure zirconia by high energy heavy ion irradiation. *Nucl. Instr. Meth. B*, 175-177:417–421, 2001.

[157] F.X. Zhang, M. Lang, R.C. Ewing, J. Lian, and Z.W. Wang. High-pressure response of zirconia nanoparticles with an alumina shell. *J. Phys. Chem. C.*, 113:14658–14662, 2009.

[158] D. Vollath, F.D. Fischer, M. Hagelstein, and D.V. Szabó. Phase and phase transformation in nanocrystalline ZrO_2. *J. Nanopart. Res.*, 8:1003–1016, 2006.

[159] M.J. Mayo, A. Suresh, and W.D. Porter. Thermodynamics for nanosystems: Grain and particle-size dependent phase diagrams. *Rev. Adv. Mater. Sci.*, 5:1–109, 2003.

[160] A. Meldrum, L.A. Boatner, and R.C. Ewing. Size effects in the irradiation-induced crystalline-to-amorphous transformation. *Nucl. Instr. Meth. B*, 207:28–35, 2003.

[161] R.C. Garvie. Stabilization of the tetragonal structure in zirconia microcrystals. *J. Phys. Chem.*, 82:2, 1978.

[162] R.C. Garvie. The occurence of metestable tetragonal zirconia as a crystalline size effect. *J. Phys. Chem.*, 69:1238, 1965.

[163] R.W. Davidge and T.J. Green. The strength of two phase cermic/glass materials. *J. Mater. Sci.*, 3:629–634, 1968.

[164] M. Bremholm, J. Becker-Christensen, and B. Brummerstedt Iversen. High-pressure, high-temperature formation of phase-pure monoclinic zirconia nanocrystals studied by time-resolved in situ synchrotron x-ray diffraction. *Adv. Mater.*, 21:1–4, 2009.

[165] Z.W. Pan, Z.R. Dai, and Z.L Wang. Nanobelts of semiconducting oxides. *Science*, 291:1947–1949, 2011.

[166] A. Meldrum, L.A. Boatner, and R.C. Ewing. Nanocrystalline zirconia can be amorphized by ion irradiation. *Phys. Rev. Lett.*, 66:2, 2002.

[167] M.C. Wittels and F.A. Sherrill. Irradiation-induced phase transformation in zirconia. *J. Appl. Phys.*, 27:6, 1956.

[168] D.K. Smith and H.W. Newkirk. The crystal structure of baddeleyite (monoclinic ZrO_2) and its relation to the polymorphism of ZrO_2. *Acta Cryst.*, 18:983, 1965.

[169] J. Jagielski and L. Thomé. Damage accumulation in ion-irradiated cermics. *Vacuum*, 81:1352–1356, 2007.

[170] A.S. Foster, V.B. Sulimov, F. Lopez Gejo, A.L. Shluger, and R.M. Nieminen. Structure and electrical levels of point defects in monoclinic zirconia. *Phys. Rev. B*, 64:224108, 2001.

[171] R.A. Cowley. Structural phase transitions I: Landau theory. *Advances in Physics*, 28:1–110, 1980.

[172] P. Scherrer. Bestimmung der Grösse und der inneren Struktur von Kolloidteilchen mittels Röntgenstrahlen. *Nachr. Ges. Wiss. Göttingen*, 26:98–100, 1918.

[173] A.R. Stokes and A.J.C. Wilson. A methode of calculating the integral breadth of Debye-Scherrer lines: generalization to non-cubic crystals. *Math. Proc. Cambr. Phil. Soc.*, 40:197–198, 1944.

[174] L. Lutterotti and P. Scardi. Simultaneous structure and size-strain refinements by the Rietveld methode. *J. Apll. Cryst.*, 23:246–252, 1990.

[175] L. Yang and Z. Shen. An X-ray line-broadening study of tetragonal zirconia matrix. *J. Mater. Sci. Lett.*, 10:633–634, 1991.

[176] M. Toulemonde, W. Assmann, C. Dufour, A. Meftah, F. Studer, and C. Trautmann. Experimental phenomena and thermal spike model description of ion tracks in amorphisable inorganic insulators. *Mat. Fys. Medd.*, 52:263–292, 2006.

[177] M. Toulemonde, J.-M. Costantini, Ch. Dufour, A. Meftah, E. Paumier, and F. Studer. Track creation in SiO_2 and $BaF_{12}O_19$ by swift heavy ions: A thermal spike description. *Nucl. Instr. Meth. B*, 116:37, 1996.

[178] M. Caron, H. Rothard, M. Toulemonde, B. Gervais, and M. Beuve. Theoretical and experimental study of electronic temperatures in heavy ion tracks from auger electron spectra and thermal spike calculation. *Nucl. Instr. Meth. B*, 245:36–40, 2006.

[179] V.V. Katin and Y.N. Yavlinksii Y.V. Martinenko. Low-temperature ionization wave. *Sov. Techn. Phys. Lett.*, 13:276, 1987.

[180] G. Szenes. Ion-velocity-dependent track formation in yttrium ion garnet: A thermal spike analysis. *Phys. Rev. B*, 52, 1995.

[181] D. Ciuparu, A. Ensuque, G. Shafeev, and F. Bozon-Verduraz. Synthesis and apparent bandgap of nanophase ziconia. *J. Mater. Sci. Lett.*, 19:931–933, 2000.

[182] H. Jiang, R.I. Gomez-Abal, P. Rinke, and M. Scheffler. Electronic band strauctures of zirconia and hafnia polymorphs from the GW perspective. *Phys. Rev. B*, 81:085119, 2010.

[183] G. Szenes. Comparison of two thermal spike models for ion-solid interaction. *Nucl. Instr. Meth. B*, 269:174–179, 2011.

[184] V.G. Keramidas and W.B. White. Raman scattering study o the crystallization and phase transformations of ZrO_2. *J. Am. Ceram. Soc.*, 57:22–24, 1974.

[185] P.E. Quintard, P. Barbéris, A.P. Mirgorodsky, and T. Merle-Méjean. Comparative lattice-dynamical study of the Raman spectra of monoclinic and tetragonal phases of zirconia and hafnia. *J. Am. Ceram. Soc.*, 85:1745–1749, 2002.

[186] V. Milman, A. Perlov, K. Refson, S.J. Clark, J. Gavartin, and B. Winkler. Structural, electronic and vibrational properties of tetragonal zirconia under pressure: a density functional theory study. *J. Phys. Condens. Matter*, 21:485404, 2009.

[187] M. Lang, F. Zhang, J. Lian, C. Trautmann, R. Neumann, and R.C. Ewing. Irradiation-induced stabilization of zircon ($ZrSiO_4$) at high pressure. *Earth Planet. Sci. Lett.*, 269:291–295.

[188] B. Schuster, F. Fujara, B. Merk, R. Neumann, T. Seidl, and C. Trautmann. Response behaviour of ZrO_2 under swift heavy ion irradiation with and without external pressure. *submitted to Nucl. Instr. Meth. B*, 2011.

[189] G.J. Piermarini, S. Block, and J.D. Barnett. Hydrostatic limits in liquids and solids to 100 kbar. *J. Appl. Phys.*, 44:5377–5382, 1973.

[190] B. Schuster. Ionenstrahlinduzierte Strukturveränderung in Zirkoniumdioxid (ZrO_2) unter hohem Druck. Master's thesis, Technische Universität Darmstadt, 2007.

[191] J. Kang, E.-C. Lee, and K.J. Chang. First-principle study of the structural phase transformation of hafnia under pressure. *Phys. Rev. B*, 68:054106, 2003.

[192] Y. Al-Khatatbeh, K.K.M. Lee, and B. Kiefer. Phase diagram up to 105 GPa and mechanical strength of HfO_2. *Phys. Rev. B.*, 82:144106, 2010.

[193] R. Thomas, E. Rije, P. Ehrhart, A. Milanov, R. Bhakta, A. Bauneman, A. Devi, R. Fischer, and R. Waser. Thin films of HfO_2 for high-k gate oxide applications from engineered alkoxide- and amide-based mocvd precursors. *J. Electrochem. Soc.*, 154:77–84, 2007.

[194] A. Benyagoub. Swift heavy ion induced crystalline-to-crystalline phase transition in zirconia and hafnia:a comparative study. *Nucl. Instr. Meth. B*, 218:451–456, 2004.

[195] O. Ohtaka, H. Fukui, T. Kunisada, T. Fujisawa A. K. Funakoshi, W. Utsumi, T. Irifune, K. Kuroda, and T. Kikegawa. Phase relation and volume changes of hafnia under high pressure and high temperature. *J. Am. Ceram. Soc.*, 84:1369–1373, 2001.

[196] M. Gutowski, J.E. Jaffe, C.-L. Liu, M. Stoker, R.I. Hegde, R.S. Rai, and P.J. Tobin. Thermodynamic stability of high-k dielectric metal oxides ZrO_2 and HfO_2 in constact with Si and SiO_2. *Appl. Phys. Lett.*, 80:1897–1899, 2002.

[197] A. Jayaraman, S.Y. Wang, S.K. Sharma, and L.C. Ming. Pressure-induced phase transformations in HfO_2 to 50 GPa studies by raman spectroscopy. *Phys. Rev. B*, 48:9205–9211, 1993.

[198] H. Fujimori, M. Yashima, M. Kakihana, and M. Yoshimura. In situ ultraviolet Raman study on the phase transition in hafnia up to 2085 k. *J. Am. Ceram. Soc.*, 84:663–665, 2001.

[199] A. Benyagoub. Evidence of an ion-beam induced crystalline-to-crystalline phase transformation in hafnia. *Euro. Phys. B*, 34:395–398, 2003.

[200] K. Amaya, K. Shimizu, K. Takeda, N. Tateiwa, T. Muramatsu, M. Ishizuka, and T.C. Kobayashi. Superconductivity under high pressure. *Physica B*, 329-333:1308–1311, 2003.

[201] L.A. Feigin and D.I. Svergun. *Structure analysis by small-angle X-ray and neutron scattering*. Plenum Press, New York, 1987.

[202] O. Kratky. *Small Angle X-ray scattering*, chapter 1. Academic Press, London, 1982.

[203] B. Afra, M. Lang, M.D. Rodriguez, J. Znang, R. Giulian, N. Kirby, R.C. Ewing, C. Trautmann, M. Toulemonde, and P. Kluth. Annealing kinetics of latent particle tracks in durango apatite. *Phys. Rev. B*, 83:064116, 2011.

[204] K. Schwartz, G. Wirth, C. Trautmann, and T. Steckenreiter. Ion-induced formation of colloids in LiF at 15 K. *Phys. Rev. B*, 56:10711–10714, 1997.

[205] T. Klempt, S. Schweizer, K. Schwartz, O. Kanert, D. Suter, U. Rogulis, and J. M. Spaeth. Magnetic resonance investigation of the dynamics of F centers in LiF. *Solid State Communications*, 119:453–458, 2001.

[206] A. Gädke. *Diffusionseffekte in volumenselektiver NMR auf kleinen Längenskalen*. PhD thesis, Technische Universität Darmstadt, 2009.

[207] H. Stork. *Ortsaufgelöste NMR an schwerionenbestrahlten Kristallen*. PhD thesis, Technische Universität Darmstadt, 2009.

[208] H. Stork, A. Gädke, N. Nestle, and F. Fujara. Flat RF coils in static field gradient nuclear magnetic resonance. *J. Magn. Res.*, 200:321–327, 2009.

[209] T. Klempt, S. Schweizer, K. Schwartz, O. Kanert, D. Suter, U. Rogulis, and J. M. Spaeth. Magnetic resonance investigation of F centers in LiF caused by ionizing radiation. *Rad. Eff. Def. Solids*, 115:159–163, 2001.

[210] H. Stork, K.-P. Dinse, M. Ditter, F. Fujara, W. Masierak, R. Neumann, B. Schuster, K. Schwartz, and C. Trautmann. Spatially resolved nuclear spin relaxation, electron spin relaxation and light absorption in swift heavy ion irradiated lif crystals. *J. Phys.: Condens. Matter*, 22:185402, 2010.

Acknowledgements

A PhD thesis is not just this written work you hold in front of you, but a long-time project that engrosses one's life for several years. I want to use this opportunity to thank all people that supported me morally or scientifically during this period of time.
Sincere thanks to:

- Prof. Franz Fujara for the supervision of this doctoral work, his support, encouragement, and warm welcome into his group.
- Prof. Reinhard Neumann for the opportunity to perform my doctoral work at the Materials Research Department at GSI, and his supervision, support, and trust during all this time. Additionally for the possibility to attend several interesting conferences where I could present my work.
- Dr. Christina Trautmann for introducing me to the field of heavy-ion irradiation, her support, guidance and encouragement during all this time. I thank her especially for all the time she invested in reading and correcting my written work thus improving it a lot.
- Prof. Ronald Miletich-Pawliczek for successful collaborations, and the provision of the oriented ruby crystals.
- Prof. Dieter H.H. Hoffmann for his strong interest in my work and the opportunity to present it to the high density matter community.
- Dr. Maik Lang for introducing me into the handling of the diamond anvil cells, successful collaborations and fruitful discussions via long-distance phone calls.
- Dr. Robert Klein for all his support during cell filling sessions, beamtimes, and for good discussions.
- Dr. Christian Weikusat for his help with mineralogical questions and support during Cave A beamtimes.
- Dr. Dieter Schardt for the support during Cave A beamtimes.
- Dr. Oliver Seeck for his great support during the XRD beamtime at DESY.
- Dr. Leonid Dubrovinsky for providing some of the DACs and his warm welcome to the Bavarian Geological Institute in Bayreuth.
- Dr. Marcel Toulemonde for his suggestions and help with the thermal spike model.
- Dr. Patrick Kluth, Dr. Matias Rodriguez, and Boshra Afra for their warm welcome to the Australian National University and the SAXS analysis.
- Dr. Fuxiang Zhang for the good high-resolution TEM images.

- Elko Schubert for all his technical support, help during the experiment setups, and constructions on short notice.
- Dipl.-Phys. Bruno Merk and Dipl.-Chem. Tim Seidl for all their help during DESY beamtimes and just for being great colleagues.
- Dr. Kay-Obbe Voss for offering to read and correct this work, all his help and diverse support.
- MSc Michael Ditter for his help with the NMR spectrometer.
- all members of the GSI Materials Research Department (Dipl.-Phys. Ina Alber, Dipl.-Phys. Veronika Bayer, Dr. Markus Bender, Dipl.-Chem. Markus Krause, Dipl.-Chem. Vincent Lima, Dipl.-Phys. Sven Müller, MSc. Quoc Hung Nguyen, Dr. Oliver Picht, Dipl.-Chem. Markus Rauber, MSc. Anton Romanenko, Dr. Daniel Severin, and those I might have forgotten) for the great atmosphere, funny coffee rounds, long beam time nights, interesting discussions, all their help ... and much more.
- my friend Dieter Schuster for absolutely everything. I couldn't have done it without you.
- my family, especially my mother who supported and encouraged me my whole life.

Thank you !

Lebenslauf: Beatrice Schuster

Geburtsdatum	1. Februar 1983
Geburtsort	Darmstadt
E-Mail	bea.schuster@gsi.de

Ausbildung

Januar 2000 - September 2000	**Auslandsaufenthalt** in Annapolis Royal, Kanada. Erwerb des High-School Abschlusses mit Auszeichnung am Annapolis West Education Center (AWEC)
Juni 2002	**Abitur** an der Eleonorenschule in Darmstadt
Oktober 2002	Beginn des Physikstudiums an der TU Darmstadt
Oktober 2005 - März 2006	**Miniforschung** am Deutschen Kunststoffinstitut (DKI)
September 2006 - Oktober 2007	**Diplomarbeit** in der AG von Prof. F. Fujara, durchgeführt im Bereich Materialforschung am GSI Helmholtzzentrum für Schwerionenforschung
November 2007	Abschluss des Physikstudiums mit **Diplom** an der TU Darmstadt (**Vordiplom** März 2005)
Januar 2008 - heute	**Doktorarbeit** in der AG von Prof. F. Fujara, durchgeführt im Bereich Materialforschung am GSI Helmholtzzentrum für Schwerionenforschung
Januar 2008 - heute	Mitglied der Graduiertenschule „Helmholtz Graduate School for Hadron and Ion Research“ (HGS-HIRe)

Berufserfahrung

Dezember 2009 - heute	Wissenschaftlicher Mitarbeiter an der Technischen Universität Darmstadt
Januar 2008 - Dezember 2009	Stipendiat des „Frankfurter Instituts für Advanced Sciences“ (FIAS)
August 2005 bis Januar 2008	Redaktionsassistent beim wissenschaftlichen Journal **Laser and Particle Beams (LPB)**.
Oktober 2000 - Juli 2005	Lehrer an der **Erzhäuser Musikschule**.

Veröffentlichungen

- **B. Schuster**, F. Fujara, B. Merk, R. Neumann, T. Seidl, and C. Trautmann „Response behavior of ZrO_2 under swift heavy ion irradiation with and without external pressure“ submitted to Nucl. Instr. Meth. B (June 2011)
- M. Ditter, H. Stork, **B. Schuster**, F. Fujara „Combining one-dimensional stray-field micro-imaging with mechanical field-cycling NMR: A new spectrometer design“ J. Magn. Res., 209, (2011), 47
- **B. Schuster**, C. Weikusat, R. Miletich, C. Trautmann, and R. Neumann„Influence of radiation damage on ruby as pressure gauge“ Phys. Rev. B, 82, 18, (2010) 184110
- C. Weikusat, U.A. Glasmacher, **B. Schuster**, C. Trautmann, R. Miletich, and R. Neumann „Raman study of apatite amorphised with swift heavy ions under various irradiation conditions“ Phys. Chem. Minerals, 38, (2010) 293
- M. Lang, F.X. Zhang, J.M. Zhang, J.W. Wang, J. Lian, W.J. Weber, **B. Schuster**, C. Trautmann, R. Neumann, and R.C. Ewing „Review of $A_2B_2O_7$ pyrochlor response to irradiation and pressure“ Nucl. Instr. Meth. B, 268, (2010) 2951
- H. Stork, K.-P. Dinse, M. Ditter, F. Fujara, W. Masierak, R. Neumann, **B. Schuster**, K. Schwartz, and C. Trautmann „Spatially resolved nuclear spin relaxation, electron spin relaxation and light absorption in swift heavy ion irradiated LiF crystals “ J. Phys. Cond. Matter, 22, (2010) 185402
- M. Lang, F. Zhang, J. Zhang, J. Wang, **B. Schuster**, C. Trautmann, R. Neumann, U. Becker, and R.C. Ewing „Nanoscale manipulation of the propertries of solids at high pressure with relatistic ions“ Nature Materials 8, (2009) 793
- **B. Schuster**, M. Lang, R. Klein, C. Trautmann, R. Neumann, and A. Benyagoub „Structural phase transition in ZrO_2 induced by swift heavy ion irradiation at high pressure“ Nucl. Instr. Meth. B, 267, (2009) 964
- H. Stork, K.-P. Dinse, F. Fujara, A. Hamburger, P. Jakes, R. Neumann, **B. Schuster**, K. Schwartz, and C. Trautmann „Spatially resolved characterization of Xe ion irradiated LiF crystals using static field gradient NMR“ J. Phys. Cond. Matter, 20, (2008) 465215

Jahresberichte

- **B. Schuster**, O. Seeck, C. Trautmann, and F. Fujara „Stbilization of high-pressure phase in HfO_2“ DESY Annual Report (2010)
- **B. Schuster**, C. Trautmann, and F. Fujara „Stabilization of high-pressure phase in HfO_2“ GSI Scientific Report, PNI-MR-02 (2010)
- **B. Schuster**, R. Miletich, R. Neumann, C. Trautmann, and C. Weikusat „Influence of heavy-ion irradiation on the use of ruby as pressure calibrant“ GSI Scientific Report, Materials-13 (2009)

- **B. Schuster**, C. Trautmann, and R. Neumann „New phase of ZrO_2 created by swift heavy ion irradiation at high pressure“ GSI Scientific Report, Materials-14 (2008)
- **B. Schuster**, A. Benyagoub, F. Fujara, R. Klein, M. Lang, R. Neumann, and C. Trautmann, and R. Neumann „Structural phase transition in ZrO_2 induced by swift heavy ion irradiation at high pressure“ GSI Scientific Report, Materials-02 (2007)

Auszeichnungen

- E-MRS Graduate Student Award for an outstanding paper contribution at the E-MRS conference, Nice, France, 2011
- Young Researcher Award for the best oral presentation at the 15^{th} REI Conference in Padova, Italy, 2009